Faculty of
Natural Science
Institute of
Electrochemistry

Insights into the Electrochemistry of *N*-Methyl-*N*-propylpiperidinium Bis(trifluoromethane)sulfonimide on Au(111) and the Alkali Metal Deposition

Dissertation to obtain the academic degree Dr. rer. nat.

Submitted by:
Maren-Kathrin Heubach
born in Stuttgart

2024

Version of November 6, 2024

Dean of the Faculty of Natural Sciences at Ulm University:
Prof. Dr. Kay-Eberhard Gottschalk

First Reviewer:
Prof. Dr. Timo Jacob

Second Reviewer:
PD Dr. Joachim Bansmann

Defence Date:
25.09.2024

© 2024 Maren-Kathrin Heubach

Satz: PDF-LaTeX 2$_\varepsilon$

For no one and everyone.

I only do this because I'm having fun.
The day I stop having fun, I'll just walk away.

— Heath Ledger

Parts of this thesis were already published in following articles:

M.-K. Heubach, F. M. Schuett, L. A. Kibler, A. Abdelrahman, T. Jacob, *ChemElectroChem* **2022**, *9*, e202200722.
https://doi.org/10.1002/celc.202200722,
CC BY-NC-ND 4.0, https://creativecommons.org/licenses/by-nc-nd/4.0/

M.-K. Heubach, F. M. Schuett, L. A. Kibler, A. Abdelrahman, T. Jacob, *ChemElectroChem* **2022**, *9*, e202200935. (Front Cover)
https://doi.org/10.1002/celc.202200935

M.-K. Heubach, F. M. Schuett, J. Mayer, O. W. Elkhafif, A. K. Engstfeld, T. Jacob, **2024**, DOI 10.26434/CHEMRXIV-2024-05D56.
https://doi.org/10.26434/chemrxiv-2024-05d56,
CC BY 4.0, https://creativecommons.org/licenses/by/4.0/

M.-K. Heubach, J. Bansmann, A. K. Engstfeld, T. Jacob, **2024**, DOI 10.26434/CHEMRXIV-2024-ZKKNM.
https://doi.org/10.26434/chemrxiv-2024-zkknm,
CC BY 4.0, https://creativecommons.org/licenses/by/4.0/

Furthermore, following articles were published during this dissertation which are not mentioned in this thesis:

F. M. Schuett, S. J. Zeller, M. J. Eckl, F. M. Matzik, M.-K. Heubach, T. Geng, J. M. Hermann, M. Uhl, L. A. Kibler, A. K. Engstfeld, T. Jacob, *Angewandte Chemie International Edition* **2021**, *60*, 22783–22790.

F. M. Schuett, M.-K. Heubach, J. Mayer, M. U. Ceblin, L. A. Kibler, T. Jacob, *Angewandte Chemie - International Edition* **2021**, *60*, 20461–20468.

S. Fackler, M. Wittmann, M. Heubach, J. Hermann, L. Kibler, T. Jacob, *Electrochimica Acta* **2024**, *490*, 144225.

Conference Contributions

Talks

Corresponding author

Initial Stages of Alkali Metal Deposition on Au(111) from [MPPip][TFSI]
M.-K. Heubach, F. M. Schuett, A. Abdelrahman, L.A. Kibler, T. Moser, J. Kunze-Liebhäuser, T. Jacob, in *DPG Frühjahrstagung SKM*, Berlin, **2024**.

In Situ Scanning Tunnelling Microscopy of Nanostructures in "new electrolytes" – Challenges and Opportunities
M.-K. Heubach, T. Jacob, in *KFN Symp. Nano-BW*, Bad Herrenalb, **2023**.

Alkali Metal Deposition on Au(111) from an Ionic Liquid: Comparing Initial Stages and Bulk Deposition of Lithium and Sodium
M.-K. Heubach, F. M. Schuett, L.A. Kibler, A. Abdelrahman, T. Moser, J. Kunze-Liebhäuser, T. Jacob, in *74th Annu. Meet. Int. Soc. Electrochem.* Lyon, **2023**.

Comparing the Initial Stages and Cluster Growth of Sodium and Lithium by in situ STM
M.-K. Heubach, F. M. Schuett, L. A. Kibler, A. Abdelrahman, T. Moser, J. Kunze-Liebhäuser, T. Jacob, in *Bunsen-Tagung 2023*, Berlin, **2023**.

Initial Stages of Cathodic Corrosion of Au(111) in an Ionic Liquid
M.-K. Heubach, F. M. Schuett, A. Abdelrahman, Y. Mattausch, L. A. Kibler, T. Jacob, in *DPG Frühjahrstagung SKM*, Dresden, **2023**.

Initial Stages of Cathodic Corrosion Investigated by in situ Scanning Tunnelling Microscopy
M.-K. Heubach, F. M. Schuett, A. Abdelrahman, L. A. Kibler, T. Jacob, in *KFN Symp. Nano-BW*, Bad Herrenalb, **2022**.

Current Understanding of Electrochemical Properties of Ionic Liquids on Well-Defined Electrodes: A Reliable Benchmark?
M.-K. Heubach, F. M. Schuett, J. Mayer, O. El-Khafif, A. Abdelrahman, A. K. Engstfeld, T. Jacob, in *ECOSS 35*, Esch-Sur-Alzette, **2022**.

In-situ STM Study of Sodium Deposition onto Au(111) in [MPPip][TFSI]: Initial Stages, Nucleation, Cluster Growth, and Alloy Formation
M.-K. Heubach, A. Abdelrahman, F. M. Schuett, M. J. Eckl, M. U. Ceblin, S. J. Zeller, L. A. Kibler, T. Jacob, in *241st ECS Meet.* Vancouver, **2022**.

Au(111) in [MPPip][TFSI] in Dependence of Water Content: Revealing the Initial Stages of Cathodic Corrosion using in-situ STM

M.-K. Heubach, F. M. Schuett, A. Abdelrahman, L. A. Kibler, T. Jacob, in *241st ECS Meet.* Vancouver, **2022**.

Sodium Deposition from [MPPip][TFSI] on Au(111) - From Initial Nucleation to Cluster Growth
M.-K. Heubach, A. Abdelrahman, F. M. Schuett, M. U. Ceblin, M. J. Eckl, S. J. Zeller, L. A. Kibler, T. Jacob, in *72nd Annu. Meet. Int. Soc. Electrochem*. Jeju Island, **2021**. (online)

Other

Atomistic Insights at Au(111) / Deep Eutectic Solvents Interface using in situ STM
Y. Mattausch, A. Abdelrahman, M.-Kathrin Heubach, L. A. Kibler, T. Jacob, *DPG-Frühjahrstagung SKM*, Dresden, **2023**.

Differences in the Electrochemical Deposition of Zinc from the Ionic Liquid [MPPI][TFSI] on Au(111) and Au(100) Model Electrodes
F. M. Schuett J. Mayer, M.-K. Heubach, M. U. Ceblin, L. A. Kibler, T. Jacob in *71st Annu. Meet. Int. Soc. Electrochem* Belgrade, **2020**. (online)

Posters

Corresponding Author

Water Influence on Cathodic Corrosion of Au(111) in Ionic Liquids: an in situ STM study
M.-K. Heubach, F. M. Schuett, A. Abdelrahman, L. A. Kibler, T. Jacob in *Bunsen-Tagung 2024*, Aachen, **2024**.

Electrochemical Behavior of Ionic Liquids on Au(111): Effects of Water Content and Purification Procedures
M.-K. Heubach, F. M. Schuett, J. Mayer, O. El-Khafif, A. K. Engstfeld, T. Jacob in *74th Annu. Meet. Int. Soc.* Electrochem. Lyon, **2023**.

Tracking Sodium Deposition on Au(111) by in situ STM: From Initial Stages to Alloy Formation
M.-K. Heubach, A. Abdelrahman, F. M. Schuett, L. A. Kibler, T. Jacob, in *2nd ELSICS Conf. Int. Bunsen Discuss. Meet.* Göttingen, **2022**.

Initial Stages of Cathodic Corrosion of Au(111) in [MPPip][TFSI] in Dependence of Water Content
M.-K. Heubach, F. M. Schuett, A. Abdelrahman, L. A. Kibler, T. Jacob, in *72nd Annu. Meet. Int. Soc. Electrochem.* online, **2021**. (online)

In situ Scanning Tunnelling Microscopy in Battery Research
M.-K. Heubach, A. Abdelrahman, F. M. Schuett, M. U. Ceblin, M. J. Eckl, S. J. Zeller, L. A. Kibler, T. Jacob, in *Post-Lithium Research: Women in Focus*, online, **2021**. (online)

Resolving the Initial Stages of Sodium Deposition from an Ionic Liquid on Au(111): An in situ STM Study
M.-K. Heubach, A. Abdelrahman, F. M. Schuett, M. U. Ceblin, M. J. Eckl, S. J. Zeller, L. A. Kibler, T. Jacob, in *International Sodium Battery Symposium*, online, **2021**. (online)

Sodium Deposition from [MPPI][TFSI] on Au(111): Initial Stages of the Deposition using in-situ STM
M.-K. Heubach, F. M. Schuett, A. Abdelrahman, T. Jacob, in *708. WE-Heraeus-Seminar*, Bad Honnef, **2019**.

Other

Studying the Local Electrochemistry at Solid-Liquid Interfaces Using Modified Miniature Fluid-FM Cantilevers
M. Karimnia, M.-K. Heubach, T. Jacob, in *74th Annu. Meet. Int. Soc.* Electrochem. Lyon, **2023**.

Differences in the Electrochemical Deposition of Zinc from the Ionic Liquid [MPPI][TFSI] on Au(111) and Au(100) Model Electrodes
F. M. Schuett J. Mayer, M.-K. Heubachl, M. U. Ceblin, L. A. Kibler, T. Jacob, in *70nd Annu. Meet. Int. Soc. Electrochem.* Durban, **2019**.
and
F. M. Schuett, M.-K. Heubach, J. Mayer, T. Jacob, in *Electrochemistry 2018*, Ulm, **2018**.

Contents

Contents **xi**

1 Introduction **1**

2 Theoretical Background **5**

2.1 Au(111) 5

2.1.1 Steps and other Surface Defects 6

2.1.2 Reconstruction 7

2.2 Ionic Liquids 9

2.2.1 Ionic Liquid-Electrode Interfaces 11

2.3 Cathodic Corrosion of Au 11

2.4 Metal Electrodeposition 12

2.4.1 Metal Deposition on the Reconstructed Au(111) surface 14

2.4.2 Metal Deposition from Ionic Liquids 14

2.5 Cyclic Voltammetry 15

2.6 *In situ* Scanning Tunnelling Microscopy 16

3 State of the Art **21**

3.1 Impurities in ILs 21

3.2 [MPPyr][TFSI] on Au(111) 22

3.3 Alkali Metal Deposition from ILs 24

4 Experimental **27**

4.1 Preparation and Cleaning of the Electrodes 27

4.1.1 Au(111) Working Electrode 27

4.1.2 Pt Counter Electrode 28

4.1.3 Reference Electrodes 28

$Zn/Zn[TFSI]_2$ 28

Na 29

$Al/AlPO_4$ 29

4.2 Electrolyte Preparation 29

4.2.1 Preparation of the Pure IL 29

4.2.2 Preparation of the Electrolytes for Na and Li Deposition 30
4.3 Cleaning of the Equipment 30
4.4 Karl Fischer Titration 30
4.5 XPS Measurements 30
4.6 Electrochemical Measurements 31
4.7 Scanning Tunnelling Microscopy 32
4.7.1 Tip Preparation 32
Tip Etching 32
Tip Coating 34
4.7.2 STM Set-Up 34
4.7.3 Measurements 35
4.8 Used Chemicals and Gases 35

5 Electrochemical Behaviour of Au(111) in [MPPip][TFSI] 39
5.1 Classification of [MPPip][TFSI] in Two Types of Electrochemical Behaviour . . . 39
5.2 Influence of H_2O and O_2 46
5.2.1 Drying Methods 46
5.2.2 Influence of Adding H_2O and O_2 52

6 Morphological Stability of Au(111) in [MPPip][TFSI] 57
6.1 Oxidation and Reduction of Au(111) 57
6.2 Initial Stages of Cathodic Corrosion 60
6.3 Influence of H_2O on the Cathodic Corrosion 63
6.4 Formation and Lifting of the Reconstruction 71
6.5 Role of O_2 on Structural Changes 72
6.6 Overview on Surface Structures of Au(111) in [MPPip][TFSI] 77

7 Alkali Metal deposition on Au(111) from [MPPip][TFSI] 79
7.1 Sodium Deposition on Au(111) from [MPPip][TFSI] 79
7.1.1 Electrochemical Overview 79
7.1.2 Initial Stages of Sodium Deposition on Au(111) 83
7.1.3 UPD of Na on Au(111) 85
7.1.4 Bulk Alloy Formation of Na and Au 91

7.2 Li Deposition on Au(111) from [MPPip][TFSI] 95
7.2.1 Electrochemical Overview 95
7.2.2 Underpotential Deposition of Li on Au(111) 99
7.2.3 Comparison of Na and Li Deposition 101

8 Summary and Outlook **103**

A Appendix **107**

Bibliography **113**

List of Figures **127**

List of Tables **131**

Curriculum Vitae **133**

Danksagung **135**

1 Introduction

Due to the increasing global demand for energy, electrochemical energy storage systems are becoming increasingly important.[1,2] Li-ion batteries (LIBs) are primarily used for portable devices, such as mobile phones and laptops, but also for electric vehicles and stationary energy storage systems.[3–5] However, the resources for the nowadays used LIBs are scarce and not equally distributed over the planet.[1,3,4] Therefore, a lot of research is performed on post-lithium batteries which use other technologies.[6–10]

Lately, the interest in Na ion or Na metal batteries increased since Na is less expensive than Li and its abundance is not limited to a few countries.[11–13] Its standard electrode potential is more positive than Li's standard electrode potential but still very negative.[14,15] As for all alkali metals, Na is extremely reactive if it comes in contact with water and other molecules with acidic hydrogen atoms.[16] Additionally, it reacts with solvents, usually used in standard electrolytes for Li-ion batteries, such as organic carbonates.[17] Other drawbacks in developing Na metal batteries are caused by dendrite formation.[18–20]

Ionic liquids (ILs) are versatile electrolytes used in many electrochemical applications, especially in energy conversion and storage.[21–25] They can be used in supercapacitors, batteries, or organic solar cells.[21,26–29] These studies include the deposition of alkali metals from ILs for the development of battery electrolytes, *e.g.*, for Li and Na metal batteries.[8,15,30–36] Beneficial properties which make ILs interesting electrolytes for Na batteries are their high conductivities, broad electrochemical stability windows, and thermal and chemical stability.[9,10,37] Several studies have shown that Na plating and stripping is possible in IL-based electrolytes.[8,15,30,36]

However, the electrochemistry of pure ILs is not yet completely understood. Many studies have investigated the IL-electrode interface with different ILs and electrodes.[38–44] Additionally, the influence of impurities, such as water, metal cations or halogenides was studied.[29,37,45–54] For investigating the fundamental electrochemical properties of an electrolyte, it is advantageous to perform the measurements under an inert atmosphere and use simple and mostly

inert electrodes which can be prepared in a reproducible way.[55] Often, Au(111) single crystals are used since they were suggested to fulfil these requirements.[56–59] However, even if such well-defined conditions are used, astonishingly different results with the same IL can be achieved.[32,44,60–62] Such differences can, for example, be observed in cyclic voltammograms (CVs) and their interpreations.[60] Different setups or experimental procedures could explain variations in the experimental results. However, it is known that even the same IL from the same supplier purchased at different times with different lot numbers shows differences in the electrochemical behaviour, which suggests that the ILs differ in the impurities.[37]

Cyclic voltammetry is often used to gain a first impression of the electrochemical properties systems.[63–66] This technique is beneficial for comparing electrolytes, electrodes or additives by analysing the different current responses to the applied potential cycles.[45,49,67–69] Nevertheless, a fundamental understanding of the systems is required to interpret this response correctly.[55,66] Furthermore, the measured current is always an average signal over the whole system, *e.g.*, for polycrystalline material, the signal is a superposition of all present facets.[63]

Additional tools are required to attribute the potential dependent features in the CV to processes taking place at the electrode surface. Structural properties of the surface can be studied by *in situ* scanning probe microscopy (SPM). SPM techniques are a valuable tool to get a direct relationship between a current response measured in a CV and morphologic changes on the electrode's surface.[59,70,71] Unlike cyclic voltammetry, SPM gives microscopic insights into the structural processes happening on the surface, including adsorbate structures and the surface mobility.[58,59,70–72] By choosing different regions on the surface, it is possible to determine which sites are active for the electrochemical processes. Generally, scanning tunnelling microscopy (STM) and atomic force microscopy (AFM) can both be used for *in situ* measurements.[52,59,71,73] In this thesis, STM was used since it has some advantages compared to AFM. Most importantly, our AFM systems use optic feedback, which is disturbed by bubble formation at very negative potentials, as used in the studies shown. Furthermore, we have a lot of experience in *in situ* STM in ILs.[31,38,74–76]

In this thesis, all studies were performed with the IL *N*-methyl-*N*-proplypiperidinium bis(trifluoromethane)sulfonimide ([MPPip][TFSI]). This IL was designed for Li-ion batteries with a huge electrochemical stability window.[35] Nowadays, it is most often used for studies of the Li deposition.[31,77–80] In the last years, we performed several studies with this IL, especially metal deposition from this IL, at our institute.[31,74,81]

This work aims at gaining fundamental insights into the electrochemical processes in the IL

[MPPip][TFSI] in contact with a Au(111) electrode. In the first part of this work, the electrochemistry of [MPPip][TFSI] is studied by cyclic voltammetry to gain a potential dependent macroscopic understanding of the system. Hereby, different types of electrochemical behaviour observed for a Au(111) surface in contact with different batches of this IL will be discussed. Then, various purification methods will be compared. The role of residual H_2O on the electrochemical properties will be studied by varying the H_2O content in the IL. Based on these measurements, possible explanations for electrochemical behaviour will be provided.

The focus of the second part of this work aims at gaining a more complete picture of the potential dependent restructuring processes on the Au(111) electrode in the IL [MPPip][TFSI] by *in situ* STM. Insights into the onset of the cathodic corrosion of Au(111) will be given, including the dependence of the H_2O content in the IL on this process. Furthermore, restructuring processes due to the adsorption and desorption of anionic adsorbates, namely the lifting and formation of the herringbone reconstruction, will be discussed. Then, other restructuring processes of the Au(111) electrode will be shown and related to possible electrochemical reactions.

The last chapter deals with the alkali metal deposition on Au(111) from [MPPip][TFSI]. Macroscopic and microscopic insights will be gained by cyclic voltammetry and *in situ* STM measurements. Hereby, a particular focus is set on the Na deposition, including the initial stages, the ongoing underpotential deposition (UPD) and bulk deposition. Finally, Li deposition will be discussed and compared to the Na deposition.

2 Theoretical Background

This chapter discusses the theoretical background of this work. First, the morphology and stability of the Au(111) electrode, which was used for all measurements, will be discussed. This includes a detailed view of surface dislocations as the herringbone reconstruction lines and step edges. Furthermore, ionic liquids are introduced as the class of electrolytes used. A short overview of different concepts for the IL-electrode interface is given. Next, the principles of cathodic corrosion are presented, and the state of the art of cathodic corrosion in ILs is reflected. After that, the basic principles of metal deposition, comprising metal deposition from ILs, are discussed. At the end of this chapter, the methods mainly used for this study are described.

2.1 Au(111)

In fundamental research, it is of utmost importance to break down a complex system into smaller units which can be studied independently. In electrochemistry, often low-indexed single-crystal surfaces are used to get insights into the fundamental processes at the electrode-electrolyte interface.[56,58,82] Especially, Au single crystals are employed since it is relatively simple to prepare them reproducibly.[56,58] Au is considered to be chemically and electrochemically very stable and does not oxidise in air.[83–85] This makes it very valuable as an inert substrate and for every measurement that cannot be set up under an inert atmosphere, as the here described STM measurements.[56] Au exhibits a face-centred cubic (fcc) structure with atomic distances of 4.0786 Å.[14] Figure 2.1 a shows the unit cell of Au with the (111)-plane going through the blue-coloured atoms. This surface is the most densely packed and most stable surface and one of the most often used in electrochemical studies.[56,57] The atomic layers are arranged in an ABC order so that the positions of the atoms repeat every third layer.[16] This can be seen with the blue-, green-, and red-coloured atoms in Figure 2.1.

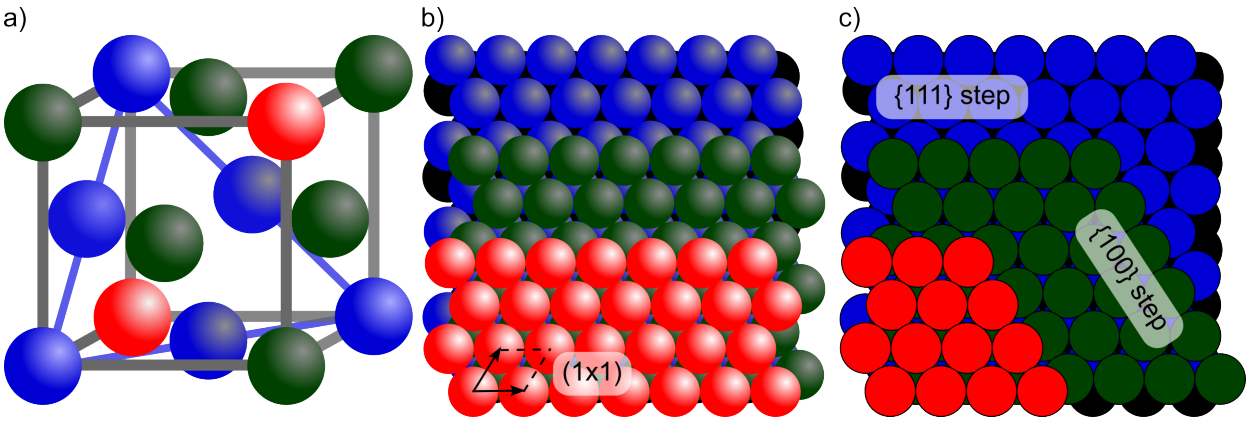

Figure 2.1: a) fcc unit cell with the (111) plane marked with blue lines which run through the blue-coloured atoms, b) (111) surface of the fcc crystal with the underlying layers and the (1x1) unit cell marked with black arrows at the bottom right, and c) (111) surface of the fcc crystal with the {100} and {111} steps marked. Derived from [56, 72, 86]

In Figure 2.1 b, the surface configuration is shown including the (1x1) unit cell, which is formed by a rhomb with lateral lengths of 4.0786 Å and an angle of 60 °.[14]

2.1.1 Steps and other Surface Defects

Real single crystal surfaces are much more complex than the simple scheme in Figure 2.1 b. Figure 2.1 c shows the possible step edges. If the atoms of the step are parallel with the atoms of the underlying terrace, it is a {100} step. If they alternate positions with the underlying atoms, it is a more stable {111} step.[56,86] Note that in some studies {100} and {111} steps are called A- and B-steps.[72] If a 120 ° angle is between two step edges, they are of a different kind, while 60 ° angles are between step edges of the same type.[86,87] Real surfaces show more defects than only steps. Figure 2.2 gives an overview of possible defects.[56,63,72,85] Some defects are induced by only one missing atom on the surface, which leaves a vacancy or one adatom on the terrace. These defects are categorised as point defects.[85] In other cases, more atoms are involved, and holes or islands form on the surface.[63,72] Steps and kinks are categorised as line defects.[85] Generally, all defects are characterised by atoms with a lower coordination number and, thus, higher reactivity than other surface atoms.[63,72,85] Another important type of surface defects are screw dislocations which are characterised by distortions of the crystal's periodicity.[63,85] In images of the surface, they appear as helical structures.[63]

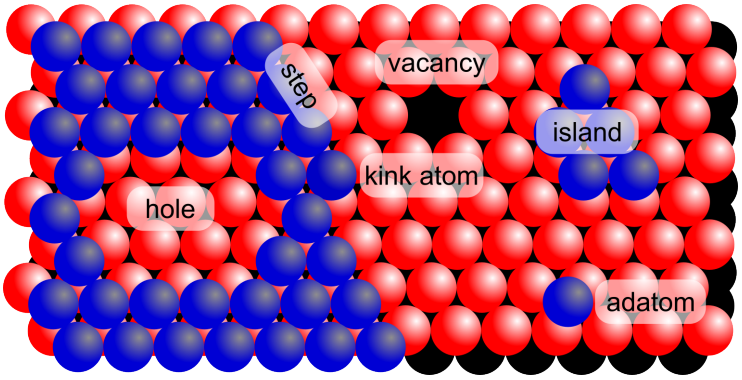

Figure 2.2: Possible surface defects on the Au(111) plane. Derived from [56, 72].

2.1.2 Reconstruction

The lower coordination of surface atoms compared with the bulk crystal can be compensated in two ways: i) Adsorbates that bind on the surface and ii) a rearrangement of the surface atoms, which leads to better coordination. This rearrangement of surface atoms is called surface reconstruction.[88,89] Since the atoms in the Au(111) plane are already densely packed, increasing the coordination by an in-plane rearrangement is impossible. Nevertheless, Au(111) reconstructs in contrast to other metal fcc-(111) surfaces.[87,88,90] The reconstructed Au(111) surface contains approximately 4 % more atoms than the bulk plains.[88,90,91] In one of the [110] directions, the surface layer is compressed so that 23 surface atoms are arranged in the same length as 22 bulk atoms.[88,90,91] If the surface atoms were equally distributed in one plane, only every 23rd surface atom would be positioned as a bulk fcc atom and between these fcc atoms would be one atom in the hcp (hexagonal close-packed) position.[90,91] In reality, most atoms are in fcc or hcp positions and only few atoms are at the bridge sites between the fcc and hcp regions.[91] Herby, more atoms are at the fcc positionas than on the hcp positions since they are energetically more favourable.[91,92] The atoms at the bridge sites form straight lines of an elevated height, the so-called discommensuration lines.[86] The unit cell of the reconstruction structure is usually described in relation to the bulk as (22x$\sqrt{3}$).[87,88,91] Another possibility is the description relative to the surface as a (23x3) structure.[91] The discommensuration lines are not straight over the entire surface but bend in 120 ° angles to spread the surface stress in all directions.[87] This pattern gives the reconstruction of the Au(111) surface the name herringbone reconstruction.[91,92] The sites at which the reconstruction lines bend are called elbow sites of the reconstruction. Only one of the double lines, called y-ridge, can bend straightly at

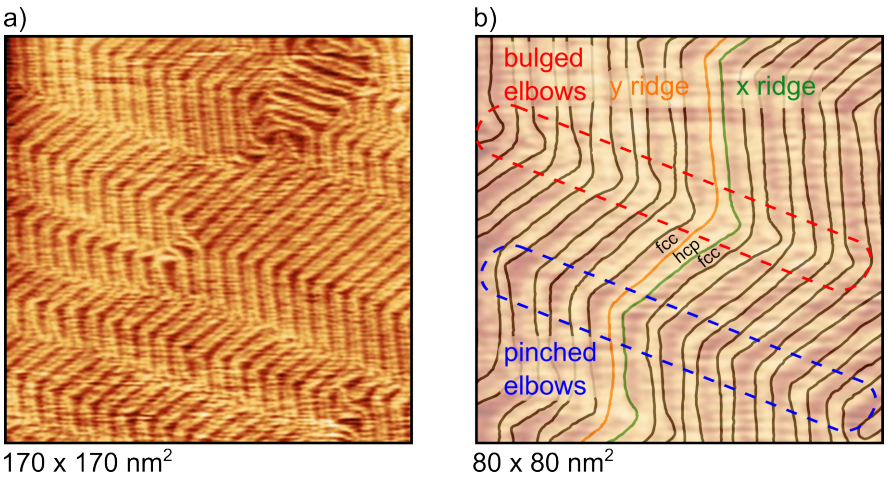

Figure 2.3: a) *In situ* STM image of the herringbone reconstruction of the Au(111) surface in a solution of 200 mM Na[TFSI] in [MPPip][TFSI] and b) zoom in this image with marked reconstruction lines including the y- and x-ridge, fcc and hcp areas, and the pinched and bulged elbows.

these elbows without changing the burgers vectors.[91] The other line, called x-ridge, is bent before and after the elbow, leading to pinched elbows where the hcp region between the lines is smaller than between straight lines and bulged elbows where the hcp region is larger.[91,92]

The reconstruction of the Au(111) surface is a unique phenomenon that occurs at high temperatures in air, other gases, or vacuum, or in the electrolyte at low potentials where the anions desorb from the surface.[88] This potential-induced reconstruction can only be observed for Au.[88] The formation and lifting of the reconstruction itself do not necessarily lead to a current. Still, usually, currents are induced by a change in the double-layer capacitance and anions ad- and desorption during the lifting and formation of reconstruction.[88] The shape of the reconstruction lines is not always uniform. It is highly dependent on the parameters with which they are formed.[89,93] For flame-annealing-induced reconstruction, the morphology depends on the annealing conditions; even slight deviations can lead to many elbows or straight lines without any elbows.[89] In Figure 2.3 a, the reconstruction lines are relatively uniform, but even here, some of the double-lines end in so-called U-connections[90] and others show crossings. Furthermore, the straight parts have different lengths. As in this image, there are often some domains in which the reconstruction lines are all parallel, but the domains differ.[90]

In electrochemical systems, the reconstruction can be lifted due to the adsorption of anions on the surface.[88,89] Since the reconstructed Au(111) surface has an excess of atoms of 4 %

compared to bulk layers, these atoms form islands on top of the surface.[88,89] For example, islands are formed by lifting the reconstruction in a sulphuric acid-based electrolyte.[88,89] In contrast, in the deep eutectic solvent ethaline, the surface mobility is increased by Cl^--ions and, thus, the excessive atoms diffuse to the step edges.[94]

2.2 Ionic Liquids

In general, an IL are a subgroup of the so-called "molten salts", which describe liquids purely composed of ions.[21,95] In contrast to molten inorganic salt, such as NaCl at high temperatures, they have melting points below 100 °C.[95–97] Most ILs are room-temperature ILs (RTILs) with melting points below room temperature.[53,98] This kind of IL is usually used in electrochemistry. Thus, in this context, IL is often used synonymously with RTIL.[95,99] This denotation is also used here. Typical ILs consist of a huge organic cation and an inorganic anion.[46,53,95,97] The low melting temperatures result from the asymmetry and long alkyl chains of the cation and the weak coordination of the anion, which prevent crystallisation at room temperature.[53,95] The organic cations are often aromatic or aliphatic heterocyclic compounds.[95,97] By combining the different cations and anions, many combinations are possible. Therefore, ILs cover many properties and can be designed accordingly.[46,97] Different kinds of categorisation for ILs exist. One possibility is to divide them into protic and aprotic ILs since their chemistry is significantly different.[95] Another classification is made between hydrophilic and hydrophobic ILs based on their miscibility with water.[29,47] The hydrophilicity is mostly determined by the anion since the cations are rather hydrophobic, so mainly the anion binds water in the IL.[29,47,100,101] Nevertheless, it is known that all ILs, including hydrophobic ILs, are hygroscopic.[29,47,102,103]

IL analogues are liquid compounds that have similar properties as ILs, but are not purely composed of ions.[104] Deep eutectic solvents (DESs) are an important class of such IL analogues. They comprise hydrogen bond acceptors, which are usually salts with huge nonsymmetric cations, *e.g.* choline chloride, and organic hydrogen bond donors, such as urea.[104] If the hydrogen bond donor and acceptor are mixed in the right ratio, they form an eutectic.[104,105]

ILs are used not only in electrochemistry but also as solvents for synthesis or biological and medical applications.[97,106,107] The multitude of possible applications originates in many beneficial properties, such as the small vapour pressure, non-flammability, a wide liquidus-range and thermal and chemical stability.[29,37,46,95,99] Additionally, ILs have high conductivities and

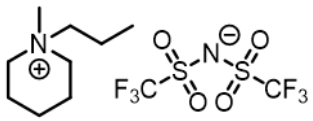

Figure 2.4: Structural formula of [MPPip][TFSI].

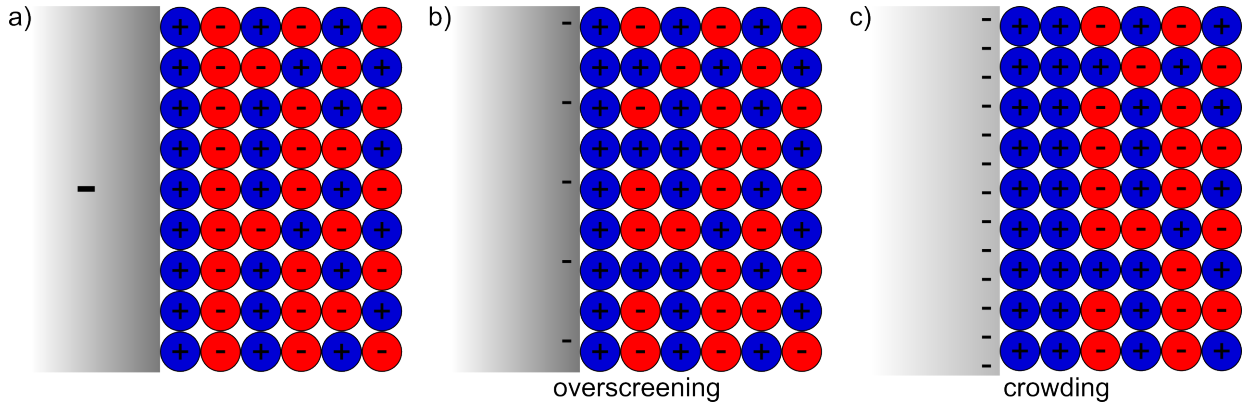

Figure 2.5: Different models of the IL-electrode interface: a) layer model, b) overscreening, and c) crowding. Derived from [37, 39, 118, 119].

often huge electrochemical stability windows, which is highly beneficial for electrochemical applications.[24,29,37,95]

In the studies shown here, the IL [MPPip][TFSI] was used, whose structural formula is shown in Figure 2.4. This piperidinium-based IL was first synthesised as an electrolyte to support Li deposition since a huge electrochemical stability window was expected.[35] The cation $[MPPip]^+$ (also $[MPPI]^+$, $[Pip_{13}]^+$, $[Pi_{13}]^+$, $[C_3MPip]^+$) is a constitutional isomer of $[BMPyr]^+$ (also $[Pyr_{14}]^+$, $[Py_{14}]^+$, $[BMP]^+$, $[C_4MPyrr]^+$). Therefore, [MPPip][TFSI] is very similar to [BMPyr][TFSI],[81,108] which is much more often used in electrochemical studies.Hereby, the properties of the pure IL[44,109–112] were studied as well as electrocatalytic reactions of gases,[113,114] the influence of impurities,[29,37,42,115–117] and metal deposition.[8,30,32,34] [MPPip][TFSI] was until now mostly used for Li deposition.[31,77–80] In our group, additionally, Mg and Zn were deposited from this IL.[31,74,81]

2.2.1 Ionic Liquid-Electrode Interfaces

Different models describe the ionic liquid-electrode interface. Generally, it is assumed that close to the charged electrode, the ions are arranged in layers of cations and anions whose order depends on the surface charge, while there is less order in the bulk electrolyte.[39,73,95] These ordered layers were observed by force-distance profiles measured with atomic force microscopy[109] and can be disrupted if water is in the electrolyte.[37] A simplified model for a negatively charged electrode is shown in Figure 2.5 a. The IL is assumed to be arranged in layers comprising both ions.[37,39,73] At the negatively charged electrode, the cations in this layer are arranged close to the electrode while the anions face the bulk electrolyte.[37,39,73] With increasing distance from the electrode, the order decreases.[37,73] The more complex models of overscreening and crowding comprise the charge compensation within the first layers and are shown in Figure 2.5 b and c for negatively charged electrodes.[118,120,121] In the case of overscreening, the adsorbed cations carry more charge than the electrode.[118,121] This overcompensation is then compensated in the next layer, where more anions are present than cations.[118,121] At higher electrode charges, not only the first ion layer is only composed of cations, but also the second layer. This phenomenon is called crowding.[118,121] Both models of the IL electrode interface were first proposed as theoretical models[118] and later observed experimentally, including the transition from overscreening to crowding by decreasing the electrode potential.[120] In some measurements with ILs and other concentrated electrolytes, the observed Debey length is higher than expected.[122] This effect is called underscreening, and a possible explanation is strong ion pairing.[123,124]

2.3 Cathodic Corrosion of Au

Usually, corrosion describes the dissolution of metals by oxidation. For noble metals under harsh conditions, reductive dissolution, called cathodic corrosion, is also possible.[125,126] In aqueous electrolytes, cathodic corrosion starts negative of the hydrogen evolution reaction's potential.[125] At these negative voltages, a water-free layer on the surface is formed, and hydrogen adsorbs on the electrode surface.[127,128] Following, negatively charged metal ions or clusters are dissolved from the surface to release the surface stress at these low electrode potentials.[126,129] The negatively charged ions or clusters are stabilised by adsorbed hydrogen and cations from the solution.[52,125,127] Hereby, only cations with low reduction po-

tentials, such as alkali cations, are able to stabilise the metal anions.[125,127,130] After dissolution, the formed complexes diffuse away from the electrode and out of the water-free layer. Thus, the metal anions are re-oxidised by water or other reactive species and agglomerate to nanoparticles.[127,131]

There are several conditions needed for cathodic corrosion to happen. For the formation of the water-free layer, the electrolyte must not be acidic.[127] Furthermore, the electrolyte should contain cations with low reduction potentials, such as alkali metal or ionic liquid cations.[125,127,132] Another important parameter is adsorbed hydrogen.[125,130,131] It was shown that no cathodic Au corrosion occurs if no water or other hydrogen source is present in the electrolyte.[126]

Cathodic corrosion is not limited to aqueous electrolytes. There are some studies in which the cathodic corrosion of Sn, Bi and Au was observed in an IL.[131–133] Hereby, *Lu et al.* suggested that the hydrogen needed for the cathodic corrosion is evolved by reduction of the cation of the IL,[131] whereas no such considerations can be found in the other studies.[132,133]

2.4 Metal Electrodeposition

Generally, the electrodeposition of metals can be described as the reduction of the metal cations from the electrolyte $\mathrm{M}^{n+}_{\mathrm{solution}}$ on the electrode to metals atoms adsorbed on the electrode $\mathrm{M}_{\mathrm{metal}}$ as given in Equation 2.1.[63,134] As depicted in the simple model in Figure 2.6, this process covers two steps: The adsorption of the metal cation on the surface and the following reduction. In this simplified model, the solvation of the cations in the electrolyte is neglected, though it is known to play an important role in real systems.[134,135]

$$\mathrm{M}^{n+}_{\mathrm{solution}} + ne^{-}_{\mathrm{metal}} \rightleftharpoons \mathrm{M}_{\mathrm{metal}} \tag{2.1}$$

If the electrode has the equilibrium electrode potential E_{rev}, this electrochemical reaction is in equilibrium.[63,134] Metal electrodeposition at electrode potentials positive of the equilibrium electrode potential is called underpotential deposition (UPD), while electrodeposition negative of this potential is called overpotential deposition (OPD).[134,136] The driving force for UPD is a favourable interaction between the electrode's material and the deposited metal.[134,136] Thus, the UPD stops as soon as the substrate is covered by that much of the deposited metal that no

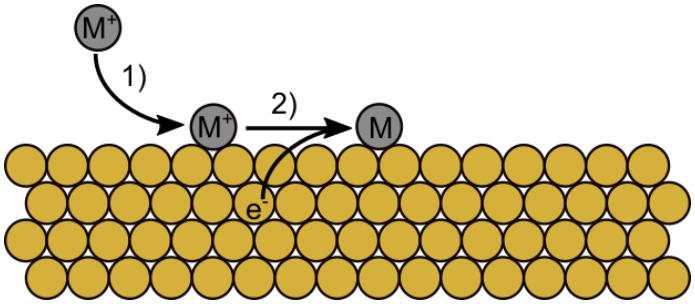

Figure 2.6: Simple model of metal electrodeposition for a single-charged metal cation. 1) The metal cation is adsorbed on the electrode. 2) The adsorbed metal cation is reduced.

favourable interactions are possible anymore. *E.g.* for Cu deposition on Au(111) from H_2SO_4-based electrolytes, this is reached with a monolayer coverage.[137,138] For the Ag deposition on Au(111) from H_2SO_4-based electrolytes a second monolayer can be deposited.[139]

While the UPD is mostly thermodynamically driven, the OPD happens at potentials at which electrodeposition is thermodynamically favourable.[134] Thus, the kinetics determine at which potential the OPD starts.[134]

Based on thermodynamics, three basic models describe the morphology of the electrodeposited material.[134,136] If interactions between the substrate and the deposited metal are unfavourable, the metal will grow in islands and not cover the whole substrate to prevent the unfavourable metal-substrate interfaces. This mode is called the Volmer-Weber growth mode.[63,134,136] For favourable interactions between substrate and metal, two other mechanisms are possible, which both begin with a monolayer coverage of the substrate. If the lattice constants of the substrate and the deposited metal are very similar, the metal growth continues in layers, called Frank-van der Merve growth mode.[63,134,136] Due to steric stress, this is impossible if the lattice constants differ. Therefore, the layer growth does not continue as soon as the steric stress becomes too high, but islands are deposited on the previously formed layers. This mode is called the Stranski-Krastanow growth mode.[63,134,136] For both Na and Li deposition on Au(111), this growth mode can be expected since it is known that Au and Na/Li interact favourably, while their lattice constants differ.[14,140,141] The discussed models are based on the assumption that the substrate is static. Nevertheless, metal deposition can lead to an immediate place exchange between the substrate and the deposited metal, forming a surface alloy.[63]

2.4.1 Metal Deposition on the Reconstructed Au(111) surface

As mentioned above, the Au(111) surface should not be seen as a flat layer due to the manifold surface defects, which are usually more reactive than the flat terraces.[63,72,85] Additionally, many metals deposit at quite negative potentials where the ($\sqrt{3} \times 22$) reconstruction is present.[142,143] This surface reconstruction can have a huge influence on the deposition as carried out by many studies of electrochemical metal deposition and metal deposition in ultra-high vacuum (UHV): In UHV, Pd,[91,144] Ni,[145,146] Co,[147–152] Rh,[153] and Mo[154,155] are preferably deposited at the elbow sites of the reconstruction lines. In contrast, for Ag,[156] Cu,[146] Al,[157,158] and Na[159,160] such structures were not found. Preferred electrodeposition at the elbow sites of the reconstruciton lines was reported for Ni[142] and Co.[143,161] For UHV conditions, the tendency for a preferable deposition at the elbow sites can be made by comparing the surface free energy and heat of sublimation of the deposited metal and Au.[146] It seems that if both energies are higher for the deposited material, nucleation happens preferably at the elbows of the reconstruction lines.[146] In UHV, the process of Ni deposition is described to start with a place exchange of the deposited metal with Au atoms at the elbows, which have different coordination numbers from the other atoms on the surface.[146]. Ni is deposited on top of the exchanged atom in the second step.[146] The same mechanism is proposed for electrochemical Ni deposition, where the Ni also preferably deposits at the reconstruction elbows.[142] Note that not all elbows are the same. There are pinched and bulged elbows, and *e.g.* for the Pd deposition in UHV, preferred deposition at bulged elbows was observed.[91]

2.4.2 Metal Deposition from Ionic Liquids

Metal deposition from ionic liquids has several advantages compared to aqueous electrolytes. The huge electrochemical and chemical stability allows the deposition of metals with very negative reduction potentials, which react with water as alkali and earth alkali metals.[162] Additionally, many metals such as Zn, Ni or Co deposit at potentials negative to the potential of the hydrogen evoltuion reaction (HER) so that both reactions take place in parallel in aqueous electrolytes.[14,163] This can be prevented using non-aqueous electrolytes. Hereby, ILs have the advantage over standard organic electrolytes that their conductivity is much higher.[162]

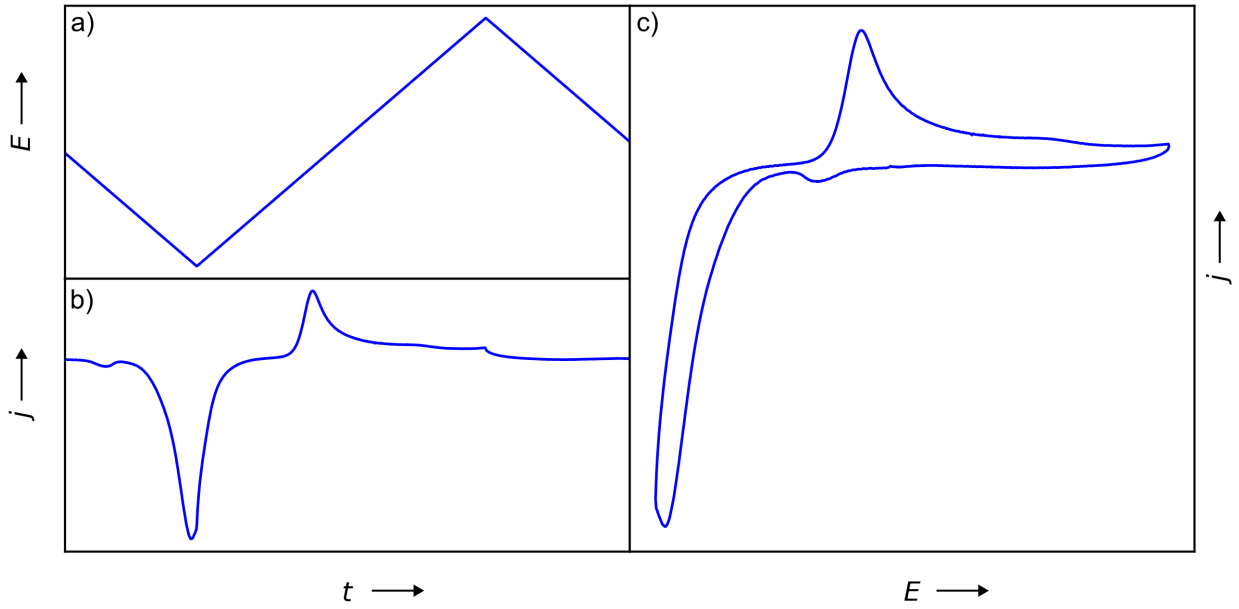

Figure 2.7: a) Potential-time curve, b) current density-time curve and c) current density-voltage curve during measuring a cyclic voltammogram.

2.5 Cyclic Voltammetry

Cyclic voltammetry is one of the most commonly used methods to get a first idea about the processes happening in an electrochemical system.[63,64] Figure 2.7 shows how a cyclic voltammogram (CV) is recorded. With time t, the applied voltage between the working electrode and the reference electrode, and thus, the potential of the working electrode E, is changed linearly (here, first negative-going) until the limiting potential of the working electrode is reached. Then, the scan is continued with the same scan rate in the other direction (here, positive-going) until the second limiting potential is reached. Here, the scan direction changes again, and the the scan is continued until the end potential is reached, which is often identical to the initial potential.[63–65] A typical potential course is shown in Figure 2.7 a. At the same time, the current or current density j between the working electrode and the counter electrode is measured as a response signal shown in Figure 2.7 b. In the CV, the current or current density response is plotted over the applied electrode potential, as shown in Figure 2.7 c.[63–65] The currents measured in the CVs can have different origins, such as the charging of the electrical double layer, adsorption of ions or electrochemical (Faradaic) reactions as the reduction or oxidation of species from the electrolyte or the electrode's material.[63,68,164] Depending on the

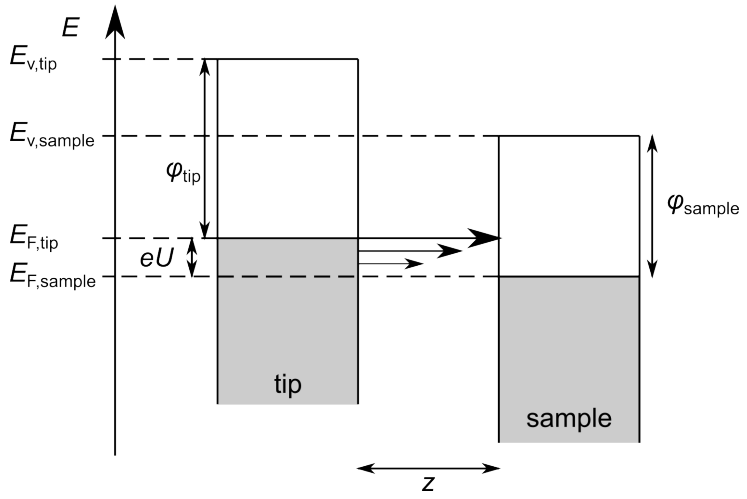

Figure 2.8: Scheme of the tunnelling from a negatively biased tip to a positively biased sample with the including the electronic levels of the tip and the sample. Derived from [146, 165].

system, the anode or the cathode is defined as the negative electrode. In this work, reduction processes that induce a negative current will be called cathodic, and the peak names will start with C. In the same way, oxidative processes that induce a positive current will be called anodic, and the peak name will start with A. Typical peaks of Faradaic reactions are shaped like the anodic peak in Figure 2.7. At the beginning of the process, the current density rises exponentially, caused by the kinetical limitations at small overpotentials called Buttler-Volmer behaviour. The current decreases again in the following since the process is limited by the diffusion of educts to and products from the electrode.[66,134]

2.6 *In situ* Scanning Tunnelling Microscopy

Scanning tunnelling microscopy (STM) is a powerful technique which uses a tunnelling current to image conductive surfaces down to the atomic scale.[166,167] A tip is brought close to the investigated electrode, and a voltage is applied between the tip and the electrode.[166,167] Figure 2.8 shows a scheme of the electron tunnelling from a negatively charged tip to a positively charged sample. Due to the applied voltage U, the Fermi level of the tip $E_{\mathrm{T,tip}}$ has a higher energy level than the Fermi level of the sample $E_{\mathrm{T,sample}}$.[146,165] If the distance between the tip and the electrode z is sufficiently small, electrons from levels between the Fermi level

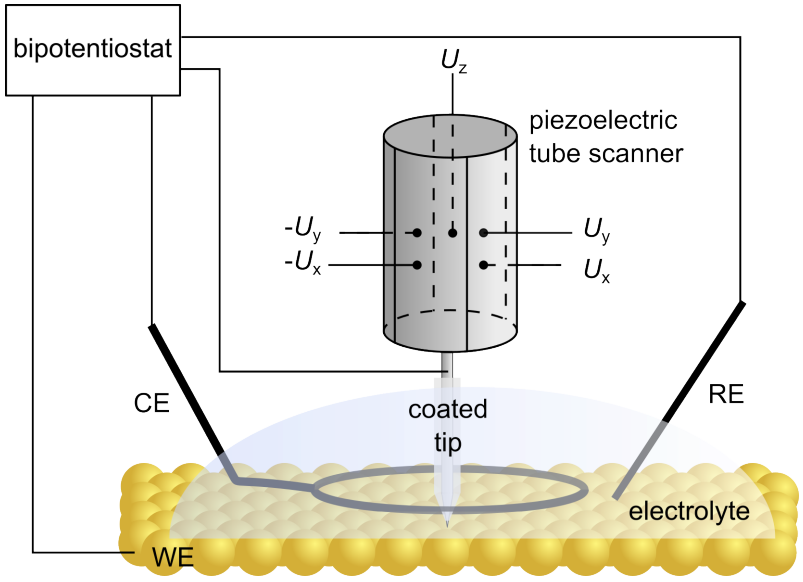

Figure 2.9: Schematic image of the *in situ* STM set-up with the piezoelectric tube scanner, isolated tip, electrolyte, RE, CE, WE and bipotentiostat. The cell compartment is not shown in this simplified image. Derived from [71, 169].

of the tip and the sample can tunnel to the unoccupied levels of the sample.[146,165] Hence, a tunnelling current can be measured.[146,165–167]

The proportionality of the tunnelling current I_T to the distance between tip and electrode and the applied voltage U_T is given in Equation 2.2 with the reduced Planck constant $\hbar$, the tunnelling barrier ϕ_T, and the electron's mass m_e.[59,165,168]

$$I_\mathrm{T} \propto U_\mathrm{T} \exp\left(-\frac{2z\sqrt{2m_\mathrm{e}\phi_\mathrm{T}}}{\hbar}\right) \tag{2.2}$$

Piezoelectric elements enable accurate scanning of the STM tip at a subnanometre scale.[168] Hereby, either the z-position of the tip is kept constant, and the tunnelling current is measured (constant height mode), or a feedback loop is used to vary the z-position of the tip in a way that the tunnelling current is kept constant (constant current mode).[146,169]

Often, the STM is used in UHV, but it is not restricted to these conditions.[59] Modifying the set-up as *e.g.* shown in Figure 2.9, *in situ* STM measurements in electrochemical systems are also possible.[59,71,169] To control the voltage between the working electrode and the reference electrode and the voltage between the working electrode and the tip, a bipotentiostat is

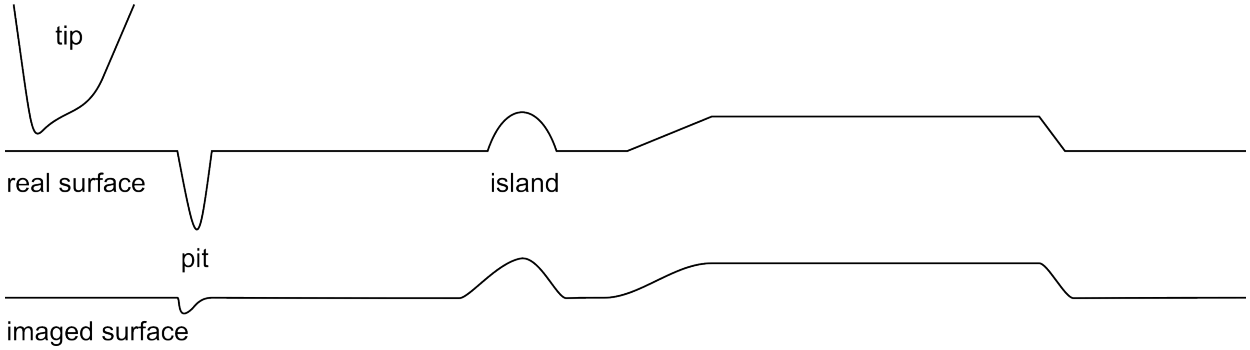

Figure 2.10: Comparison of the image of the surface with the real surface for an asymmetric tip. Derived from [146].

needed.[59] Furthermore, the tip, except the topmost part, needs to be covered with an insulating layer. Otherwise, it would act as a fourth electrode and Faradaic currents in the range of µA–mA would be measured, which are much higher than the typical tunnelling currents in the range of pA–nA.[59] With these adaptions, a direct observation of processes on the electrode surface is possible. Applications vary from the imaging of adsorption layers in the atomic scale in aqueous electrolytes,[59,170] ionic liquids,[44,61] or deep eutectic solvents,[94] to macroscopic changes of the surface as the formation and lifting of the reconstruction,[59,94] oxidation[171–173] of the electrode or metal deposition.[32,59,74,143]

Other scanning probe techniques used in electrochemistry include atomic force microscopy (AFM), scanning electrochemical microscopy (SECM), and scanning electrochemical cell microscopy (SECCM).[71,174] For getting topographic information of the electrode's surface *in situ*, usually, STM or AFM are used. Hereby, the AFM has the advantage that the probe interactions are the mechanic forces between the sample and the tip.[71,174] Therefore, the image gives a real topography, while STM gives an image of constant tunnelling probability.[71,169,174] For metal surfaces, it can be assumed that the surface of constant electron density resembles the topography.[169] Therefore, this difference is barely an issue in measurements on metal electrodes. Another advantage of AFM is that it is not restricted to conductive surfaces like STM.[174]. Non-conductive structures on electrodes, such as the solid-electrolyte interphase, can be studied by AFM.[175–177] However, most electrochemical studies are conducted at conductive samples. The advantages of the STM are the ease of tip preparation and the rather robust feedback loop.[59,178] In the AFM, the position of the tip is often tracked by an optical sensor.[71,174] This is sensitive to changes in the refractive index at gas-liquid phase boundaries and thus for bubble formation.

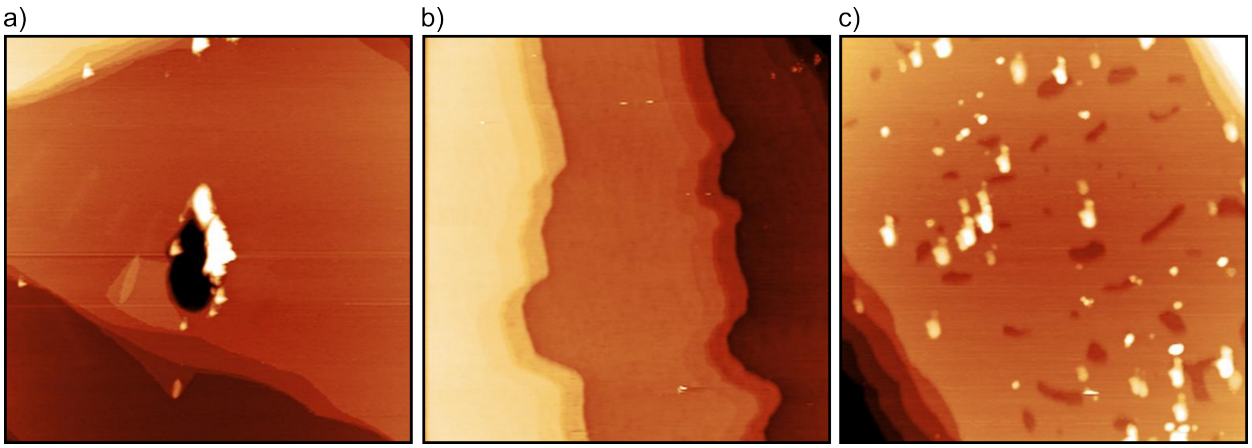

Figure 2.11: Typical artefacts during *in situ* STM measurements. a) A hole in the surface induced by a tip crash, b) a threefold tip which images the step edges threefold, and c) a multiple tip whose shape is imaged at the islands.

The image obtained with scanning probe techniques always represents the interaction between the tip and the studied surface.[179–181] Therefore, the geometry and size of the tip play a crucial role in the resolution of the images and can lead to various artefacts.[179–181] For instance, if the tip is very broad and asymmetric, the imaged surface will deviate from the actual surface, as shown in Figure 2.10. These effects are known as tip convolution effects.[180,181] If pits are narrower than the tip width, they cannot be imaged with the correct depth. Whereas larger pits or islands are measured with the actual height, their shape is not correctly resolved due to the asymmetry of the tip.[179–181] In *in situ* STM measurements, the tip is often changed during the measurement. This might be caused by unavoidable crashes on the surface or electrochemical reactions at the tip. Figure 2.11 shows some typical artefacts seen in measurements.

In Figure 2.11 a, a typical artefact of a tip's crash into the surface is imaged.[182,183] A considerable hole has formed in the centre of the image. Next to it, there are huge deposits of the material that have been pushed aside. The quality of the image is excellent since now Au atoms cover the topmost part of the tip, which improves its quality.[182,183] Figure 2.11 b shows how a threefold tip images step edges. Each step edge is imaged three times.[179] Similarly, Figure 2.11 c shows the image of a multiple tip. Herby, only the islands are imaged many-fold. Furthermore, all islands show the same shape, which indicates that the shape of the islands is not imaged but the shape of the tip.[152] Note that the interaction between tip and sample does not only lead to visible artefacts. The tip can also move material over the surface, prevent

deposition or dissolution in the imaged area or lead to a preferred deposition or dissolution by perturbations in the electrochemical double layer.[169]

3 State of the Art

3.1 Impurities in ILs

Several studies have shown impacts of different impurities on the electrochemical behaviour of ILs.[45,51,53,184,185] Typical impurities include residual water and oxygen as well as alkali cations, halides and organic compounds which originate from the IL's synthesis.[45,51,53,116] The impurity most discussed for electrochemical measurement is water which will be discussed in more detail.

Generally, all ILs are hygroscopic and it is commonly accepted that the water content is a parameter which should always be monitored.[29,37,42,47,50,115,184,186–188] It could be shown that residual water in ILs usually accumulates at the electrode-electrolyte interface of the negatively charged electrodes.[29,42] For hydrophobic ILs, it also accumulates at the electrode-electrolyte interface of positively charged electrodes.[29,42] Only on neutral or slightly positive electrodes water depletion from the electrode-electrolyte interface could be observed.[42,188]

The presence of water in the ILs significantly reduces their electrochemical stability window.[37,51,115,116] At the electrode-electrolyte interface, it prevents the formation of layers of the ionic liquid, as described previously.[29,37] It is worth noting that water interacts stronger with the anions than with the organic cations.[42] In the bulk electrolyte, water does not affect the IL's structure as soon as its concentration is low. Only at high water concentration, water clusters form in the electrolyte and interrupt the ordering of the IL's ions.[189]

For reducing the water content, ILs are typically dried with heat and vacuum.[38,44,45,115,190–193] To reduce the water concentration even more, molecular sieves can be used which absorb water.[81,191,194] These molecular sieves consist of different types of zeolites depending on the desired pore size.[195]

3.2 [MPPyr][TFSI] on Au(111)

Some parts of this section have previously been published in the article "Reproducibility of electrochemical measurements with ionic liquids: Is the water content the decisive parameter?".[60]

Most electrochemical studies of ILs have a focus on electrochemical processes of other compounds dissolved in the IL, such as metal salts[8,30–32,34,196] or reactive gases.[52,113] Some studies focus on pure IL in contact with metal electrodes. The Au(111) electrode is especially often used for these fundamental studies due to the abovementioned advantages.[44,61,109,191] Comparing the different studies, it becomes evident that the data obtained for the same systems are often quite different. Figure 3.1 shows a comparison of cyclic voltammograms obtained for Au(111) in the IL [BMPyr][TFSI] with a scan rate of $10\,\mathrm{mV\,s^{-1}}$ extracted from different studies.[32,44,61,109] Since all measurements were performed with other reference electrodes, the CVs were aligned using features occurring in all of them.

The curves are not very similar despite the two peaks on which all CVs were aligned. This is partially reasoned by the differences in the potential limits. Unfortunately, only *Wen et al.* showed experiments with different potential limits.[61] The CV of *Atkin et al.*[109] (Figure 3.1 a) showed a CV for a huge potential window. At potentials negative of the first cathodic peak in all measurements, more cathodic peaks appear until at approx. $-3\,\mathrm{V}$ *vs.* $\mathrm{Fc/Fc^+}$ the current decreases exponentially. This was referred to as the cathodic decomposition of the electrolyte, whereas the other cathodic features are assigned to adsorption processes. The peaks in the following positive-going scan are consequently assigned to processes involving the decomposition products. *Gasparotto et al.*[32] have chosen a smaller potential window. The lower potential limit is only slightly negative of the cathodic peak, which was present in all measurements. Therefore, in the following positive-going scan, the current density is much lower than in the measurement of *Atkin et al.*[109] and fewer peaks are visible. The peaks are assigned to surface restructuring and charging of the double layer. *Wen et al.* reported different potential limits, of which two are shown. One of them is similar to the limits chosen by *Gasparotto et al.*[32] and *Rudnev et al*,[44] the other to that of *Atkin et al.*[109] In the CV with the smaller potential window, two cathodic peaks and two anodic peaks are visible. The changes in the potential limits revealed that the anodic peak visible in all shown measurements is related to the cathodic peak visible in all measurements. Using video STM, the cathodic peaks could be related to changes in the adlayer of cations. The CV measured by *Rudnev et al.*[44] shows a

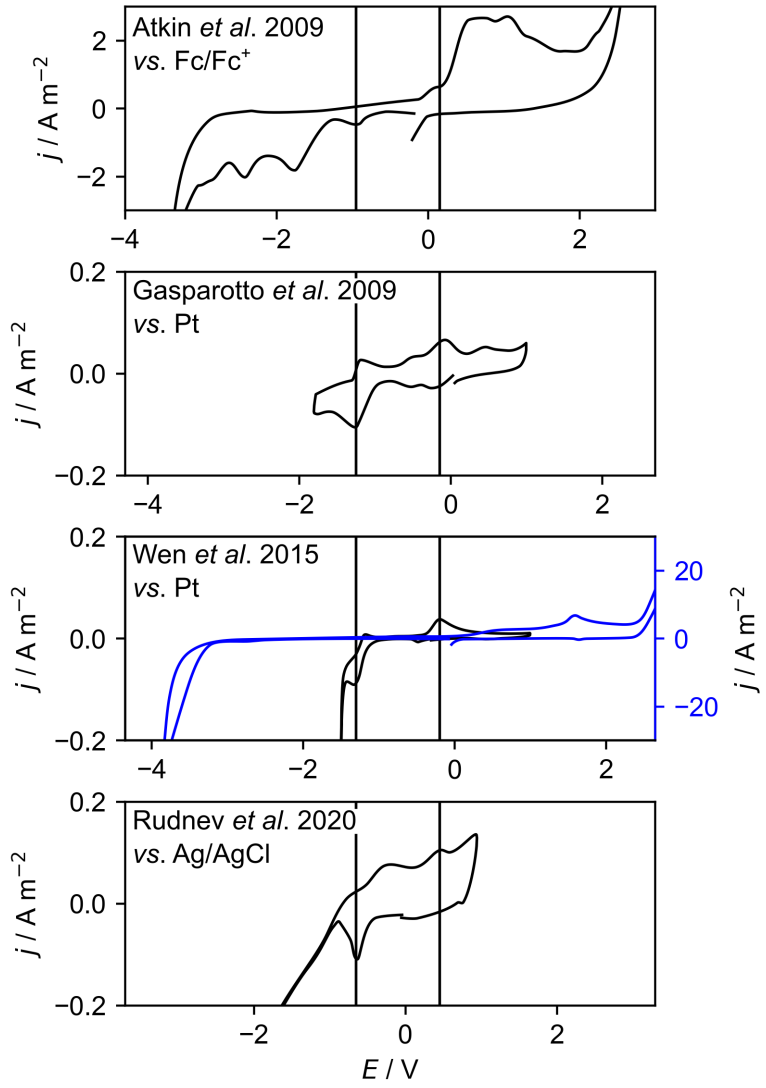

Figure 3.1: CVs for Au(111) in [BMPyr][TFSI] as reported by *Atkin et al*,[109] *Gasparotto et al*,[32] *Wen et al*,[61] and *Rudnev et al*.[44]. The scan rate was always 10 mV s^{-1}.

linear decrease of current density at potentials negative of the cathodic peak in all measurements. Despite this, it is similar to the CV from *Gasparotto et al.*[32] The peaks were not further explained, but the *in situ* STM measurements of the respective potentials did not show any significant structural changes.

The comparison of these studies underscores the challenges in the field of electrochemistry of ILs. The data and explanations provided are highly diverse, reflecting the complexity of the subject. This diversity is further exacerbated by the absence of commonly accepted standardised reference electrodes, such as the standard hydrogen electrode for aqueous measurements.[197] These challenges highlight the need for further research and standardisation in this area.

3.3 Alkali Metal Deposition from ILs

There is a huge variety of studies about the alkali metal deposition from ILs, usually with a focus on Li and Na.[6,8–10,15,30–33,196,198–200] For this work, two aspects are crucial: The reduction potentials of Na and Li in ILs and the initial stages of Na and Li deposition. They will be discussed in the following.

In some studies in $AlCl_3$-based ILs, it was observed that the Na deposition occurs at more negative potentials than the Li deposition.[198,199] Such effects can be explained by stronger solvation of Na in the respective electrolyte.[198,199] Additionally, it was observed that the coordination of Na with $[TFSI]^-$-anions is stronger than the coordination of Li with $[TFSI]^-$-anions, since Na-ions are bigger.[135] *Monti et al.* could show that Na^+-cations are coordinated by three $[TFSI]^-$-anions, while Li^+-cations are coorinated by only two. It could be expected that similar trends than observed in $AlCl_3$-based ILs could occur for $[TFSI]^-$-based ILs. However, in [BMPyr][TFSI], such effects were not observed.[15] Generally, it is discussed that developing a galvanic series under standardised conditions for ILs or deep eutectic solvents would be beneficial to elucidate such anomalies.[201]

Most Li and Na deposition studies from ILs focus on bulk deposition.[8,30,34,36] Nevertheless, there is a limited number of studies that image the initial stages of Li electrodeposition.[31,32,196] These studies have been performed by *in situ* STM on a Au(111) surface using different hydrophobic ILs.[31,32,196] *Berger et al.* used the IL [MPPip][TFSI] and observed an island deposition during the UPD followed by bulk deposition at overpotentials.[31] Furthermore, current-less

restructuring phenomena were observed after the deposition, which could be the initial stages of dendrite formation.[31] *Gasparotto et al.* deposited Li from [BMPyr][TFSI] and reported that the UPD comprised two monolayers or even more.[32] They expected an alloy formation which co-occurs to the Li deposition.[32] *Hu et al.* used an imidazolium-based IL and reported the formation of an SEI (solid electrolyte interphase) during the deposition due to decomposition of the electrolyte.[196]

4 Experimental

In this chapter, first, the preparation methods of the used chemicals and materials are described. Then, the experimental setups and procedures are shown. In the end, a list of all used chemicals, including their origin and purity, is given.

4.1 Preparation and Cleaning of the Electrodes

4.1.1 Au(111) Working Electrode

Before every measurement, the Au(111) working electrode (WE) was annealed in a *Carbolite CWF 1200* muffle furnace at 960 °C for at least 2 h. No temperature control during the following cooling phase was possible, but typically, the oven needed ca. 5 h to cool down to 60 °C. After this treatment, minor surface defects healed, and the herringbone reconstruction was observable. Before *in situ* STM measurements, the Au(111) crystal was additionally flame annealed in a butane flame for 2 min and cooled down in N_2-atmosphere.

After the electrochemical measurements in the IL-based electrolytes, the crystal was rinsed with acetone to remove the IL. Residual organics were removed by immersion into 65 % HNO_3 for at least 30 min. Afterwards, the crystal was rinsed with ultra-high purity (UHP) water to remove the HNO_3.

After measurements where Au oxidation could not be excluded, the crystal was additionally immersed for some minutes in HCl to remove possible oxides. Afterwards, it was rinsed with UHP water.

If visible dirt was still present after these treatments (*e.g.* after measurements including bulk alloy formation or IL decomposition), the crystal was additionally immersed into Caroic acid (H_2SO_4:H_2O_2, 3:1) for 30 min and boiled out in UHP water three times afterwards. If this

treatment did not remove the dirt, the crystal was additionally electropolished in 0.1 M H_2SO_4 at 5 V for some seconds, immersed in HCl and then rinsed with UHP water.

Before placing the crystal in the muffle furnace, it was always rinsed with UHP water and dried in a N_2-stream.

4.1.2 Pt Counter Electrode

For all measurements, a Pt wire served as a counter electrode (CE). Before the cell assembly, it was annealed in a butane flame and cooled in air. After each measurement, it was rinsed with acetone.

4.1.3 Reference Electrodes

In the shown studies, we have selected the reference electrodes (REs) depending on the system under investigation. We used a homemade Zn/Zn[TFSI]$_2$-electrode for electrochemical measurements of electrolytes without metal salts. All electrochemical measurements with a Na[TFSI] containing electrolyte were performed using a Na-rod as RE, which was cut from a large Na piece on the verge of measurement to prevent the formation of a passivating oxide layer. All *in situ* STM measurements and the electrochemical measurements with Li[TFSI] containing electrolytes were performed using an $AlPO_4$-coated Al wire since, in both cases, a set up under an inert atmosphere, respectively Ar atmosphere for Li was not possible.

Zn/Zn[TFSI]$_2$

The used Zn/Zn[TFSI]$_2$-RE was an electrode of the second kind, which means that it has a huge potential stability.[197] It was homemade in a 3D-printed housing of polyvinylidene fluoride with a magnesia stick as a frit.[197] The housing was filled with solid Zn[TFSI]$_2$ and a concentrated solution of Zn[TFSI]$_2$ in [MPPip][TFSI].[197] This solution was contacted with a Zn wire which was freshly grinded before immersion.[197] The electrode was sealed with a heat shrink tube and stored in [MPPip][TFSI].[197] After each measurement, it was carefully rinsed with acetone. This electrode proved to have a very stable potential at –0.65 V *vs.* Fc/Fc$^+$.[197]

Na

For the Na deposition measurements, a Na rod was used as a RE. The sodium was stored in large pieces in the glovebox under paraffin oil. Prior to the measurement, a small rod was cut from these pieces to remove the oxidised surface. It turned out that despite this treatment, the measured potential was 100–200 mV positive of the real Na/Na^+-potential. Therefore, the measurements were, in the end, calibrated on the occurring peaks. Despite that, the potential was very stable without significant shifts throughout a measurement. After the measurement, the Na rod was dissolved in propan-2-ol and water.

Al/$AlPO_4$

For all measurements in which the above-mentioned REs were not applicable, $AlPO_4$-coated Al wire was used. This electrode was prepared by immersing an Al wire first for 5 min into an aqueous KOH solution to dissolve surface oxides. Afterwards, the wire was immersed for 5 min in 85 % H_3PO_4 to form an $AlPO_4$ layer on the surface. This electrode showed high stability during a measurement, but the potential varied between different measurements independent if a freshly prepared electrode or an already used one was used. Nevertheless, for every measurement a new electrode was prepared. After the measurements, the potentials were always converted to $Zn/Zn[TFSI]_2$ for measurements of the pure IL, or Na/Na^+, respectively, Li/Li^+ for the alkali metal deposition measurements.

4.2 Electrolyte Preparation

4.2.1 Preparation of the Pure IL

For measurements with the pure IL, three different approaches were used: As-received, vacuum-dried, and molecular sieve-dried. The as-received ILs had a water content between 5 ppm and 100 ppm, which was dependent on the supplier. For vacuum-drying, the IL was transferred in either a Schlenk-tube or a vial and vacuum-dried at 60 °C and 1×10^{-3} mbar overnight. This resulted in a water content of ca. 15 ppm in Schlenk-tubes and 50 ppm in vials. For the treatment with a molecular sieve, a molecular sieve with a 4 Å pore size was

added to the IL before vacuum-drying. Afterwards, the molecular sieve remained in the IL during the storage. This procedure yielded reproducibly a water content below 5 ppm.

A table including all pretreatments of the electrolytes for each measurement is included in the Appendix (Table A.1-A.2).

4.2.2 Preparation of the Electrolytes for Na and Li Deposition

The electrolytes for the alkali metal deposition were mixed in a glovebox with N_2-atmosphere. Afterwards, they were transferred to a Schlenk-line and vacuum-dried as described for the pure ILs. This was always done in a Schlenk-tube since the residual water for the alkali electrodeposition electrolytes should be as small as possible.

4.3 Cleaning of the Equipment

All cells used for electrochemical measurements or *in situ* STM measurements were chemical resistant and made of either Teflon or Kel-F. After each measurement, they were rinsed with acetone and UHP water before immersing them for at least 12 h in Caroic acid. Thereafter, they were rinsed with UHP water and boiled out in UHP water five times before drying them in an oven.

4.4 Karl Fischer Titration

Karl Fischer Titration was used to determine the water content of the ILs. The Karl Fischer coulometer *851 Titrando* by *Metrohm* was used with the respective reagent and software.

4.5 XPS Measurements

XPS (x-ray photoelectron spectroscopy) measurements were performed by PD Dr Joachim Bansmann at the Institute for Surface Chemistry and Catalysis (IOK). The spectra were

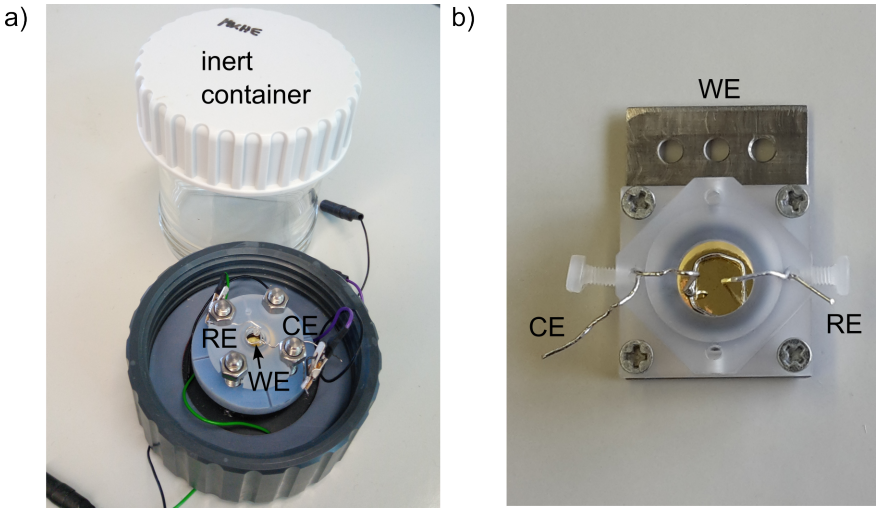

Figure 4.1: Miniaturised cells for the electrochemical measurements: a) Homemade cell including an inert container and b) electrochemical cell for measurements in the glovebox.

recorded with a *PHI 5800* spectrometer using a monochromatic Al K_α x-ray source (1486.8 eV). The sample was connected to the ground potential, and pass energies of 93.9 eV, respectively 29.35 eV were used for survey and detail spectra. For the comparison of the different batches of IL, a droplet of each batch was placed on a Cu foil, which was used as supporting material. A Au sheet was used for the deposition of Na from the molecular sieve for XPS and as support for the droplet of the molecular sieve-treated IL.

4.6 Electrochemical Measurements

Since the electrochemical behaviour of ionic liquids is dependent on the atmospheric conditions, especially on moisture and oxygen, all electrochemical measurements were performed under an inert atmosphere.

All Li deposition measurements were performed in a homemade miniaturised cell shown in Figure 4.1 a.[197] The Au(111) WE was mounted with an O-ring of an inner diameter of 0.7 cm at the bottom of the cell. RE and CE wires were mounted at the side. For the Li deposition measurements with 10 mM, the cell was prepared in an Ar-filled glovebox, including electrolyte addition. Afterwards, the cell was closed and transferred from the glovebox to a *Biologic VSP*

potentiostat. For Li deposition measurements with 200 mM Li[TFSI], the cell was assembled in air and the cap of the inert container was replaced by a cap which could be connected with a Schlenk adapter. Before adding the electrolyte, the cell was purged with Ar, and the electrolyte was added under Ar counterflow to prevent exposure to air. The measurement was performed with a *Biologic SP300* potentiostat.

All other measurements were performed in a N_2 filled glovebox (*MBRAUN LABstar*) with a H_2O and O_2 content below 0.5 ppm using a *Zahner IM6* potentiostat and the corresponding *Thales* software. The Au(111) WE was mounted with an O-ring of an inner diameter of 1.185 cm in a miniaturised electrochemical cell which is shown in Figure 4.1 b. RE and CE wires were mounted at the sides of the cell. The Na rod and the Zn/Zn$[TFSI]_2$ RE were dipped into the cell from above.

4.7 Scanning Tunnelling Microscopy

4.7.1 Tip Preparation

All tips were prepared from a Pt/Ir wire (80:20). They were first etched in an aqueous 5 M solution of NaCN and then coated with high-density polyethylene (HDPE) as described in detail below.

Tip Etching

Note that the following procedure must not be repeated without sufficient safety precautions. Tip etching was performed in a fumehood since HCN formation during the etching process is unavoidable. Additionally, any contact with NaCN was carefully avoided. A scheme of the set-up used is shown in Figure 4.2 a. The Pt/Ir wire was cut into pieces of ca. 3 cm, which were connected with a crocodile clip to an AC (alternating current) power supply and vertically mounted. The CE was a loop of a platinum wire which was placed around the Pt/Ir wire. Hereby, the following aspects were important: i) The loop should be positioned around the middle of the Pt/Ir wire. ii) The Pt/Ir wire should cross the centre point of the loop. iii) The loop should be as horizontal as possible (the least possible deviations from the x-y-plane).

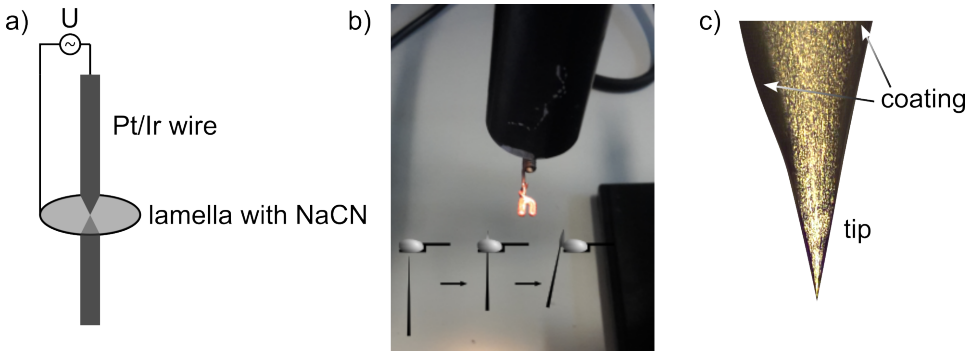

Figure 4.2: STM tip preparation: a) Scheme of the tip etching station, b) hot fork for the coating with HDPE and schematic drawing of the tip coating, and c) microscopic image of the resulting etched and HDPE-coated STM tip.

After adjusting the electrodes, a lamella of the 5 M NaCN solution was formed in the loop of the CE by placing a Becher of the solution underneath. After removing the Becher, a small container was placed underneath the electrodes to catch the lower tip as soon as it fell down. Etching was done with the AC power supply according to the parameters shown in Table 4.1. The timer was stopped, and the lamella was renewed as soon as the lamella broke down or after 2 min if it did not break down. As soon as the lower tip fell off the upper part by gravitation, the CE was quickly removed to stop further etching of the upper part.

Table 4.1: Tip etching parameters.

U **/ V**	***t*** **/ min**
11.8	1
8	4
5.6	until oscillation
4	until tip falls down

The etched tips were carefully rinsed with UHP water to remove all leftovers from the NaCN solution.

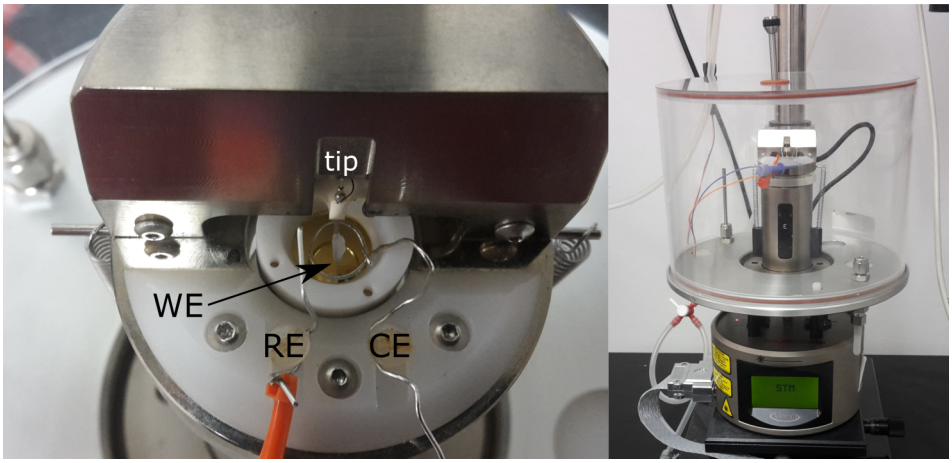

Figure 4.3: STM setup: Detailed view of the miniaturised electrochemical cell and the tip and image of the whole setup with the inert container.

Tip Coating

All STM tips were coated with high-density polyethylene (HDPE). The set-up for the tip coating is shown in Figure 4.2 b. A fork built from a wire was connected to the tip of a soldering station with temperature control. The temperature was set to 270 °C. As soon as this temperature was reached, residual HDPE from the last coating procedure was removed. Then, another HDPE pellet was placed on the fork. After waiting ca. 2 min until the pellet was completely molten, the tip was pulled through the HDPE. Herby, only the part which should be coated was pulled through the HDPE. By removing the wire from the HDPE, the HDPE pulls threads which can be removed by stripping them off at the hot fork. After coating the tips, it is advantageous to leave residuals of HDPE on the fork to protect it from dust.

A microscopic image of the etched and coated tip is shown in Figure 4.2 c. The HDPE coating is imaged as shadows at the edges of the tip. It becomes clear that even by this simple preparation procedure, the coating thins out in the direction of the tip, leaving out the topmost part.

4.7.2 STM Set-Up

All STM images shown in this thesis were recorded with a *Veeco Multimode 8* STM/AFM device, including the corresponding *Nanoscope 5* controller, the *Bruker Universal Bipotentiostat*,

and the *Nanoscope Software 8.15*. An *AS-12VLR* scanner was used, which is designed for imaged areas below 4 µm^2. Figure 4.3 shows the set-up of the electrochemical STM cell. The detailed view of the cell shows the WE is mounted on the scanner, and the RE, CE, and STM tip are mounted at the scan head. An inert container, which can be purged with inert gases, is placed around the scanner and cell to prevent exposure to air during the measurement. For minimisation of mechanical vibrations, the STM was placed on an air table.

4.7.3 Measurements

For all STM measurements, a Pt wire served as a CE and an $AlPO_4$-coated Al wire as RE. The electrolyte was added under counter-flow of the used inert gas (N_2, or Ar for Li deposition), and the purging was continued for 5 min. During the *in situ* STM measurement, no purging was possible since this would cause noise. The whole set-up was placed on an air-table for noise-damping. Before every measurement, a CV was recorded to enable a potential conversion to the REs used in other measurements. All measurements were performed using the constant current mode. The detailed parameters, such as tunnelling currents and gains, for every shown image, are listed in the appendix (Tables A.3 and A.4).

4.8 Used Chemicals and Gases

Table 4.2: Au(111) single crystal.

Crystal	Diameter	Height	Manufacturer
Au(111)	12 mm	2 mm	*MaTecK*, Jülich

Table 4.3: Batches of the IL [MPPip][TFSI].

Batch	Purity	Initial Water content / ppm	Manufacturer	Opened
Batch 1	99 %	Unknown	*IoLiTec*, Heilbronn	11.2017
Batch 2	99 %	Unknown	*IoLiTec*, Heilbronn	09.2020
Batch 3	99.9 %	101 ppm	*IoLiTec*, Heilbronn	05.2021
Batch 4	99.9 %	5 ppm	*Solvionic*, Toulouse	06.2021
Batch 5	99.9 %	99 ppm	*IoLiTec*, Heilbronn	08.2022

Table 4.4: Additives for the IL-based electrolytes.

Chemical	Purity	Purpose	Manufacturer
Na[TFSI]	99.5 %	Metal salt for Na deposition	*Solvionic*, Toulouse
Li[TFSI]	99.9 %	Metal salt for Li deposition	*Solvionic*, Toulouse
H[TFSI]	$\geq$95 %	OH^- quenching agent	*Sigma-Aldrich*, Seelze
4 Å molecular sieve	-	Drying agent	*Merck*, Darmstadt

Table 4.5: Gases.

Chemical	Purity	Purpose	Manufacturer
C_4H_{10}	Comm. highest purity	Annealing	*EDCO Eindhoven BV*, Eindhoven
N_2	N 5.0	Inert gas	*MTI IndustrieGase AG*, Neu-Ulm
Ar	N 5.0	Inert gas (Li deposition)	*MTI IndustrieGase AG*, Neu-Ulm

Table 4.6: Metal wires and sheets.

Chemical	Diameter	Purity	Purpose	Manufacturer
Pt wire	0.5 mm	99.99 %	CE	*MaTecK*, Jülich
Al wire	0.5 mm	99.95 %	REs	*MaTecK*, Jülich
Zn wire	1 mm	5N	RE	*MaTecK*, Jülich
Pt/Ir wire (80:20)	0.25 mm	99.99 %	STM tips	*MaTecK*, Jülich
Au sheet	0.1 mm	4N5	WE	*MaTecK*, Jülich
Cu sheet	unknown	unknown	XPS sample holder	unknown
Na rod	–	$\geqslant$99 %	RE	*Merck*, Darmstadt

Table 4.7: Other chemicals.

Chemical	Purity	Purpose	Manufacturer
Acetone	technical	Cleaning	*VWR*, Rosny-sous-Bois
Propan-2-ol	technical	Cleaning	*VWR*, Rosny-sous-Bois
HCl	30 %, surprapure	Cleaning	*Merck*, Darmstadt
H_2O_2	30 %	Cleaning	*Merck*, Darmstadt
H_2SO_4	96 %	Cleaning	*Merck*, Darmstadt
HNO_3	65 %	Cleaning	*Merck*, Darmstadt
NaCN	>97 %	Etching solution	*Sigma-Aldrich*, Seelze
HDPE (*Lupolen 5031 L*)	-	STM tip coating	*LyondellBasell*, Rotterdam
KOH	99.99 %	Al/$AlPO_4$ wires	*Sigma-Aldrich*, Seelze
H_3PO_4	85 wt.-%	Al/$AlPO_4$ wires	*Sigma-Aldrich*, Seelze
$Zn[TFSI]_2$	66.5 %	Zn reference	*Solvionic*, Toulouse
Ferrocene	>98 %	Reference	*Fluku Chemie AG*, Buchs

5 Electrochemical Behaviour of Au(111) in [MPPip][TFSI]

Some parts of this chapter have previously been published in the articles "Reproducibility of electrochemical measurements with ionic liquids: Is the water content the decisive parameter?" and "Assessing the Quality of Ionic Liquids Using Single Crystal Electrochemistry, Surface Science and Data Screening".[60,202]

Understanding the electrochemical behaviour of a specific electrode in ILs is challenging because it not only varies in dependence on the used IL, but also using different batches from the same IL purchased from the same company. In this chapter, first, the IL [MPPip][TFSI] is classified in different batches of the same electrochemical behaviour. Then, the influence of H_2O and O_2 on the observed behaviour will be discussed.

5.1 Classification of [MPPip][TFSI] in Two Types of Electrochemical Behaviour

It is well-known that electrochemical measurements using the same IL can lead to different results depending on the date the batch of IL was purchased or the supplier.[37] During my thesis, I used five different batches of the IL [MPPip][TFSI] from two suppliers. Details about these different batches are given in the experimental chapter 4. Figure 5.1 shows the first and fifth CV for Au(111) recorded in each batch with a lower potential limit (LPL) of −1.5 V and an upper potential limit (UPL) of 1.7 V. Comparing the CVs, two aspects can be highlighted: i) The CVs of batch 1 are very similar to the CVs of batch 3. Therefore, these batches can be categorised as batches of 'type I'. Similarly, the CVs of batch 2 are similar to the CVs of batches 4 and 5. Thus, those batches can be categorised as batches of 'type II'. ii) There are

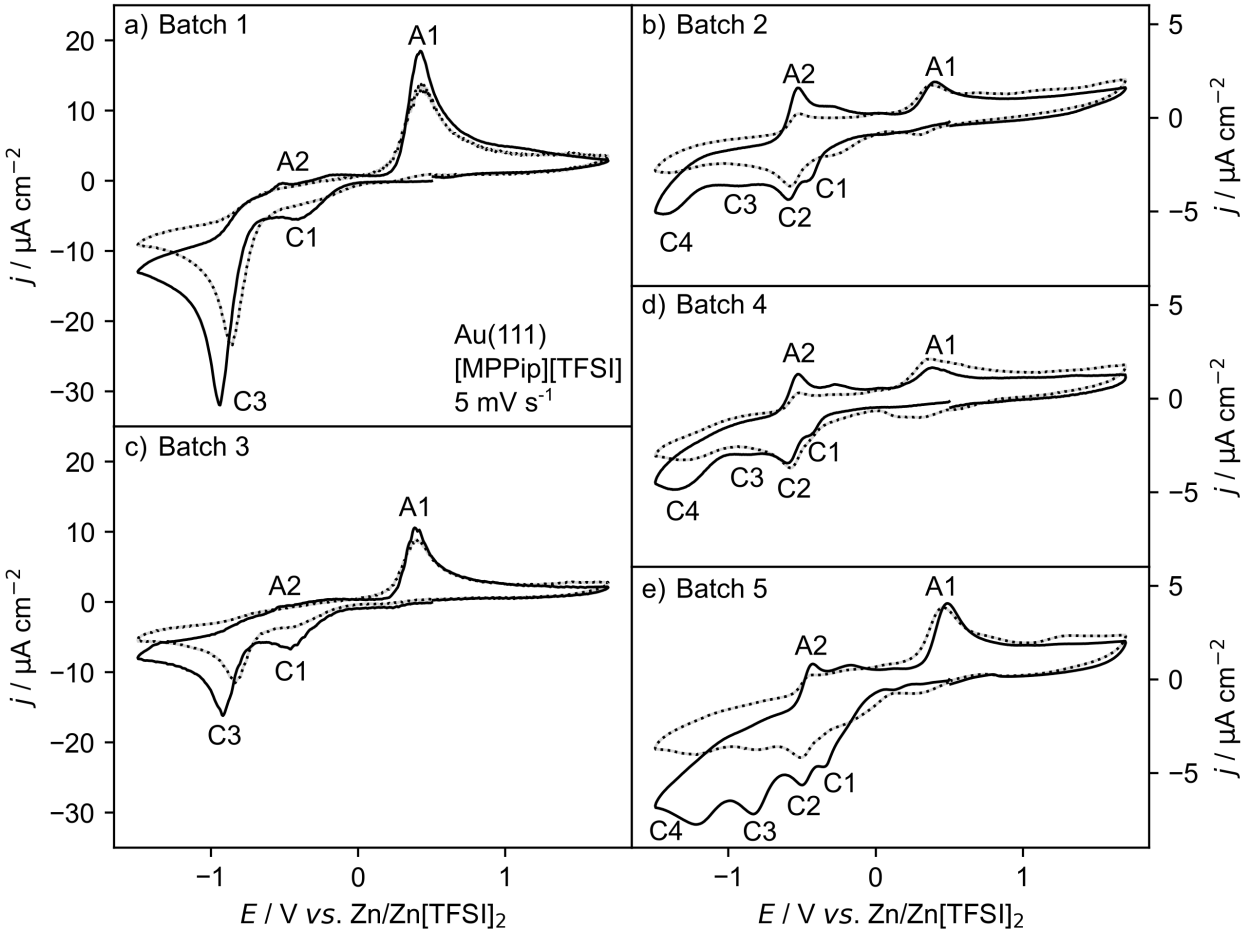

Figure 5.1: CVs for Au(111) in the five different batches of the IL [MPPip][TFSI] used during the last years. Each cycle was recorded starting at 0.5 V with a LPL of –1.5 V, an UPL of 1.7 V, and a scan rate of –5 mV s^{-1}. The 1st and 5th cycles are shown with solid and dotted curves, respectively.

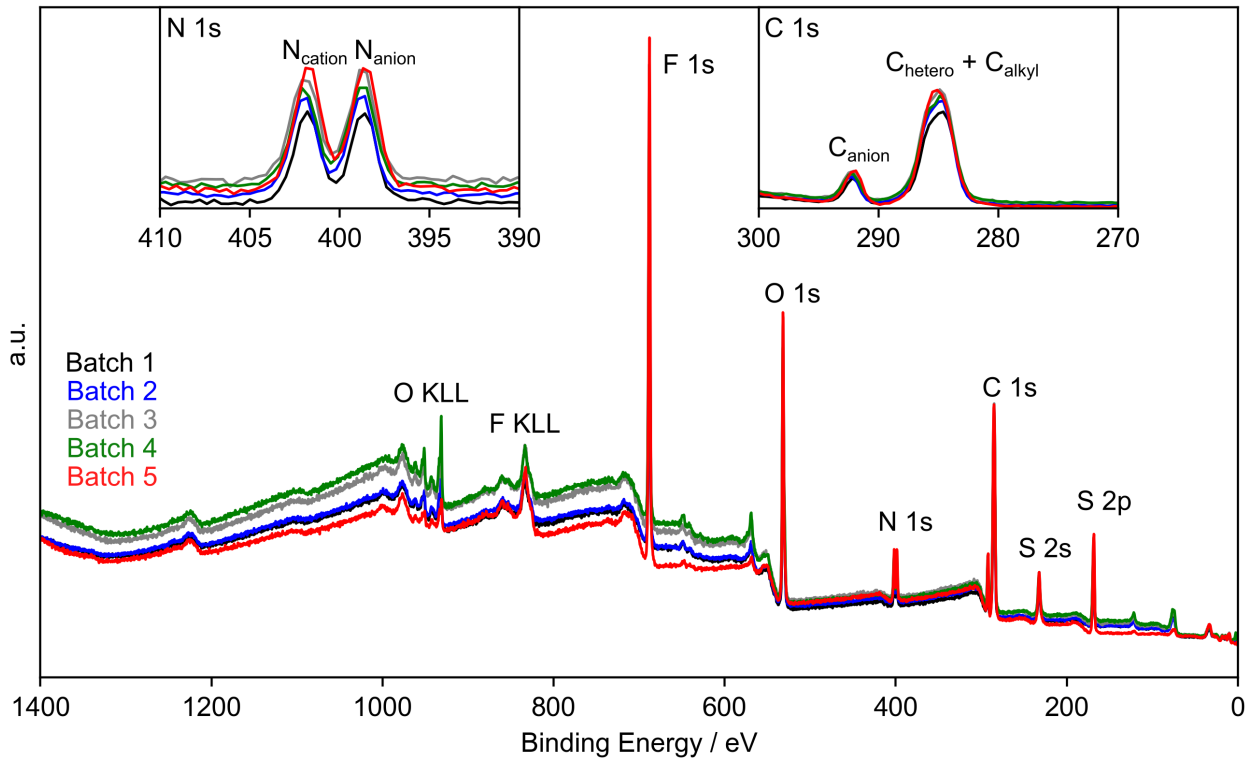

Figure 5.2: XP spectra of the five different batches of the IL [MPPip][TFSI] used during the last years. Batches 1 and 2 were vacuum-dried; the other batches were used as-received. The insets show detailed views of the N 1*s* and C 1*s* regions. The peaks align with the XP spectra of the constitutional isomer [BMPyr][TFSI].[203]

huge differences between the two observed behaviours. The overall current densities of the CVs for type II are significantly lower than those for type I. In the same way, the current density in the peaks C1 (–0.45 V), C3 (–0.9 V), and A1 (0.4 V), which are the dominating features of type I, is much lower for type II. The peaks C2 (–0.6 V), C4 –1.4 V and A2 (–0.5 V), which are not significant for type I, are predominant in the CVs of type II.

The two distinct types of electrochemical behaviour can lead to the assumption that the type of behaviour is determined by the presence or absence of only one impurity. Often, ILs are contaminated by metal halides, which originate from the synthesis.[45] Therefore, we performed XPS for a quick check on impurities. Figure 5.2 shows the XP spectra of all investigated batches of the IL, including a magnification of the C 1*s* and N 1*s* regions. All spectra are rather similar. The observed peaks align with the peaks of the constitutional isomer [BMPyr][TFSI].[203] Therefore, high concentrations of metal impurities can be excluded.

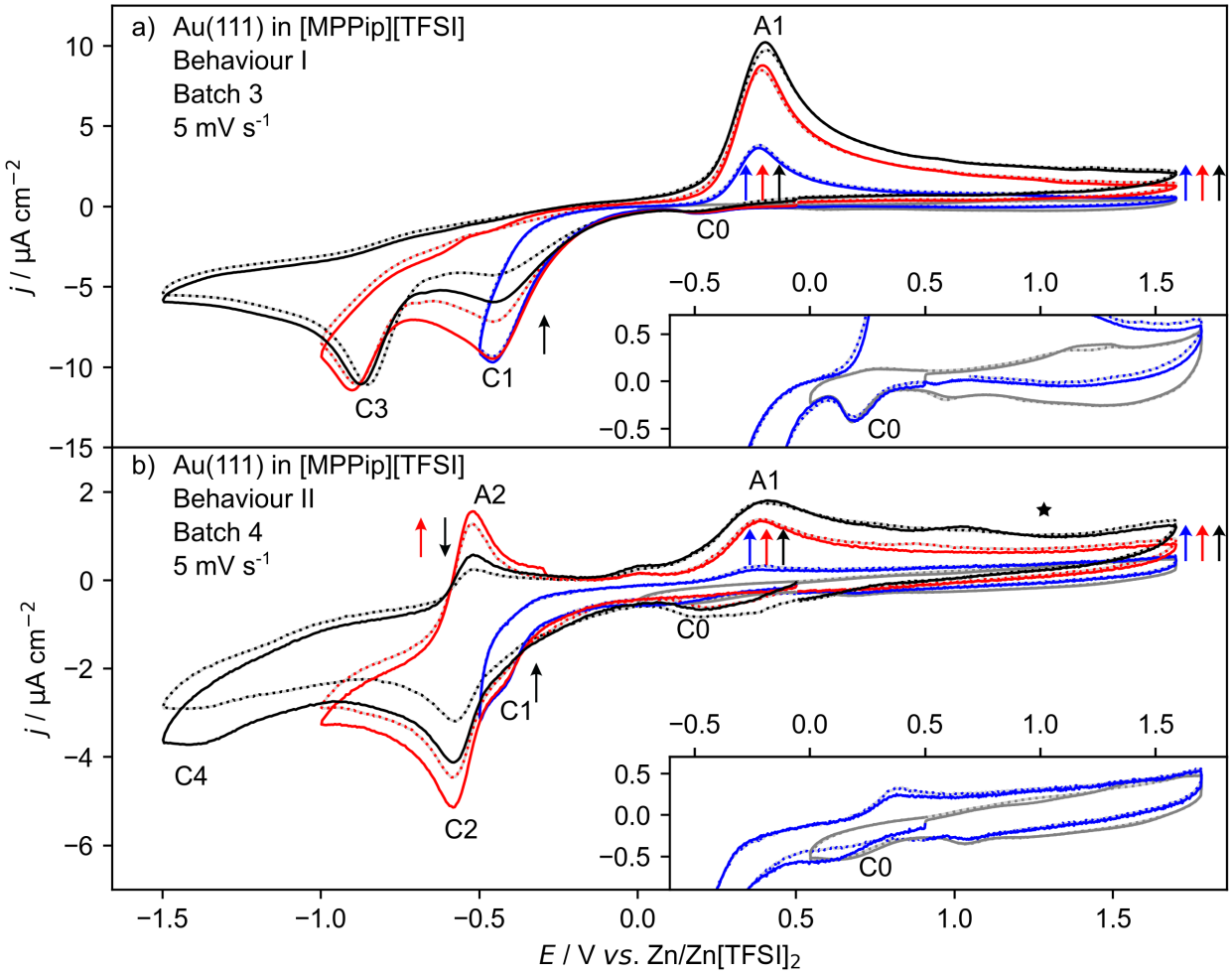

Figure 5.3: CVs for Au(111) in a) batch 3 and b) batch 4 of the IL [MPPip][TFSI]. Each cycle was recorded starting at 0.5 V and a scan rate of –5 mV s^{-1}. The LPL was gradually decreased from 0.0 V to –1.5 V while the UPL was constant at 1.7 V. For each LPL, two cycles were recorded; the 1st is shown with solid lines, and the 2nd with dotted lines. The insets magnify the low current density region of the CVs with LPLs of 0.0 V and –0.5 V.

Next, the LPL of the CVs was stepwise decreased from 0.0 V to −1.5 V while the UPL was kept constant at 1.7 V to determine the correlation between the different peaks. In Figure 5.3, the resulting CVs for batch 3 and batch 4 representing type I and II, respectively, are shown. The grey curves show the CV with the highest LPL of 0.0 V. The CVs are rather featureless compared to those recorded with a lower LPL. The prominent peak A1 is not observed to any extent. In the negative-going scan, a small cathodic peak C0 appears at ca. 0.2 V for both investigated batches. This peak is also present in all following cycles but is barely visible due to its small current density.

Decreasing the LPL to −0.5 V, the peak C1 at ca. −0.45 V appears followed by the anodic peak A1 at ca. 0.4 V. For batch 3 (type I), C1 and A1 have a maximum current density of ca. $-10\,\mu A\,cm^{-2}$ and $4\,\mu A\,cm^{-2}$, respectively. In contrast, the peaks C1 and A1 show as low current density with a maximum of ca. $-3\,\mu A\,cm^{-2}$ and $0.25\,\mu A\,cm^{-2}$ for batch 4. It seems that the current density in the peak C1 is not only related to the peak C1 but also the rising peak C2 with a peak maximum at ca. −0.6 V.

Decreasing the LPL to −1.0 V, the differences between the two types of electrochemical behaviour became even more apparent. For batch 3 (type I), the current density decreases negative of the peak C1. At even more negative potentials, the peak C3 with a peak maximum at ca. −0.9 V causes another increase of the current density to a maximum of ca. $-11\,\mu A\,cm^{-2}$. Consequently, in the positive-going scan, the peak A1 reaches a maximum current density of $9\,\mu A\,cm^{-2}$. Additionally, the current density positive of this peak increased as well. The current density is also higher in the following negative-going scan in the range from the UPL to the initial potential of 0.5 V. For batch 4 (type II), the peak C1 is followed by the peak C2 with a peak maximum at ca. −0.6 V and a maximum current density of ca. $-5\,\mu A\,cm^{-2}$. In the positive-going scan, this peak is followed by the peak A2 at a peak maximum of ca. −0.5 V and a maximum current density of ca. $1.5\,\mu A\,cm^{-2}$. The peak A1 increases to a maximum current density of ca. $1.3\,\mu A\,cm^{-2}$ and similarly to type I, the current density increases at potentials positive of the peak A1 in the positive-going scan and the negative-going scan between the UPL and the initial potential. Another effect observed for both behaviours is that in the second potential cycle, the maximum current density decreases in the peak C1 in type I, respectively, and the peaks C1, C2, and A2 for type II.

Decreasing the LPL to −1.5 V only has a minor impact on batch 3 (type I). At potentials negative of the peak C3, the current density does not become zero but remains at ca. $-5\,\mu A\,cm^{-2}$. Due to this additional negative charge, the peak A1 has a higher current density. The current

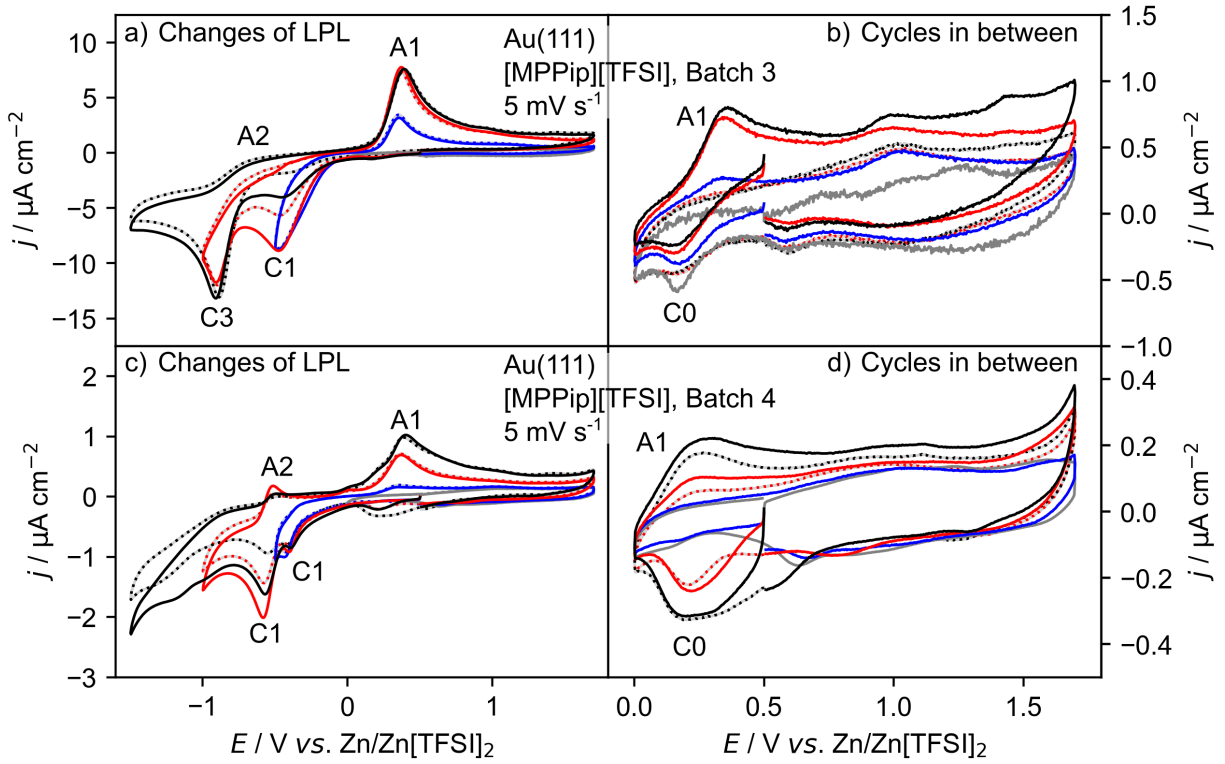

Figure 5.4: CVs for Au(111) in a) and b) batch 3 and c) and d) batch 4 of the IL [MPPip][TFSI]. Each cycle was recorded starting at 0.5 V and a scan rate of –5 mV s^{-1}. a) and c) The LPL was stepwise decreased from 0.0 V to –1.5 V while the UPL was constant at 1.7 V. For each LPL, two cycles were recorded; the 1st is shown with solid lines, and the 2nd with dotted lines. After each decrease of the LPL, additional cycles with an LPL of 0.0 V were recorded, which are shown in b) and d). Here, the solid and dotted curves show the 1st and 5th cycle.

density at potentials positive of this peak is also higher than in the CVs with higher LPLs. For batch 4 (type II), the changes by this decrease of the LPL are more significant. First, the additional peak C4 at ca. –1.4 V appears. Consequently, the peak A2 decreases even more than in the previous cycle. In contrast, the maximum current density of the peak A1 increases and an additional small hump at potentials positive of A1 appears. As for type I, the current density at potentials positive of the peak A1 shifts to more positive values.

Another experiment determined whether the CV changes by lowering the LPL were reversible or irreversible. Therefore, after recording 2 cycles at each LPL, the LPL was again set to 0.0 V. The resulting CVs with the varied LPL for batch 3 and 4 are shown in Figure 5.4 a and c and

the respective cycles with an LPL of 0.0 V in Figure 5.4 b and d. The CVs with an LPL of 0.0 V changed upon lowering the LPL in the previous cycle for both batches. The peak A1 emerges, and the current density close to the UPL increases compared to the cycles before lowering the LPL. For the batch 4, additionally, the peak C0 emerges. By repetitive cycling with an LPL of 0.0 V after cycles with a lower LPL, the CVs recorded in batch 3 take the shape of the CV before lowering the LPL. In contrast, the CVs with an LPL of 0.0 V recorded in batch 4 after the LPL was decreased are barely influenced by cycling. The peak C0 remains and the overall current density is much higher than in the initial cycle.

A comparison of the suppliers and the stated purity (Table 4.3) shows that neither the supplier nor the purity is the parameter which determines if a specific batch is type I or type II. The batches 1 to 3, and 5 are subsequently purchased from the same supplier and show alternating behaviour of type I and II. This leads to the assumption that a difference in the synthesis does not induce the observed behaviours. It is more likely that the concentration of one impurity varies from batch to batch. From the shown CVs, it is hard to estimate if the higher concentration of this impurity is present in batches of type I or II since there are two different ways an impurity could influence the electrode surface and thus the features of the CV. i) The impurity is reduced in the peaks C1 and C3 or its presence catalyses the reduction processes during these peaks. The species formed during this reaction are then oxidised in the peak A1. Thus, a higher impurity concentration is present in batches of type I. Due to the lower concentration of the impurity in type II, the peaks C1, C3, and A1 have a lower current density, and the surface is not blocked for the processes which occur during the peaks C2, C4, and A2. ii) Another explanation could be that in batches of type II, the concentration of an impurity is increased. This impurity (partially) blocks the surface for the reactions of the peaks C1 and C3. Consequently, the peak A1 decreased significantly. The peaks C2, C4, and A2 could be explained by electrochemical reactions of the impurity itself or by reactions catalysed by it.

5.2 Influence of H_2O and O_2

5.2.1 Drying Methods

Since H_2O is a very common impurity in ILs and quite reactive, it is state-of-the-art to dry ILs before their use. Common drying steps are the application of heat and vacuum[44,190–192] or the addition of molecular sieves.[81,184,204] In this thesis, the IL was either used without any pre-treatment or after applying heat and vacuum. The heat and vacuum drying was only applied if residual water had to be diminished, namely for alkali metal deposition and the investigation of cathodic corrosion at minimised water contents. The molecular sieve was only used for comparison in the measurements described in the following. Details are included in the experimental section in Chapter 4. It should be clarified which influence the applied procedures have on the electrochemical behaviour of the IL. Especially, introducing new impurities in the electrolyte during drying must be avoided. The quantitative effect of the drying procedures on the H_2O content was evaluated by Karl-Fischer titration. Typical H_2O contents of the as-received IL depend on the supplier and are 5 to 100 ppm. After drying at 80 °C and 1×10^{-3} mbar, the H_2O content varied between 50 ppm and 15 to 20 ppm. This value depended on the container in which the IL was dried. Hereby, Schlenck-tubes yielded a lower H_2O content than vials. Adding a molecular sieve before applying heat and vacuum, the H_2O content was typically below 5 ppm. After determining the water content, CVs recorded in the differently dried IL were compared to those recorded in the as-received IL. *Elkhafif et al.* also used cyclic voltammetry for comparing the IL's quality after drying with heat and vacuum, respectively, with molecular sieves. However, they only recorded CVs for the full electrochemical stability window, whereas in this thesis a stepwise decrease of the LPL will be discussed.

Figure 5.5 shows the effect of the different drying methods on the features observed in the CVs for batch 3 (type I). In each measurement, the LPL was gradually decreased, as described in the previous section for Figure 5.3, to see which influence the different purification methods had on the evolution of the peaks in dependence on the LPL. The dotted curves in each figure show the respective measurements for the untreated IL. Figure 5.5 a shows a comparison of the heat and vacuum-dried IL (solid curves) with the untreated IL (dotted curves). The maximum current density of the peak C1 has decreased after the drying procedure. Consequently, the maximum current density of the peak A1 also decreased. This could be expected since the previously described experiment has shown that the peak A1 is correlated with the

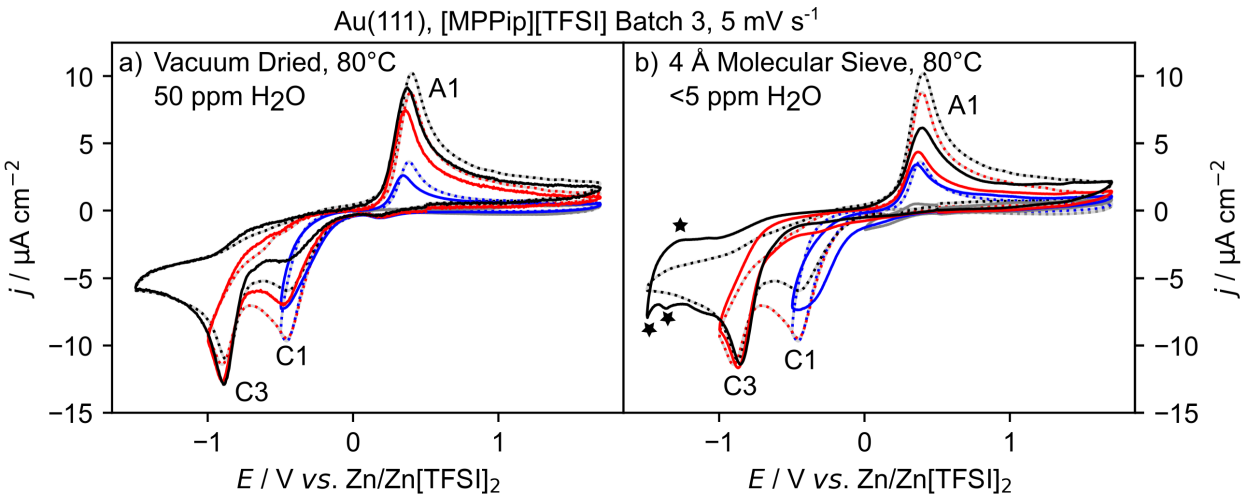

Figure 5.5: CVs for Au(111) in batch 3 of the IL [MPPip][TFSI] with the same measurement procedure as for Figure 5.3. The a) vacuum-dried and b) molecular sieve-dried (solid) is compared to the as-received (dotted) IL. For each LPL, the 1st cycle is shown.

peak C1. Interestingly, the maximum current density of the peak C3 slightly increased compared to the measurement with the untreated IL. Nevertheless, these changes are small and typical variations between different measurement days. Note that the changes shown here are not necessarily due to the change in the H_2O content. Applying heat and vacuum can reduce all volatile species, including gases dissolved in the IL, e.g. O_2 or CO_2.

In the next step, the influence of the molecular sieve on the electrochemical behaviour of the IL was tested. Here, 4 Å molecular sieve was added, and then the IL was again dried at heat and vacuum. Again, the electrochemical behaviour was compared to the untreated IL by cyclic voltammetry, and the LPL was gradually lowered. The resulting CVs are shown in Figure 5.5 b with the solid curves for the IL with molecular sieve and the dotted curves for the untreated IL.

The maximum current density of the peaks C1 and A1 decreased compared to the untreated IL which is similar to the treatment with heat and vacuum. Note that with the molecular sieve added, more potential cycles with an LPL of −0.5 V were performed as in the reference measurement with the untreated IL. This is why the peak C1 only appears in the blue curve. It is expected that the peak would still be present in the red and black curve if fewer cycles with an LPL of −0.5 V would have been made. An even more significant change can be seen in the black curve recorded with an LPL of −1.5 V. Negative of −1.2 V three features appear, which are marked with stars in Figure 5.5. First, a small cathodic peak appears at ca. −1.3 V.

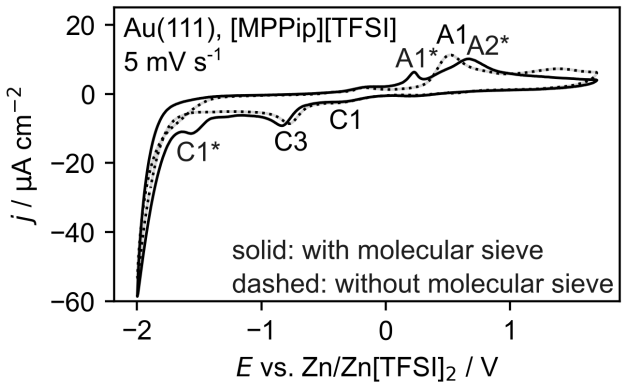

Figure 5.6: CVs for Au(111) recorded in batch 3 of the IL [MPPip][TFSI] with a LPL of –2.0 V. The solid and dotted curves show the molecular sieve-dried and as-received IL, respectively.

Second, the negative current density increases from –1.4 V until the LPL, while it decreases for the measurement with the untreated IL. Third, in the following positive-going scan, the current density increases at less positive potentials as in the measurement with the untreated IL, including a small hump at ca. –1.3 V.

Figure 5.6 shows an additional CV with an LPL of –2.0 V. The molecular sieve-dried IL (solid) is compared with the as-received IL (dotted). It becomes clear that the increase in negative current density around the LPL of –1.5 V turns into a peak C1* with a maximum current density of ca. –1.6 V, which is not present in the as-received IL. At ca. –1.7 V the current density declines exponentially. This exponential decrease could indicate the negative stability limit of the IL on Au(111). In the following positive-going scan, the features have changed significantly compared with the previous potential cycles. There is a peak A1* at 0.3 V and a peak A2* at 0.7 V, while the peak A1 has vanished. In the untreated IL, no such changes compared to the previous positive going scans (see Figure 5.3 were observed. Only the current density at potentials positive of the peak A1 is increased, as it was observed for every extension of the LPL. This indicates that the peaks C1*, A1*, and A2* are mainly induced by some changes in the IL by the molecular sieve.

Figure 5.7 a and b show the CVs of the molecular sieve dried batches 4 and 5 of the IL [MPPip][TFSI]. These batches both show electrochemical behaviour of type II, and the measurement procedure was the same as for the previous experiments, gradually lowering the LPL from 0.0 V to –1.5 V. For batch 4, a CV with an additional LPL of –2.0 V was recorded. In comparison, the dashed curves show the measurements of the as-received IL. Overall, the

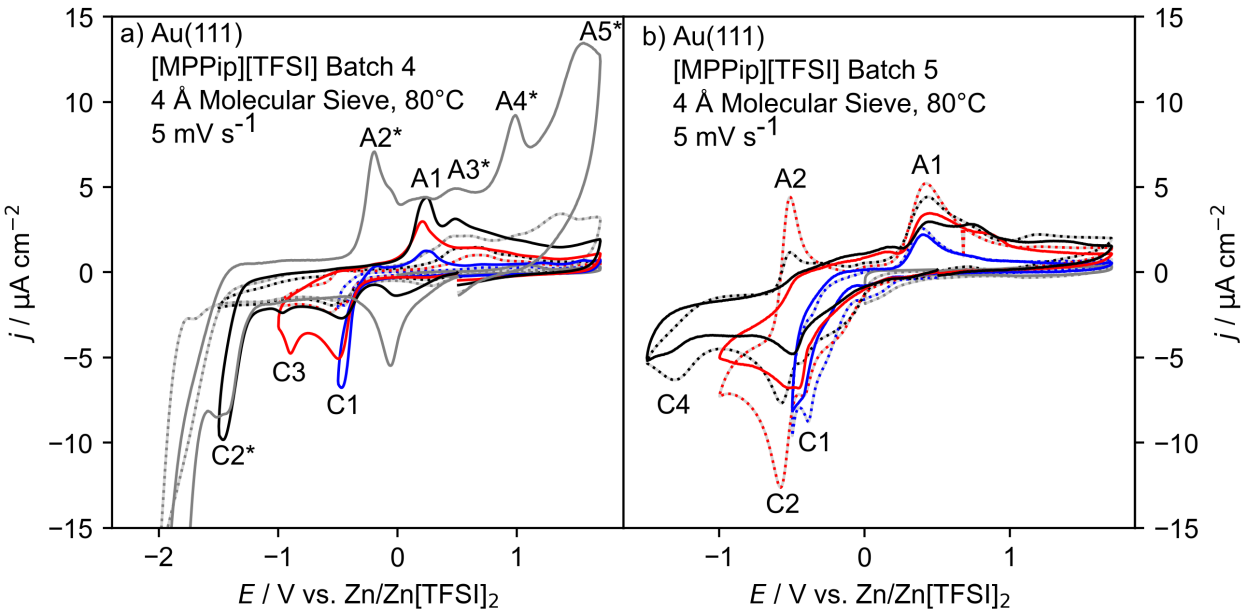

Figure 5.7: CVs for Au(111) recorded in a) batch 4 and b) batch 5 of the IL [MPPip][TFSI] with the same measurement procedure as for Figure 5.3. The molecular sieve-dried (solid) is compared to the as-received (dotted) IL. For each LPL, the 1st cycle is shown.

electrochemical behaviour after adding a molecular sieve to an IL of type II was very variable: A huge variety of peaks appeared in different measurements. Nevertheless, there are some clear trends observable in all measurements. First, the peaks C2 and A2 vanish after the addition of a molecular sieve. We assume that they are induced by an impurity which can be bound to the molecular sieve. Second, after reducing the LPL to –2.0 V, peaks appear which are not present in the untreated IL. These peaks resemble the ones for the molecular sieve-treated IL of batch 3 (type I) which are marked with stars in Figure 5.5.

We assume that there are two possible explanations for these additional peaks. One possibility could be that the molecular sieve has removed a species which blocked the surface. Therefore, the peaks C1*, A1* and A2* only appear after adding a molecular sieve to the IL. A possible process could be the ordered adsorption of the IL on the surface.[61,81] Another explanation could be that some species from the molecular sieve remain in the electrolyte after the treatment. There are several indications that this species is cationic Na, which changed places with the cations of the IL: i) The peaks observed are quite similar to the ones that were discovered for the same IL with Na[TFSI] added to investigate the Na deposition.[205] The details about the Na deposition will be discussed in chapter 7. ii) *Ntais et al.* have shown that such ion exchanges are possible.[206] They used x-ray diffraction and Fourier transform Raman spectroscopy to prove the presence of Na[TFSI] in a zeolite-IL composite material.[206]

To verify the presence of Na in the IL after the pre-treatment, XP spectra, shown in Figure 5.8, were recorded. At first, spectra of the as-received IL and the molecular sieve-dried IL were recorded. They are shown in black and blue, respectively. The overview spectra look very similar. Nevertheless, the spectrum of the molecular sieve-dried IL shows a small Si 2*p* peak. In addition, the detail spectra show that there is a significant Na 1*s* peak. There are no significant peaks of Na or Si in the detailed spectra of the untreated IL. To verify that Na can be deposited from the molecular sieve-treated IL, a polycrystalline Au sheet was polarised in it at –1.8 V for 2 h. At this potential, a significant Na deposition is expected (see Chapter 7). Afterwards, the IL was removed by rinsing with acetone and an XP spectrum of the Au sheet, was recorded, shown in the red curve in Figure 5.8. The overview spectrum shows a clear Na 1*s* peak. Hence, it is clear that Na is present in the molecular sieve-treated IL.

In summary, both drying methods lead to changes in the CVs to some extent. However, they only yield a slight decrease of the peaks C1 and A1. Additionally, the molecular sieve introduces Na ions and silicate as additional impurities.

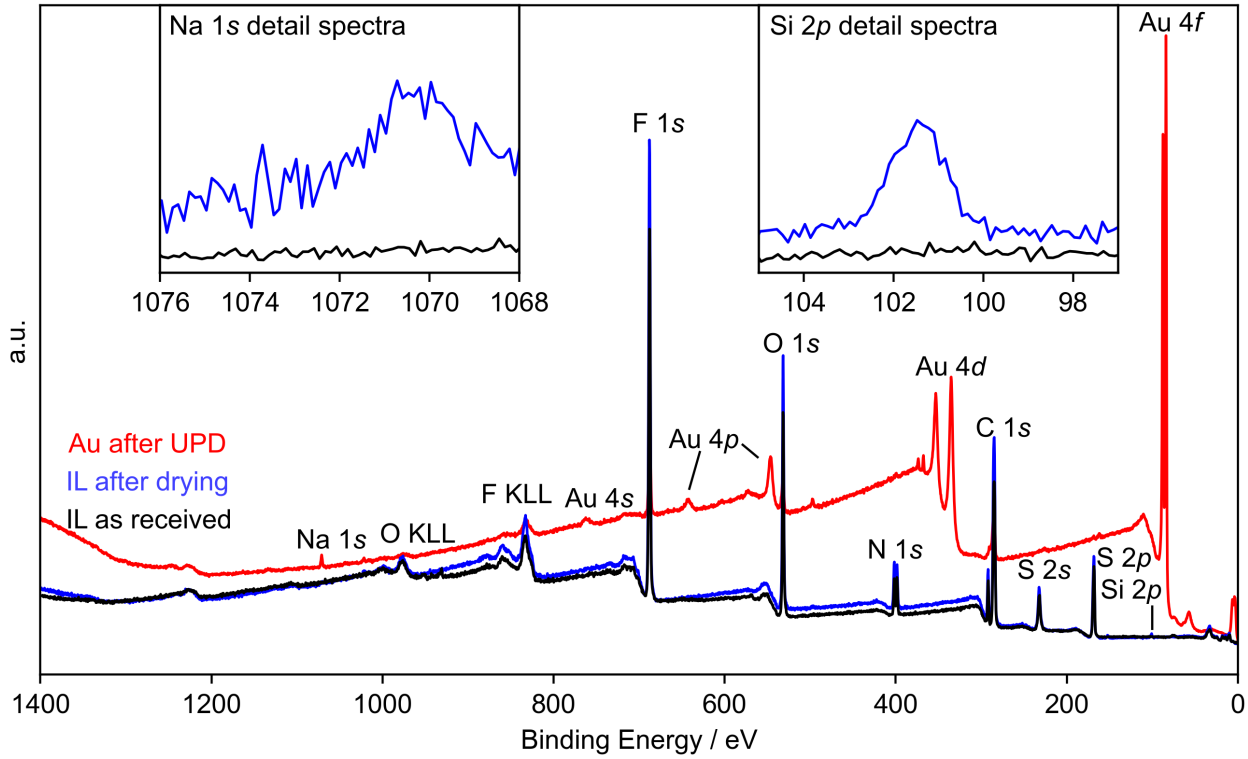

Figure 5.8: XP spectra of the molecular sieve-dried and as-received batch 5 of the IL [MPPip][TFSI] and a polycrystalline Au surface after Na UPD from the molecular-sieve dried IL with polarisation at −1.8 V for 2 h. The insets show detailed spectra of the IL in the Na 1*s* and the Si 2*p* region.

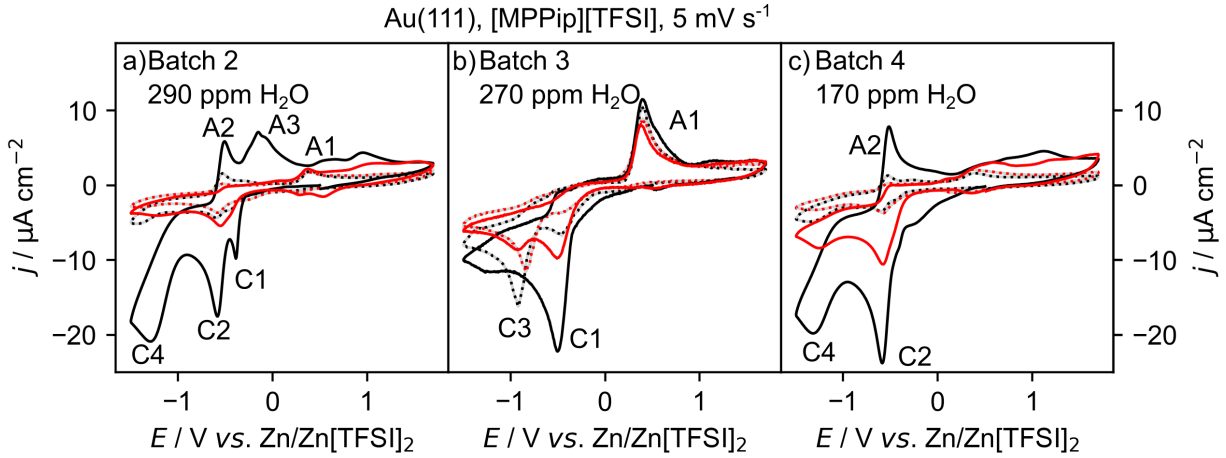

Figure 5.9: CVs for Au(111) recorded in a) batch 2, b) batch 3, and c) batch 4 of the IL [MPPip][TFSI] with ca. 150 ppm H_2O added. Each cycle was recorded starting at 0.5 V with a LPL of –1.5 V, an UPL of 1.7 V, and a scan rate of –5 mV s^{-1}. The 1st and 5th cycles are shown in black and red curves, respectively. The dotted curves show the respective CVs of the IL without added H_2O.

5.2.2 Influence of Adding H_2O and O_2

In order to investigate the influence of additional H_2O, small amounts of H_2O were added to the IL. For the batches 2, 3, and 4, Figure 5.9 shows CVs for the IL to which ca. 150 ppm H_2O was added. Compared to the CVs of the pure IL, for all batches an overall increase of the current density is measured in the negative-going scan starting at ca. 0.0 V. In the case of batch 3 (type I), only the peak C1 increased significantly. In contrast, the peak C3 decreased after adding H_2O to the electrolyte, and the peak A1 did not change significantly. For the batches 2 and 3, which showed electrochemical behaviour of type II, the peaks C2, C4, and A2 increased by adding H_2O. Additionally, in batch 2, the peak C1 increased and a new anodic peak at ca. –0.15 V appeared. Both batches of type II showed additional small peaks in the positive-going scan, which were not observed previously.

Figure 5.10 shows a series of CVs for Au(111) recorded in [MPPip][TFSI] of batch 3 with a H_2O content of ca. 450 ppm 12 h, 2 days, and 5 days after the H_2O addition to the IL. In comparison, the dotted curves show the IL without added H_2O and a H_2O content of ca. 75 ppm. 12 h after the H_2O addition, the CV is comparable to the CV with 270 ppm H_2O. Interestingly, the peak C1 increased by the H_2O addition covers less charge as in the measurement with a H_2O content of 270 ppm. Note that the measurement with 270ppm H_2O was performed directly after the

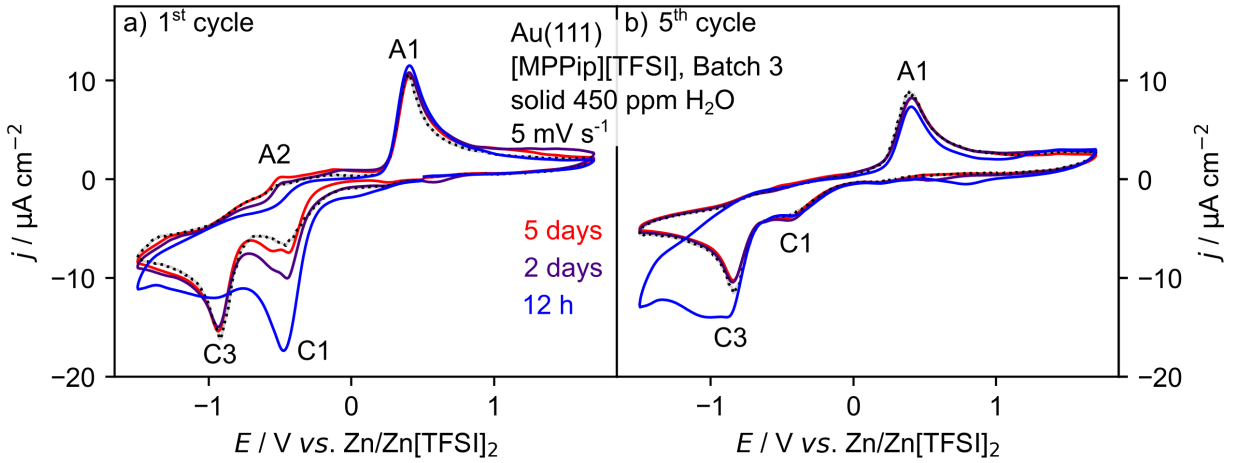

Figure 5.10: CVs for Au(111) recorded in batch 3 of the IL [MPPip][TFSI] with a H_2O content of 450 ppm 12 h (blue), 2 days (purple), and 5 days after the H_2O addition in comparison to the IL without added H_2O (dotted). Each cycle was recorded starting at 0.5 V with a LPL of –1.5 V, an UPL of 1.7 V, and a scan rate of $-5\,mV\,s^{-1}$. The 1st cycles are shown in a) and 5th cycles in b).

H_2O addition. The height of the peak C1 seems not necessarily dependent on the H_2O content but rather on the time between the H_2O addition and the electrochemical measurement. This trend continues with the next CVs measured after two and five days. After two days, only the first cycle shows a significant deviation of the current density maximum of the peak C1. All other peaks are the same as in the CV with the IL without added H_2O. After five days only very few changes have remained. Two small features are visible, which resemble the peaks C2 and A2 of the ILs of type II. Nevertheless, these peaks sometimes occur in ILs of type I as well, but with a much lower intensity.

It could be assumed that the peak C1 in type I and the peaks C1, C2, and C4 in type II are related to electrochemical reactions of H_2O. In this case, the water content decreased to its initial value within five days since the CVs for the IL with 450 ppm H_2O take the shape of the pure IL after this period. However, Karl Fischer titration revealed that the water content was constant. Therefore, the change of the peak C1 was not induced by the increase of the H_2O content in the IL but by adding another species along with the H_2O whose concentration is unknown. This species must be much more volatile than H_2O or reacting with the IL, explaining the substantial decrease in concentration when the H_2O concentration did not change. The most apparent compound is O_2, which was present in the air during the H_2O addition. Furthermore, the H_2O was air-saturated since it was not diaerated with an inert gas such as N_2

before the addition to the IL. Ionic impurities of the used H_2O, such as metal cations, can be excluded since its quality was constantly monitored. Furthermore, the concentration of such impurities would not decrease with time.

Different reaction mechanisms are suggested for the O_2 reduction reaction (ORR).[113,116,207–209] The most simple possibilities are a one-electron process forming a superoxide radical anion ${O_2}^{-*}$ (5.1) or a two-electron process forming a peroxide ion ${O_2}^{2-}$ (5.2). Both these reactions only involve only O_2.[116,207,208]

$$\mathrm{O_2} + \mathrm{e^-} \longrightarrow {\mathrm{O_2}}^{-*} \tag{5.1}$$

$${\mathrm{O_2}}^{-*} + \mathrm{e^-} \longrightarrow {\mathrm{O_2}}^{2-} \tag{5.2}$$

Especially in the presence of H_2O, alternative reaction mechanisms occur in which H_2O is involved as well.[113,207–209] These mechanisms are essential since superoxide is very reactive and reacts with H_2O if present. The possible reactions are a two-electron transfer forming hydrogen peroxide and hydroxide (5.3), a four-electron transfer forming hydroxide ions (5.4) and a one-electron transfer forming a peroxide radical and hydroxide ion (5.5,5.6).[113,208]

$$\mathrm{O_2} + 2\,\mathrm{H_2O} + 2\,\mathrm{e^-} \longrightarrow \mathrm{H_2O_2} + 2\,\mathrm{OH^-} \tag{5.3}$$

$$\mathrm{O_2} + 2\,\mathrm{H_2O} + 4\,\mathrm{e^-} \longrightarrow 4\,\mathrm{OH^-} \tag{5.4}$$

$$\mathrm{O_2} + \mathrm{H_2O} + \mathrm{e^-} \longrightarrow {\mathrm{HO_2}}^{*} + \mathrm{OH^-} \tag{5.5}$$

$$2\,{\mathrm{HO_2}}^{*} \longrightarrow \mathrm{O_2} + \mathrm{H_2O_2} \tag{5.6}$$

As discussed above, these reaction mechanisms are more realistic than the mechanisms without involved H_2O since measurements without any H_2O in the IL are impossible under the applied conditions.[184] Since the peak A1 only appears in the positive-going scan when the LPL was extended into or beyond peak C1 in the previous negative-going scan, the process inducing the peak A1 seems to be related to the species formed during these reactions; either OH^- or H_2O_2.

In order to determine which of these species is involved in the process inducing the peak A1, H[TFSI] was added to the IL. The added protons can react in two ways: They recombine with OH^- to H_2O or enable another mechanism for the ORR in which H_2O_2 is formed (5.7)[207,209].

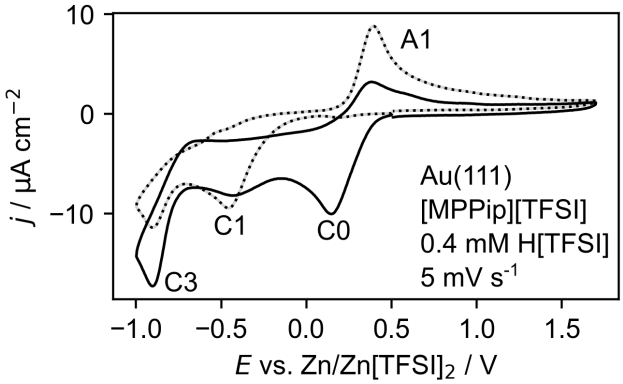

Figure 5.11: CVs for Au(111) recorded in batch 3 of the IL [MPPip][TFSI] with 0.4 mM H[TFSI] (solid) in comparison to the pure IL (dotted). The cycles were recorded starting at 0.5 V with a LPL of –1.0 V, an UPL of 1.7 V, and a scan rate of –5 mV s^{-1}.

$$O_2 + 2\,H^+ + 2\,e^- \longrightarrow H_2O_2 \tag{5.7}$$

Therefore, it can be assumed that the peak A1 should decrease if OH^- is involved in the process inducing it, respectively, increase if H_2O_2 is involved in the process.

Figure 5.11 shows a CV for batch 3 of the IL [MPPip][TFSI] with 0.4 mM H[TFSI] in comparison to the same CV of the IL without H[TFSI]. The addition of H[TFSI] leads to a significant increase of the peak C0. So far, the origin of this peak is unclear. Additionally, the peak C3 is increased, and the peak A1 is decreased. In measurements with a higher concentration of H[TFSI], the peak C0 becomes the predominant feature, and the peak A1 completely disappears. This leads to the assumption that the peak A1 is related to the adsorption and subsequent oxidation of OH^-.

It seems contradictory that the peak C1 in ILs of type I decreases with every cycle while the peak A1 remains constant. This can be explained if the ORR is not the only reaction where OH^- is formed. The window opening experiment (Figure 5.3) showed that the peak C3 also contributes to the current density in the peak A1. Therefore, it is likely that this peak is related to the H_2O reduction reaction(5.8).[196,210]

$$2\,H_2O + 2\,e^- \longrightarrow H_2 + 2\,OH^- \tag{5.8}$$

The assumption that the peaks C3 and A1 are related to the H_2O reduction and oxidation

is supported by the potential difference of ca. 1.3 V between the peak potentials since it is well-known that the electrochemical stability window of H_2O is 1.23 V.[211]

For type II, the peak assignment is more complicated since more peaks are present. It seems that all peaks from type I are also there, but additional features can also be observed. The peaks C2 and A2 are increased after the H_2O and O_2 addition and vanish completely after the addition of the molecular sieve. It seems they are related to another ORR mechanism, which only happens in the presence of a specific catalytic impurity that the molecular sieve can remove. The small peak separation between the peaks C2 and A2 hints to a stabilisation of ${O_2}^{-*}$ which is formed in the peak C2 (5.1) and reoxidised in the peak A2(5.9). *Randström et al.* reported such a mechanism in the absence of H_2O at a similar peak potential.[116]

$$ {O_2}^{-*} \longrightarrow O_2 + e^- \tag{5.9} $$

In summary, it seems that all observed peaks of the CVs for Au(111) recorded in the IL [MPPip][TFSI] are not induced by the IL itself but by impurities present, such as H_2O and O_2. The influences of the electrocatalytic reactions of these impurities on the morphology of the Au(111) surface will be investigated in the next chapter.

6 Morphological Stability of Au(111) in [MPPip][TFSI]

This chapter describes the stability of the Au(111) electrode in [MPPip][TFSI]. Primarily, *in situ* STM measurements were performed to investigate the surface morphology at different potentials and structural changes were related to features observed in the CV. First, the Au surface oxidation and reduction have been imaged. A particular focus was set on the initial stages of cathodic corrosion of the Au(111) surface and the influence of the H_2O content in the IL on it. Second, the formation and lifting of the reconstruction were analysed. In the last section, other morphological changes which occur in the presence of O_2 were analysed. All measurements shown in this chapter were performed with batches of [MPPip][TFSI], which showed type I of electrochemical behaviour.

6.1 Oxidation and Reduction of Au(111)

For electrolytes, electrochemical potential stability windows (or short electrochemical windows, EWs) are often given to refer to the stability of an electrolyte towards electrochemical oxidation and reduction. The potential difference between the reduction and the oxidation potential is then called EW.[212]. The knowledge about these limits is particularly important for supporting electrolytes, which should not participate in electrochemical reactions. For example, the here investigated IL [MPPip][TFSI] was designed with a huge EW to support Li deposition and dissolution. Even if EWs are often given as specific values referred to an electrolyte, they also depend on the type of electrode used.[74,213] For example, the here used IL has a higher reduction potential on poly-crystalline Zn than on Au(111) and Au(100) and thus a smaller EW.[74] Another parameter that limits the stability of an electrochemical system is the oxidation and reduction potential of the electrode. Under certain circumstances, these potentials are exceeded

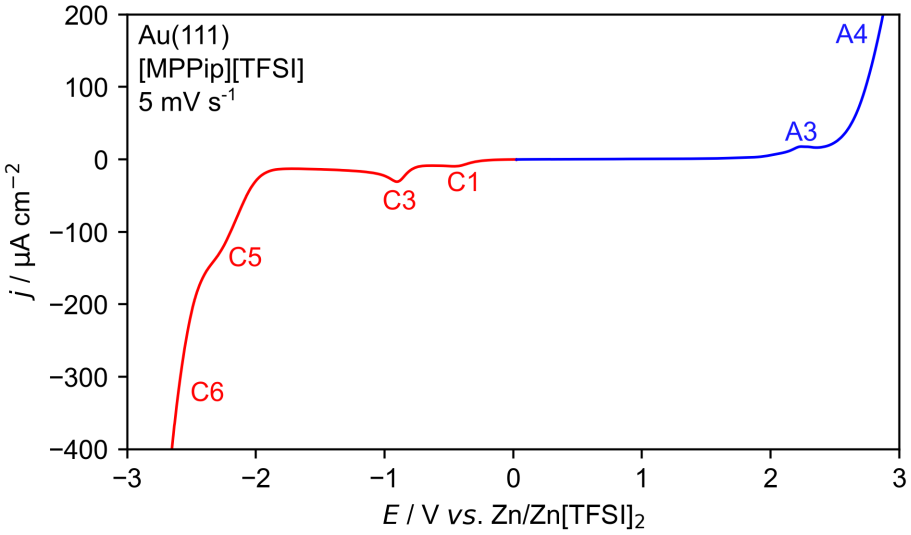

Figure 6.1: Linear potential sweeps for Au(111) recorded in [MPPip][TFSI] with 5 mV s^{-1}. The red curve shows the negative-going scan, and the blue curve shows the positive-going scan. Both measurements were conducted with a freshly prepared set-up.

on purpose, such as during the charging or discharging process of a metal-based battery. For fundamental studies, such as the Na deposition on Au(111) discussed in Chapter 7, it is essential to know the stability windows of the electrolyte and working electrode. Otherwise, it is difficult to distinguish between the electrochemical reactions of the added species and those of the supposedly inert electrode and solvent.

Figure 6.1 shows two independent potential sweep experiments for Au(111) in the IL [MPPip][TFSI]. Both start at 0.025 V, where the electrode and electrolyte are supposedly stable. The red curve shows a negative-going scan, and the blue curve a positive-going scan. Since the reduction and oxidation potential of the electrolyte were far exceeded in the measurements, the back-scans are not shown. The peaks C1 and C3, discussed in Chapter 5, are present in the negative-going scan. At even more negative potentials, the peak C5 appears as a shoulder on the following exponential-like decrease of the current density, denoted as region C6. The well-known peak A1 is not present in the positive-going scan since it was performed in the freshly assembled cell without applying negative potentials in the region of peaks C1 and C3. At 2.2 V, the peak A3 appears, followed by an exponential-like increase of the current density, denoted as region A4. It is not clear if the peak C5 or the region C6 coincides with the reductive decomposition of the IL. Another explanation for one of these peaks could be reductive gold dissolution, called cathodic corrosion. Similarly, the peak A3 could be

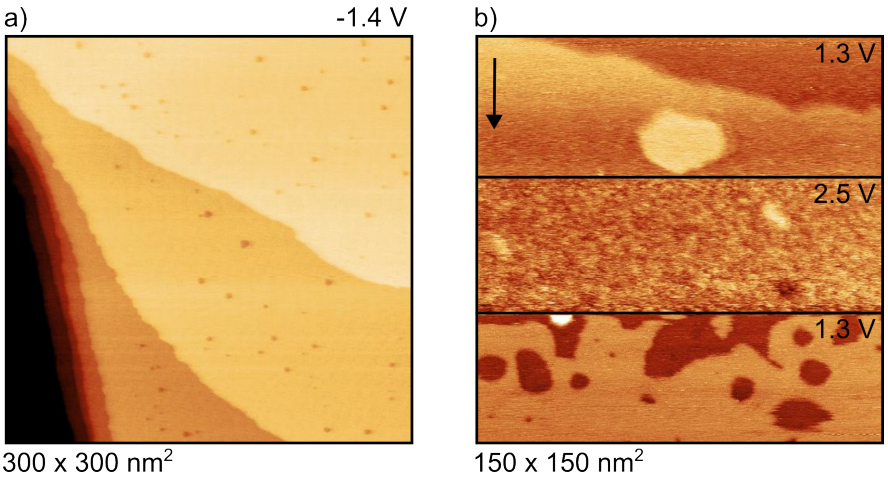

Figure 6.2: *In situ* STM images of a) the cathodic corrosion of Au(111) at –1.4 V and b) the anodic corrosion of Au(111) at 2.5 V in [MPPip][TFSI]. In b) the potential was stepped from 1.3 V to 2.5 V and back at the indicated lines.

induced by Au oxidation.

To gain insights into the underlying processes, *in situ* STM was used. Figure 6.2 shows the first instabilities of the Au(111) electrode a) at –1.4 V in the negative going scan and b) at 2.5 V in the positive going scan. At –1.4 V, monoatomic deep pits formed on the surface. These pits grew with time, and no other restructuring could be observed. This leads to the assumption that the material was etched from the surface. More details on this process will be given in the following section. The top part of Figure 6.2 b was recorded at 1.3 V, positive of the potential region where the herringbone reconstruction is lifted. Therefore, islands of monoatomic height cover the surface. After a potential jump to 2.5 V, the image is very fuzzy. This indicates high mobility at the solid-electrolyte interface and can be caused by ongoing electrochemical reactions or high mobility of surface adatoms and electrolyte components.[71,72] After decreasing the potential again to 1.3 V, the previously flat terrace was covered with holes and islands of one monolayer height. In aqueous solutions of $HClO_4$ and H_2SO_4, pits or pits and islands of one monolayer were observed after one oxidation and reduction cycle of Au(111).[172,173,214] The pits were explained by the dissolution of Au during the oxidation and oxide reduction and the islands by redeposition.[83,172] Interestingly, these structures persisted for some images in the aqueous solution,[172,173] while, in the IL, already the next image showed flat terraces indicating a high mobility of Au adatoms on the surface at the applied potential.

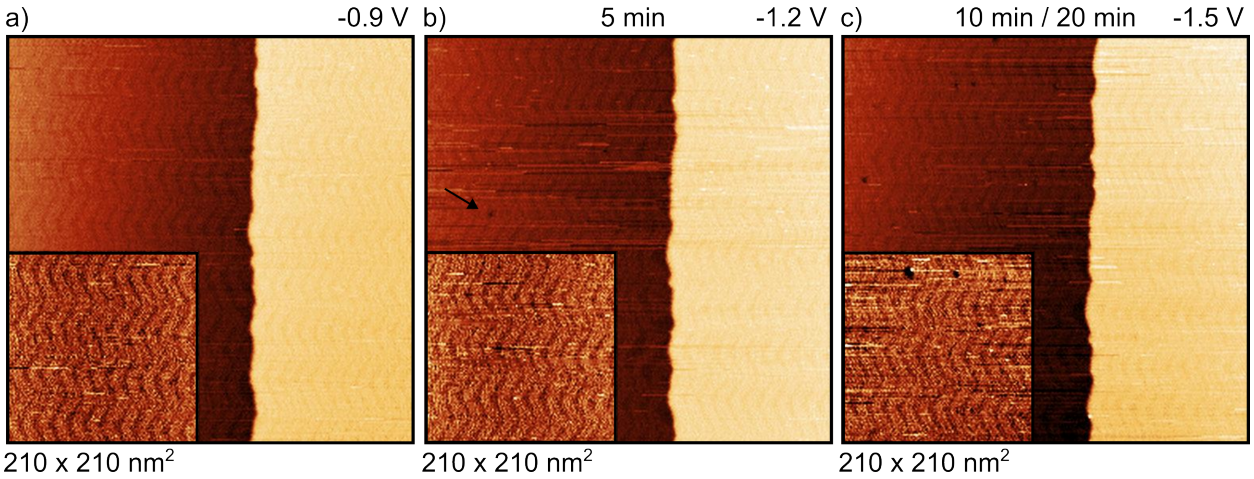

Figure 6.3: *In situ* STM images of the initial stages of the cathodic corrosion of Au(111) in [MPPip][TFSI] with 20 ppm H_2O. The images show a) the reconstructed Au(111) surface at –0.9 V, b) the first pit formation 5 min after the potential was decreased to –1.2 V, and c) the continuing pit formation 10 min after the potential was further decreased to –1.5 V and, thus 20 min after the fist pit formation. The contrast in the left bottom corner was increased to increase the visibility of the surface structures.

6.2 Initial Stages of Cathodic Corrosion

The Figures 6.3 and 6.4 show a series of *in situ* STM images during the initial stage of pit formation on the Au(111) surface in [MPPip][TFSI] between –0.9 V and –1.8 V. All images were recorded by scanning from the top to the bottom of the image. The series starts in Figure 6.3 a at –0.9 V on the reconstructed Au(111) surface. Two terraces, which are separated by a step of monoatomic height, are visible. Both terraces show the herringbone pattern of the $(\sqrt{3}\times 22)$ reconstruction of the Au(111) surface (see region shown with higher contrast in the bottom left corner). Figure 6.3 b shows an *in situ* STM image of the same region of the surface 5 min after the potential was decreased to –1.2 V. Overall, the surface did not change significantly, but the image gets more noisy indicating higher mobility of species on the surface.[71,72] Furthermore, the first pit can be seen marked with an arrow. Since no further significant changes were observed during the investigated time scale, the potential was decreased to –1.5 V. Figure 6.3 c was imaged 10 min after this potential decrease and 20 min after the first pits were observed on the surface at –1.2 V. In the presented image (Figure 6.3 c), a total of six pits have formed on the surface. From the left bottom area where the contrast was increased, it is apparent that the pits form at the so-called 'elbow' sites of the herringbone reconstruction. Even if the

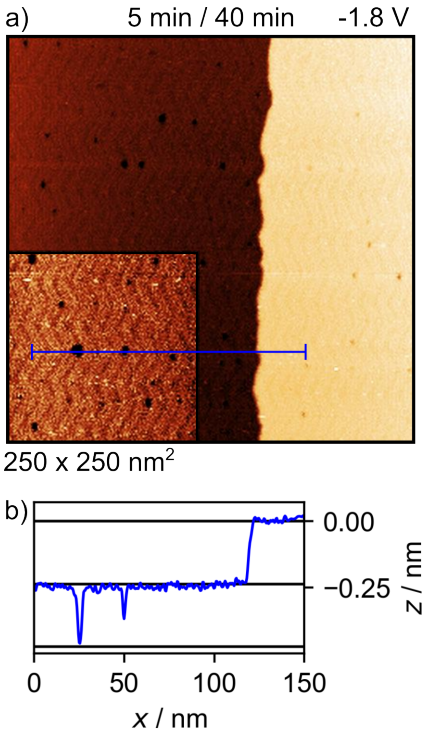

Figure 6.4: a) *In situ* STM images of the ongoing cathodic corrosion of Au(111) in [MPPip][TFSI] with 20 ppm H_2O 5 min after a potential decrease to −1.8 V and, thus 40 min after the initial pit formation. The contrast in the left bottom corner was increased to increase the visibility of the surface structures. b) Height profile of the blue line in a).

image quality makes it hard to distinguish between the pinched and bulged elbows, all pits are formed at the elbows that point to the right. Thus, it might be that one type of elbow is preferred over the other. The parts with increased contrast show that pinched elbows point to the left and bulged elbows to the right. Therefore, it seems that at this stage of the pit formation, pit formation at the bulged elbows is preferred over the pinched elbows.

Figure 6.4 a shows the same region of the surface as in Figure 6.3, recorded 5 min after the potential was decreased to −1.8 V and, thus, 40 min after the pit formation started. The image reveals a significant increase in pits (40 compared to 6 above in Figure 6.3 c). The pits were observed at ca. 10 % of the elbows. Nevertheless, the pit formation is no longer exclusively at the bulged elbows but also the pinched elbows. Still, pits at bulged elbows seem to be preferred with a ratio of ca. 70 %. The depth of the pits was deduced from a line scan illustrated in blue in Figure 6.4 which reveals monolayer deep holes. In black, the step height

of Au monolayer is shown. The left pit in the line scan fits very well with the height of a single atomic Au layer, while the second pit seems less deep. This is, however, possibly simply due to tip convolution effects unless the electronic properties of these sites changed due to the adsorption of species from the electrolyte.[180,181]

While the pits formed at the elbow sites of the herringbone reconstruction, the step edge remained unchanged. This becomes clear when the recorded images are superimposed. Even if the elbow sites of the herringbone reconstruction present the least stable site on the Au(111) terrace, one would expect lower stability of the step edges since the atoms here are less coordinated. It might be that not only the stability of the surface atoms is important, but that other parameters are decisive. It is known that adsorbed hydrogen plays an essential role in cathodic corrosion.[125,130] In alkaline solutions, it is clear that hydrogen originates from the reduction of water.[125,127] In ILs, it was suggested that hydrogen evolved during the reduction of the cation of the IL according to equation 6.1.[131] However, this reaction should not occur positive of the peaks C5 and C6 and thus can be excluded. Hydrogen could also be evolved by reduction of the residual H_2O in the IL. For the measurement shown in Figures 6.3 and 6.4, a vacuum-dried batch of IL with a H_2O content of ca. 20 ppm was used. By reduction of this residual H_2O (Equation 6.2), hydrogen could be formed at much less negative potentials than needed for the decomposition of the IL. As discussed in Chapter 5, this reaction might induce the peak C3 and, thus, starts at ca. −0.5 V. In aqueous electrolytes, the cathodic corrosion starts about 1 V negative of the H_2O reduction.[130] However, in ILs, a H_2O-free layer close to the surface is much easier formed than in aqueous media. Therefore, it can be expected that the onset potential of the cathodic corrosion in ILs is higher than in aqueous media. The main limitation in ILs could rather be the accumulation of enough hydrogen on the surface to stabilise the anionic Au.

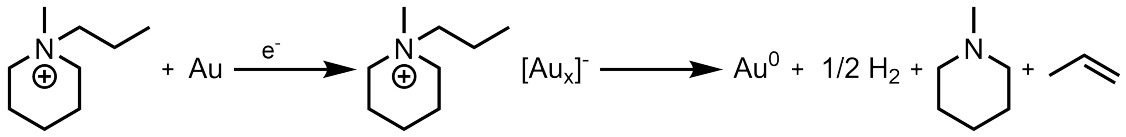

(6.1)

$$2\,H_2O + 2\,e^- \longrightarrow H_2 + 2\,OH^- \tag{6.2}$$

There are two possible explanations why the adsorbed hydrogen could lead to the preferred pit formation at the reconstruction elbows. i) Generally, formed hydrogen deliberately desorbs

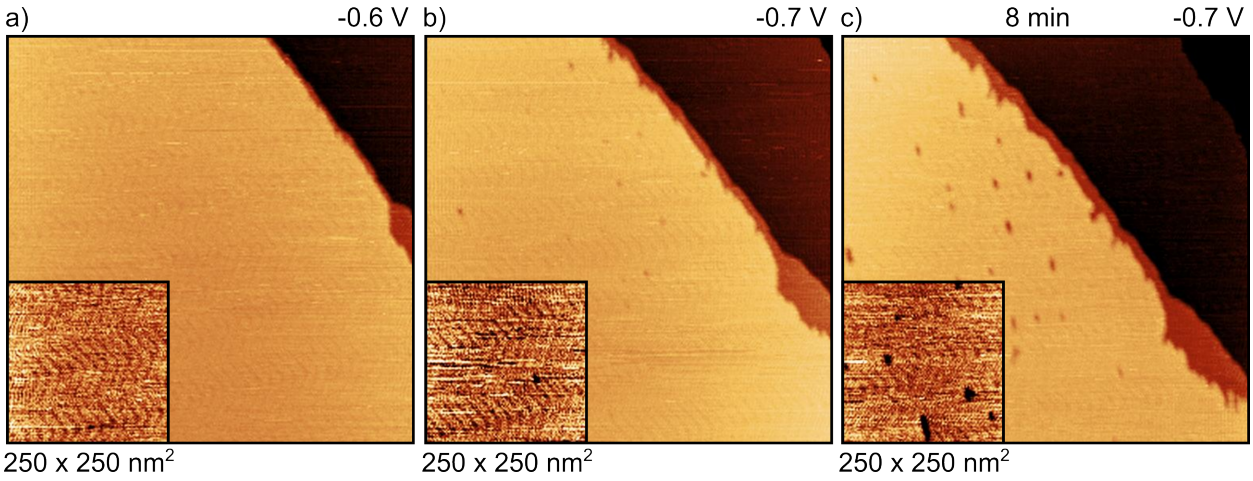

Figure 6.5: *In situ* STM images of the initial stages of the cathodic corrosion of Au(111) in [MPPip][TFSI] with 100 ppm H_2O. The images show a) the reconstructed Au(111) surface at –0.6 V, b) the first pit formation at –0.7 V, and c) the continuing pit formation 8 min after the potential decrease. The contrast in the left bottom corner was increased to increase the visibility of the surface structures.

from Au surfaces and does not accumulate in a huge amount.[93,215,216] Still, it can be assumed that an accumulation at more reactive surface sites, such as the reconstruction elbows and step edges, is possible.[93,216] i) If hydrogen accumulates at the step edge, assuming it can freely diffuse along the edge is reasonable. In contrast, it might be trapped at the reconstruction elbows and accumulate until the pit is dissolved. ii) Since the reconstruction elbows are the reactive sites on the terraces, it might be that the hydrogen formation is preferably happening at these sites. However, it was not observed that the HER activity increased with a higher elbow site density on the surface.[216]

6.3 Influence of H_2O on the Cathodic Corrosion

It is known that H_2O plays a significant role in the cathodic corrosion in nonaqueous electrolytes.[126] Since H_2O should be the main source of hydrogen, it is probable that the H_2O content also greatly influences the here observed pit formation in the IL. Therefore, additional measurements with ILs containing larger amounts of H_2O (100 ppm and 200 ppm) were performed. Figures 6.5 and 6.6 show a series of *in situ* STM images of Au(111) in [MPPip][TFSI] with a H_2O content of 100 ppm. All images were recorded from bottom to top. The STM image

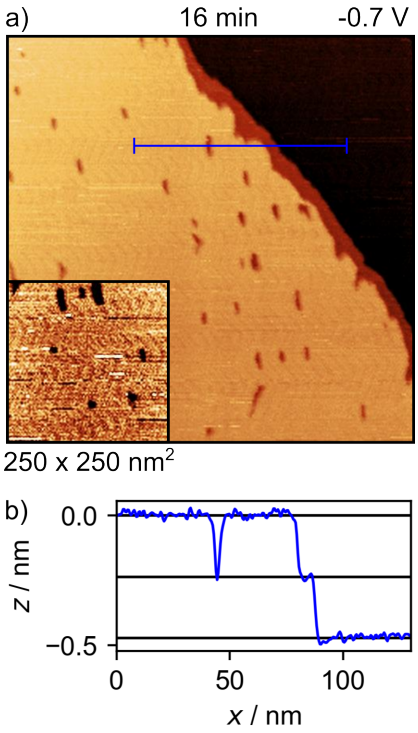

Figure 6.6: a) *In situ* STM images of the ongoing cathodic corrosion of Au(111) in [MPPip][TFSI] with 100 ppm H_2O 16 min after the potential decrease to –0.7 V and b) Height profile of the blue line in a). The contrast in the left bottom corner was increased to increase the visibility of the surface structures.

in Figure 6.5 a was measured at –0.6 V on the reconstructed Au surface. In the part of the image in which the contrast was increased, the herringbone reconstruction is clearly visible. Two step edges can be seen in the image's top-left corner. In Figure 6.5 b, the STM image was recorded after a potential step to –0.7 V. This led to two changes: i) On the upper terrace, pits were formed at the herringbone reconstruction's elbows sites. ii) The topmost step edge has some fissures. Figure 6.5 c shows the surface 8 min after the potential change. The number of pits has increased, and some pits also increased in size. Also, some pits and fissures grew, and it seems they are formed parallel to the reconstruction lines. Interestingly, no significant changes could be observed at the other imaged steps or terraces.

Figure 6.6 a shows the surface 16 min after the potential change to –0.7 V. The pits have now grown, mostly parallel to the reconstruction lines. The fissures in the step edge have broadened and the step edge looks much smoother than in the previous image. Note that now a similar number of pits cover the surface as for the H_2O content of 20 ppm after 40 min and a

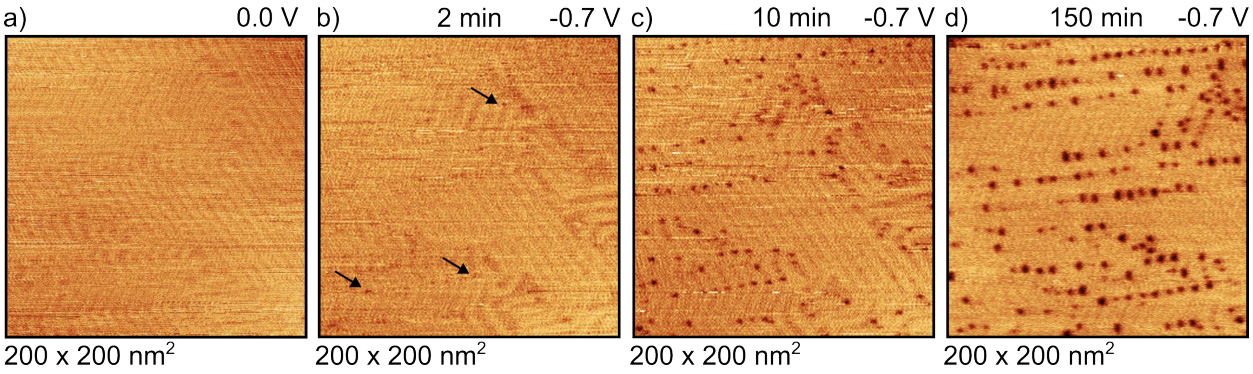

Figure 6.7: *In situ* STM images of the initial stages of the cathodic corrosion of Au(111) in [MPPip][TFSI] with 200 ppm H_2O. The images show a) the reconstructed Au(111) surface at 0.0 V, b) the first pit formation at –0.7 V, and the continuing pit formation c) 10 min and d) 150 min after the potential decrease.

potential decrease to –1.8 V. Figure 6.6 b shows a line scan along the blue line in Figure 6.6 b, running across the step edge. The step height of Au is shown by the black horizontal lines. The pit depth is comparable to that of a monoatomic Au step on Au(111).

The pit formation in ILs containing 100 ppm H_2O differs from that in ILs with 20 ppm H_2O. i) The pit formation starts 0.5 V more positive potentials. ii) The pit number increases more quickly. iii) The step edges also change.

Next, the H_2O content was increased to 200 ppm. Figure 6.7 shows a series of *in situ* STM images of the Au(111) surface during the initial pit formation after decreasing the potential from 0.0 V to –0.7 V. All images were scanned from top to bottom. At 0.0 V, the reconstructed surface does not show any pits (6.7 a). The imaged area only shows one terrace and, thus, no steps. Figure 6.7 b shows the same region 2 min after the potential sweep to –0.7 V was finished. The noise level has slightly increased, which is a sign of increased mobility of adatoms on the surface or ongoing surface reactions.[71,72] In some regions, small pits started forming, either at the elbows or the U-turns of the reconstruction lines. Some of these positions are marked with arrows. This behaviour is similar to what has been observed for the same electrolyte with lower H_2O contents. Figure 6.7 c shows the same region 10 min after the potential decrease. Now, pits have formed at most elbow sites of the reconstruction lines. These pits cover ca. 1.5 % of the imaged surface area (Due to the small size of the pits and tip convolution effects, the number should be taken with caution). Within the next images, the surface is not changing a lot. Overall, the existing pits have grown, and a few new pits have formed.

Figure 6.7 d shows the surface after 150 min. The imaged area drifted to the left compared to the other images. Nevertheless, it is apparent that the pits have grown, covering ca. 5 % of the surface.

To illustrate the evolution of the pit formation for ILs with different H_2O content, the pit coverage, number and average size were determined, which is illustrated in Figure 6.8. Note that the potential was constant at −0.7 V for the measurement of the IL with a water content of 100 ppm and 200 ppm, while it was decreased from −1.2 V to −1.8 V for the IL with a water content of 20 ppm. It is apparent that the percentage of the pits is higher with a higher H_2O content in the IL. Note that during the investigated time, the pit coverage for a H_2O content of 20 ppm is almost negligible. Even if the differences in the graph seem relatively low, the percentage coverage after 25 min with 200 ppm is ca. 55 % higher than with 100 ppm. Visibly large deviations are apparent for the number of pits and pit size. The increase of H_2O content from 20 ppm to 100 ppm did not lead to a significant increase in the number of pits. However, this pit number increased faster with 100 ppm water content than with 20 ppm. The water content increase from 100 ppm to 200 ppm dramatically changed the pits' number. For the average pit size, the trend is different. Here, the number is highest for the H_2O content of 100 ppm, whereas the other measurements show fluctuations of small numbers from image to image. These fluctuations can be explained by the small sizes of the pits, which are more challenging to measure.

To explain these trends, the driving force and necessary conditions for cathodic corrosion must be considered. The driving force is an increased surface stress induced by the high negative charge at the electrode.[126,130] It can be assumed that this surface stress is independent of changes in the H_2O content in the electrolyte, especially of relatively small changes as studied here. This surface stress can be reduced by 'ejecting' negatively charged atoms or clusters from the surface. This is expected to occur at surface defects at which the atoms have lower coordination numbers, such as at step edges and the elbow sites of the herringbone reconstruction. Other parameters that come into play are the necessary conditions for forming these anionic metal species. As mentioned above, adsorbed hydrogen plays an important role, and for the investigated system, the residual H_2O is expected to be the hydrogen source. The more H_2O is present in the electrolyte, the more hydrogen can be formed at the solid-electrolyte interface and, thus, adsorb on or absorb into the Au. A specific amount of adsorbed hydrogen is likely needed to dissolve the anionic Au in the electrolyte. The more H_2O is in the electrolyte, the more hydrogen is adsorbed on the electrode, and thus, the dissolution can occur

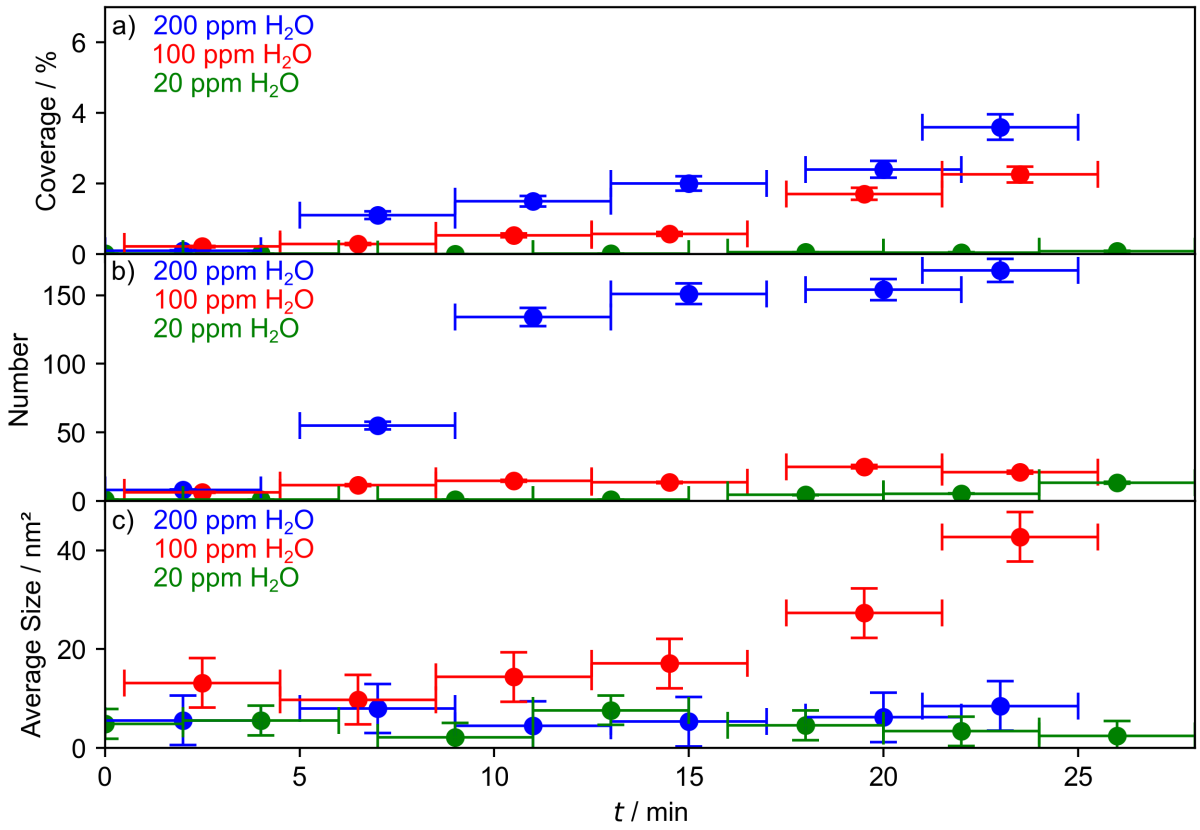

Figure 6.8: Comparison of the pits formed during the initial stages of cathodic corrosion regarding surface coverage, number and average size in dependence on the H_2O content in the IL. Since the areas of the images were different, the pit number is normalised to an area of 200 nm×200 nm. The potential was constant at –0.7 V for the measurements in the IL with a water content of 100 ppm and 200 ppm. For the measurements in the IL with a water content of 20 ppm it was gradually decreased from –1.2 V to –1.8 V.

at more sites simultaneously. In contrast, if the H_2O content is lower, fewer dissolution spots are present; therefore, more material has to dissolve from those spots to relieve the surface stress. This might explain why more pits are formed at higher H_2O content while larger pits are formed at lower H_2O content.

Another difference between the measurements with high and low H_2O content is the large difference in the onset potential for the onset of pit formation. Two possible explanations can be derived from the measurements shown here. The first relates to hydrogen coverage. With a H_2O content of 20 ppm, the first pit formation was observed at potentials negative of peak C3, which was associated with H_2O reduction. These overpotentials might be required to reach sufficient hydrogen coverage on the surface. Likewise, the potential must be decreased further to increase the number of pits. As mentioned above, hydrogen does not accumulate on the surface as deliberately as it does on *e.g.* Pt or Pd.[93,215,216] If the rate of hydrogen formation decreases, it can be assumed that the local concentration at the electrode is decreasing. The higher the overpotentials for the H_2O reduction is, the more hydrogen is formed as long as the process is not limited by the diffusion of H_2O to the electrode. Therefore, a more negative potential is needed for low H_2O contents to get sufficient hydrogen concentrations on the surface for cathodic corrosion. Another possible explanation of the differences in the onset potential of the pit formation is based on variations of the structure of the herringbone reconstruction before the pit formation. The reconstruction lines are well-ordered and uniform in the measurement with 20 ppm H_2O at –0.9 V. Typically, the electrochemically induced reconstruction is less ordered.[216] This leads to the assumption that the thermal surface reconstruction was not lifted during the CV measured at the beginning of the measurement due to shifts of the reference electrode. It was only cycled to potentials slightly positive at the onset of the peak A1, which might not be sufficient to lift the surface reconstruction. Therefore, it can be assumed that this measurement starts on the thermally reconstructed surface. It is known that the thermally reconstructed Au(111) surface is less active for the HER than the electrochemically reconstructed surface and has higher overpotentials for this reaction.[93,216] This could also explain the high overpotential in the measurement with the lowest water content.

Another effect observed with the increasing H_2O content was a dissolution of Au at the step edges, which was not observed with 20 ppm H_2O. Different reasons might explain this behaviour. i) With the increased amount of hydrogen on the surface, as discussed above, hydrogen might accumulate at the step edges and the elbow sites of the reconstruction pattern. It might be that at the step edges, the adsorbed hydrogen diffuses along the step edges, while it

is more confined at the elbow sites. Thus, the affordable coverage of hydrogen for the cathodic corrosion is easier to reach at the elbow sites. When the concentration of water and thus of adsorbed hydrogen increases, enough adsorbed hydrogen could accumulate at specific sites of the step edges as well, *e.g.* at kink sites. ii) Another parameter that was not monitored is the content of residual O_2. As shown in the last chapter, it might be that the O_2 content is increased as well if the H_2O content is increased. It might be that O_2 or the products formed during the ORR also influence the pit formation. iii) Taking a closer look at the STM images (Figures 6.3,6.5) reveals that the step edges appear quite differently. As mentioned above, the reconstruction lines are rather uniform in the measurement with 20 ppm H_2O (Figure 6.3). They alternate directions in parallel, and the distance between the elbow sites is rather similar. Also, the step edge is mainly parallel to the reconstruction line next to it. It might be that this step edge is more stable than step edges with different orientations and, thus, is less prone to restructuring processes. In the measurement with 100 ppm H_2O, some reconstruction lines have U-turns at the step edges. These sites seem to be prone to the formation of fissures.

A possible mechanism for the restructuring of the Au (111) surface in the presence of H_2O is summarised in a schematic illustration in Figure 6.9. For simplicity, the charges of the ions of the IL are not shown, and the Au(111) surface is imaged as a flat surface, neglecting the reconstruction lines. Note that the pit formation happens, in fact, at the elbow sites of the herringbone reconstruction. First, the residual H_2O is reduced at the Au(111) surface, forming OH^--ions and hydrogen atoms. Some of the hydrogen adsorbs or is absorbed into the negatively charged Au(111) electrode. To relieve the surface stress, negatively charged Au atoms or clusters, which are stabilised by adsorbed hydrogen, as well as by the cations of the ionic liquid, are ejected from the surface. Next, the anionic Au clusters or atoms are reoxidised by H_2O, O_2, or other reactive residues in the electrolyte, agglomerate to nanoparticles, or redeposit on the surface. Such information is complicated to derive from the underlying measurements. Therefore, what happens to the dissolved Au remains unclear. Nevertheless, the formation of new islands/clusters by redepostion was not observed in the imaged area during the measurement. It is hard to say if redeposition happened at other potentials due to the huge morphology changes on the surface, which occurred independently of the cathodic corrosion and will be discussed below.

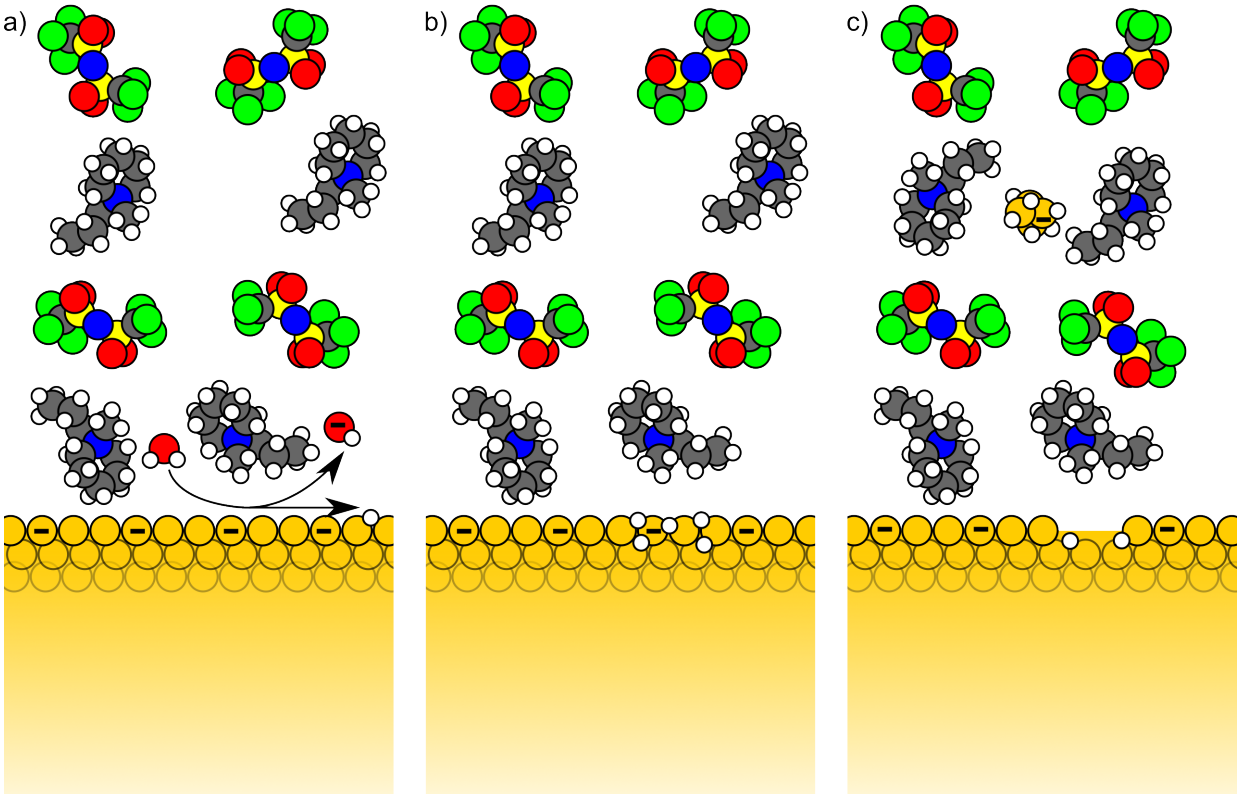

Figure 6.9: Scheme of the cathodic corrosion in ILs. a) Residual H_2O is reduced and OH^- and hydrogen are formed. b) Hydrogen accumulates on the surface. c) Stabilisation of a negatively charged Au cluster by cations of the IL.

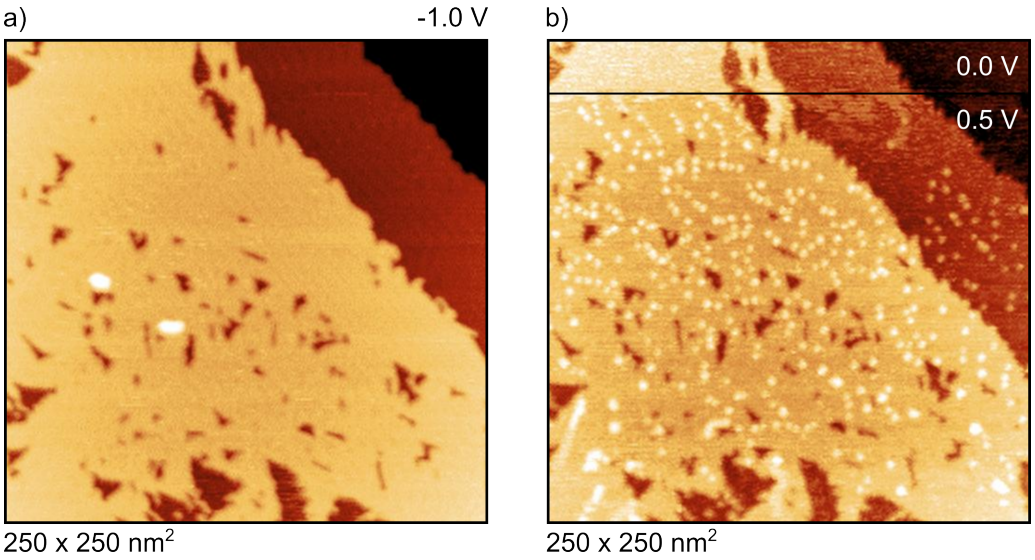

Figure 6.10: *In situ* STM images a) the reconstructed Au(111) surface in [MPPip][TFSI] with 100 ppm H_2O after the cathodic corrosion at –1.0 V. b) Lifting of the reconstruction in the topmost part of the image by stepping from 0.0 V to 0.5 V. The image was recorded from top to bottom.

6.4 Formation and Lifting of the Reconstruction

Noble metals, such as Au or Pt, undergo surface reconstruction at elevated temperatures to enhance the coordination of the surface atoms.[88] Au is the only fcc metal that shows a reconstruction of the (111) plane.[90,217] Furthermore, for the low-indexed Au surfaces, both the formation and lifting of the reconstruction can be induced electrochemically.[88] From other electrolytes, it is known that the species in the electrolyte and the applied potential have a huge impact on the morphology of the surface reconstruction and the island formation after the lifting of the reconstruction. Figure 6.10 a shows the reconstructed Au(111) surface at –1.0 V. The pits on the upper terrace were previously induced by cathodic corrosion. Nevertheless, the reconstruction lines on the upper terrace are visible. During the following potential step to 0.0 V, the image quality decreased and the reconstruction lines could not be resolved. The image in Figure 6.10 b was recorded from top to bottom and showed the same region during a potential step in the top part of the image from 0.0 V to 0.5 V. After the potential step, many islands formed on the surface, which cover about 8 % of the surface. Compared to the 4 % Au excess atoms in the reconstructed Au(111) surface this number is rather large. Several parameters can contribute to this high number. First, it might be that the material, which was

dissolved during the cathodic corrosion in the previous images, is redeposited. However, this high island coverage was observed not only if the cathodic corrosion had happened before. Another explanation can be that the small islands are imaged huger as they are due to tip convolution effects.[180,181] It might even be that in the used IL, the reconstructed Au(111) layer in deed covers more atoms than 4 %. According to DFT calculations, the ($\sqrt{3} \times 22$) reconstruction is only the most stable surface configuration.[217] Nevertheless, theoretical calculations show that even other ($\sqrt{3} \times p$) structures are possible.[217]. Thus, it could be possible that the reconstruction lines formed in [MPPip][TFSI] have smaller distances than expected, and thus, the first layer is even more compressed. Nevertheless, this would be hard to prove since atomically resolved images would be needed. Since no reports of such effects for any electrolyte are known, it can be assumed that an overestimated size is the reason for the high amount of island coverage.

Comparing Figure 6.10 a and b reveals that some islands form chains which follow the previous reconstruction lines. This indicates that the mean free path of the Au atoms under the applied conditions is very small. This could originate from the applied potential or the high number of surface defects, such as holes. However, other measurements in this IL showed that even with a lower amount of surface defects, rather small islands form after the lifting of the reconstruction at potentials between 0.4 V and 0.6 V. From measurements in a deep eutectic solvent, it is known that some anions in the electrolyte, such as Cl^-, enhance the surface mobility, and thus, the excess atoms are deposited on the step edges and no islands or only huge islands form.[94] In the IL studied here, the opposite seems to be true, and the atoms are not very mobile. Therefore, many small islands form and are stable at the applied potential. It was shown that even smaller islands than the here observed ones are observed in the presence of adsorbed adenine.[218] This was explained by a decreased mobility of the Au atoms due to the adsorbed adenine.[218]

6.5 Role of O_2 on Structural Changes

In the previous chapter, it was shown that O_2 plays a crucial role in the interpretation of the CVs for Au(111) in [MPPip][TFSI]. Here, we demonstrate its role on the structural changes. The following measurements were conducted with a batch of [MPPip][TFSI] with 100 ppm H_2O. Furthermore, they were done about 20 h after the set-up of the STM, and it can be expected

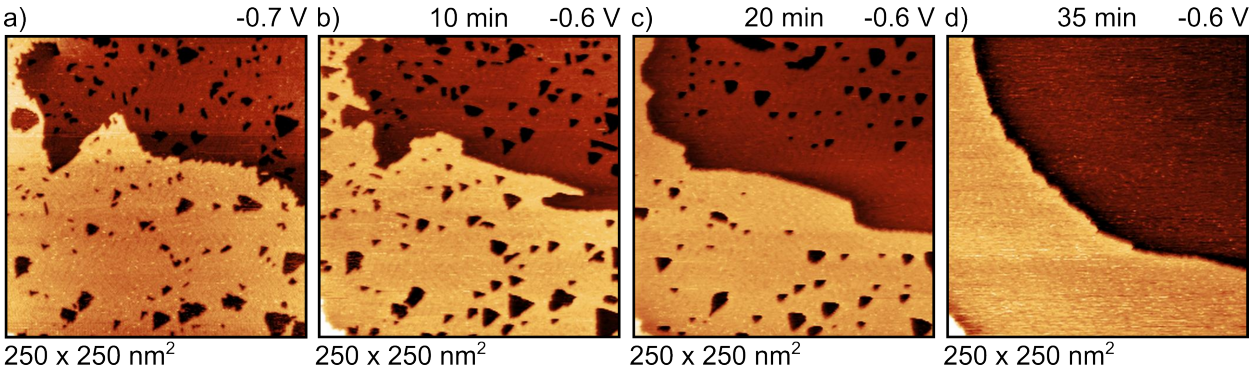

Figure 6.11: *In situ* STM images of surface restructuring of Au(111) in [MPPip][TFSI] with 100 ppm H_2O. a) The surface after the cathodic corrosion at –0.7 V with many monolayer deep holes, merging of the holes and restructuring of the step edge b) 10 min, c) 20 min, and d) 35 min after a potential step to –0.6 V. All images were recorded from top to bottom.

that in this period, the O_2 content in the inert container significantly increased. Indications of this were also observed by an increase of the peak C1 in the CVs recorded in between the *in situ* STM measurements.

Figure 6.11 shows a series of *in situ* STM images recorded from top to bottom. The first image of the series Figure 6.11 a was recorded after the cathodic pit formation had proceeded for ca. 1 h at –0.8 V. Figure 6.11 a shows the surface at –0.7 V with many small pits and even larger holes which formed during the polarisation at –0.8 V. All holes and pits are one monolayer deep and the surface did not significantly alter at the applied potential of –0.7 V. Surface restructuring starts after increasing the potential to –0.6 V. The image in Figure 6.11 b was taken 10 min after the potential was increased. Some of the small pits have coalesced, and the step edge has significantly changed. It seems that some material from the upper step edge has been dissolved. As a result of the restructuring, many holes show a triangular shape, and the step edges, which were previously rather irregular, are now preferentially following three of the six possible directions given by the unit cell of the surface. This means that one of the step types {111} and {100} seems to be preferred over the other type. Differentiation is possible by following the reconstruction lines, which only cross {111} step edges.[86,87] Here, preferably {111} step edges are formed.

Figure 6.11 c shows the same part of the surface 20 min after the potential change to –0.6 V. Now, many of the monolayer deep holes have vanished or become smaller. Whereas in the

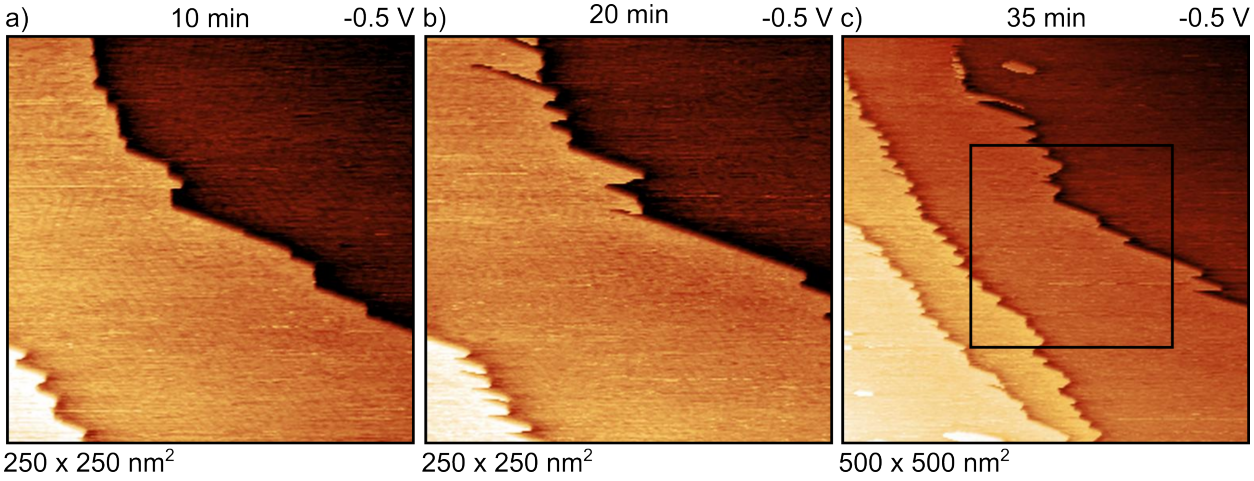

Figure 6.12: *In situ* STM images of surface restructuring of Au(111) in [MPPip][TFSI] with 100 ppm H_2O a) 10 min, b) 20 min, and c) 35 min, and d) 35 min after a potential step to −0.5 V. In c), the imaged area was increased, and the before imaged area is depicted with the black box. All images were recorded from top to bottom.

last image (Figure 6.11 b), some holes and step edges had rather sharp angles, they are now more round shaped and the triangles are truncated. This indicates that the {111} step edges are no longer that dominant than in the last image.

Figure 6.11 d shows the surface 30 min after the potential change. Now, the holes have completely vanished, and the step edges do not show any preference for a certain kind of structure. It seems that all surface defects formed during the pit corrosion have healed out.

Figure 6.12 shows a series of STM images recorded after further increasing the potential to −0.5 V after a) 10 min, b) 20 min, and c) 35 min. All images were recorded from top to bottom. After increasing the potential to −0.5 V, the step edges, which were somewhat irregular before (see Figure 6.11), rearranged such that parts of them are straight with sharp angles between. Again, it seems that the step edges are mostly oriented in the {111} direction, with a minor amount of {100} step edges. After 20 min, channels grow from the step edges into the upper terrace, while at other parts of the step edge, the upper terrace grows. This, again, leads to an increase of the {111} step edges. Figure 6.12 c shows a larger scale image of the same region 35 min after the potential was increased. The previously imaged part of the surface is shown with a black frame. Both channels at the step edge, which were shown in the former images, have vanished again, but similar channels or finger-like structures can be seen in other parts of the electrode. Additionally, some islands appear in the top and bottom parts of the image.

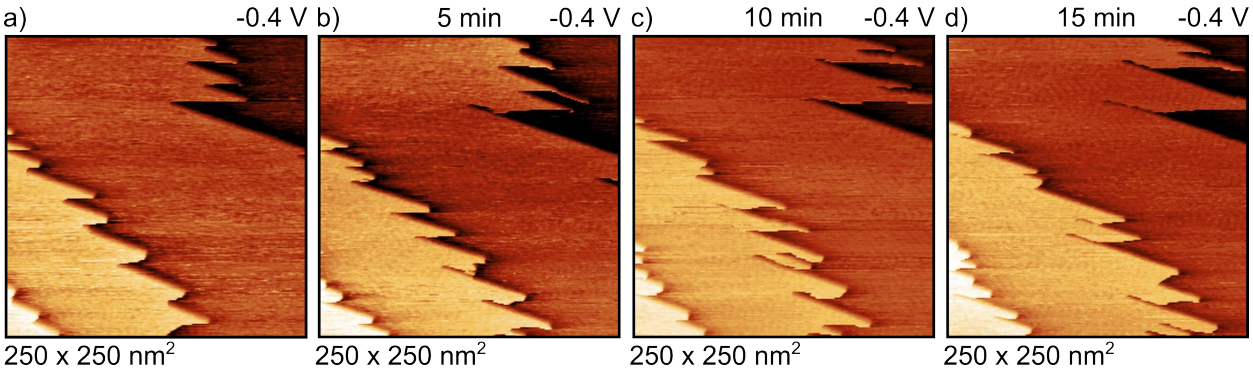

Figure 6.13: *In situ* STM images of surface restructuring of Au(111) in [MPPip][TFSI] with 100 ppm H_2O a) directly, b) 5 min, c) 10 min, and d) 15 min after a potential step to –0.4 V. The images a) and c) were revorded from bottom to top, and b) and d) from top to bottom.

It might be that such islands do not grow in the part that was imaged previously since the tip moves mobile surface atoms to the step edges. Overall, in the image, again, the step edges are mostly oriented in the {111} direction.

Figure 6.13 shows a series of STM images recorded after the potential was increased to –0.4 V (recorded subsequently, to those shown in Figure 6.12). The images were recorded after a) the increase of the potential, b) 5 min, c) 10 min, and d) 15 min after increasing the potential. Figure 6.13 a and c were imaged from bottom to top, and b and d from top to bottom. The surface changes during the images are relatively small, but again some channels and fingers form at the step edges. Some of them can only be observed in one image, while others persist from Figure 6.13 b to d. Overall, the step edges still show a preferred {111} orientation, and all channels and fingers that grow have mainly {111} step edges.

Additional, to the structural changes in Figures 6.11–6.13, the measured step height increased from the image in Figure 6.11 a with the usually measured height of 200-300 pm to the doubled value of ca. 500 pm in Figure 6.11 b and values up to 1280 pm in the following images. The step heights for the images shown in this section are summarised in Table A.5 in the Appendix, including the step heights of the images in Figure 6.5–6.6 which were recorded in the same measurement. The difference in height can not be inferred from the images since the colour scale of each image was adapted to the terraces. Note that deviations of up to 100 pm from the geometric height of 236 pm within one line are quite usual with the used setup. Still, all values given here are averaged over several lines, which usually results in deviations

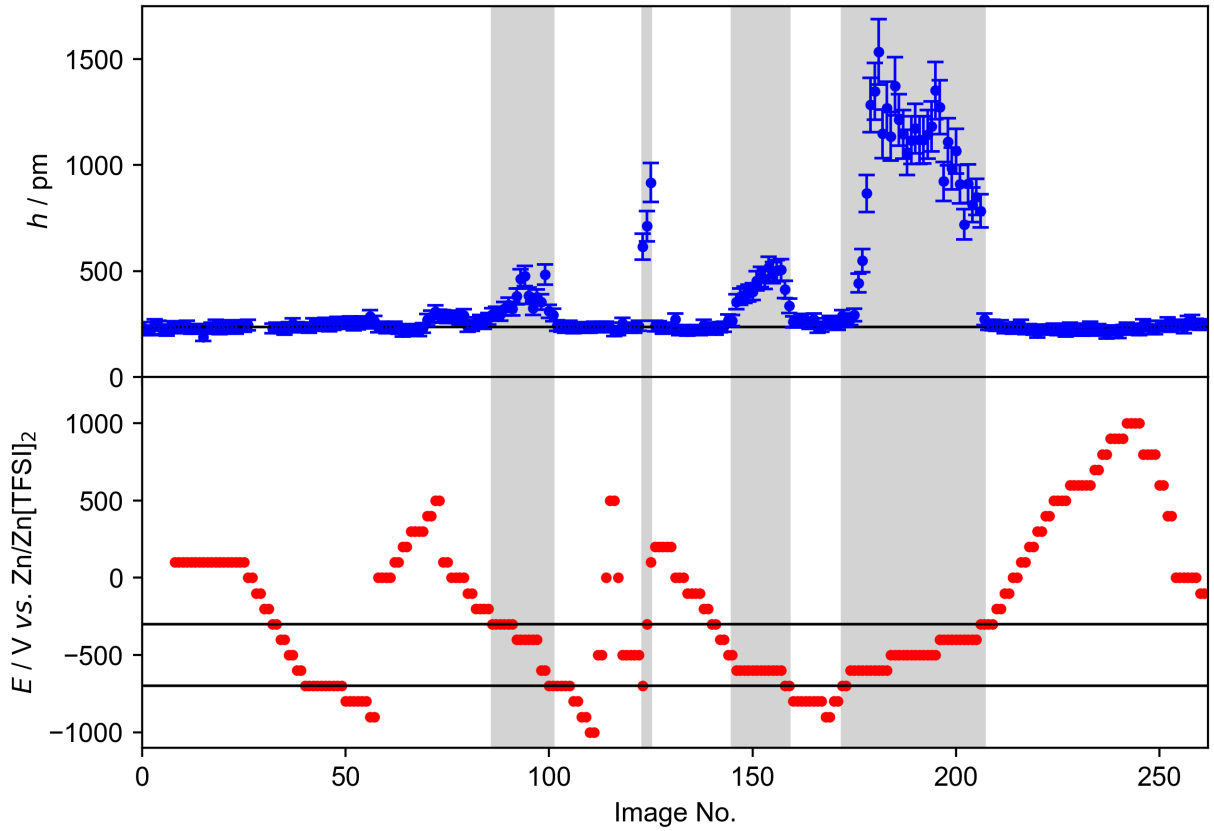

Figure 6.14: Step heights (blue) and corresponding potential (red) of all images of the measurement of Figures 6.5, 6.6, 6.11,6.12, and 6.13. The images with significantly increased step heights are indicated with the grey background. The expected step height and the potentials in between the height changes were observed are indicated with black lines.

smaller than 20 pm. Thus, the doubled height is already far more than typical deviations. The increase in the step height observed during the series of images is difficult to explain. If an adsorbate covers the surface, it should not change the height, even if it is a different size than the Au(111) step height, since it usually covers both terraces. The only possible explanation for the observed change of the geometric height would be a process which only affects one of the layers, *e.g.*, an insertion of material underneath that layer. However, this would mean that the insertion in the lower terrace stops nearly exactly where the upper terrace starts, which seems unrealistic. A more probable explanation is that the height measurement is incorrect. One should remember that the shown height correlates with the tunnelling current even in the constant current mode. In particular, chemical reactions are known to induce noise in the STM measurements.[219,220] However, this usually only leads to a small perturbation and no increase in a complete step. Here, it seems rather likely that species in the electrolyte permanently influence the current signal of the tip.

To get more details about both these differences, an overview of the measured step heights in all images of this measurement is shown in Figure 6.14, including the applied potential. All height deviations were measured in the potential range of –0.7 V to –0.3 V. This potential range covers the potentials at which the ORR is considered to take place. The step heights in the positive-going scan show higher deviations than in the negative-going scan, and the deviations increase with measurement time. This leads to the assumption that the deviations are induced by a species formed at negative potentials, accumulates in the electrolyte, and induces Faraday currents at the tip, changing the response signal of the STM. Most likely, H_2O_2 or even more reactive species which are formed during the ORR are involved in this process. Also, it might be that adsorption of these species is preferred at the {111} step edges and thus stabilises them.

6.6 Overview on Surface Structures of Au(111) in [MPPip][TFSI]

Au electrodes are often used due to their high electrochemical and chemical stability.[56–58,83] However, in the previous sections, it was shown that the morphology of Au(111) undergoes many changes within the electrochemical stability window of the IL on Au(111). Figure 6.15 summarises the different processes which influence the surface structure of Au(111) in the IL

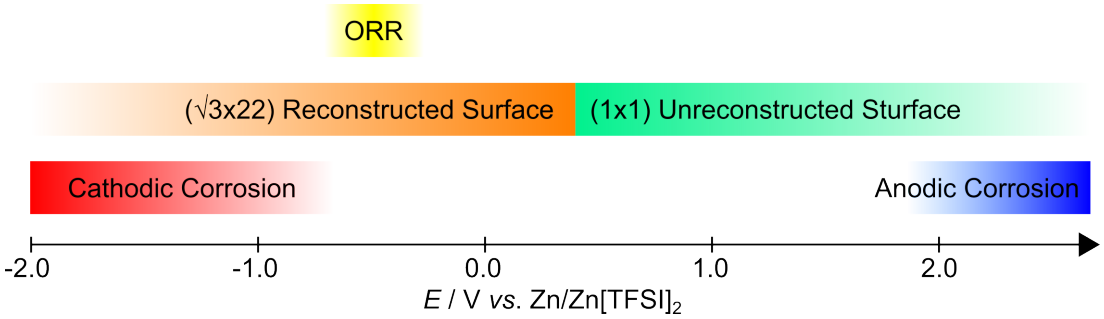

Figure 6.15: Potentials of surface restructuring processes of Au(111) in [MPPip][TFSI].

[MPPip][TFSI]. The cathodic corrosion starts between –1.2 V and –0.7 V depending on either different conditions for the formation of the herringbone reconstruction or the H_2O content. Due to the ORR, instabilities of the surface can already appear between –0.7 V and –0.3 V. At positive potentials, the anodic corrosion begins around 2.0 V. Furthermore, the rearrangement between the reconstructed and unreconstructed surface occurs at ca. 0.4 V. This shows that the morphology of the Au(111) electrode is far from stable under the present conditions despite the fact that Au is considered chemically and electrochemically stable.[56–58,83]

7 Alkali Metal deposition on Au(111) from [MPPip][TFSI]

7.1 Sodium Deposition on Au(111) from [MPPip][TFSI]

Some parts of this section have previously been published in the article "Initial Stages of Sodium Deposition onto Au(111) from [MPPip][TFSI]: An In-Situ STM Study for Sodium-Ion Battery Electrolytes".[205]

The Na deposition on Au(111) was first investigated by cyclic voltammetry to find the potentials where electrochemical processes occur. In the next step, the system was investigated by *in situ* STM, resolving the morphology of the Na deposits. In the last step, the bulk alloying between Na and Au at overpotentials was studied in more detail by cyclic voltammetry. All potentials in this section are referenced against the Na/Na^+ redox couple.

7.1.1 Electrochemical Overview

Figure 7.1 shows several CVs for Au(111) in a solution of 200 mM Na[TFSI] in the IL [MPPip][TFSI]. The starting potential was 2.55 V, the UPL 4.15 V, the scan rate 5 mV s^{-1} while the LPL was gradually decreased from 1.25 V, to 1.05 V, 0.65 V, 0.05 V and −0.05 V. Positive of 1.45 V, the electrochemical behaviour is the same as for the pure IL. The observed features can be categorised as follows: i) The peaks C1', C2', and A1' are known for the pure IL of type I (compared to chapter 5) and marked in black. ii) The cathodic peaks C1 to C5, which are only present if Na[TFSI] was added to the IL, are assigned to the Na deposition and can be divided into the UPD peaks C1 to C4 positive of 0.0 V and the OPD negative of 0.0 V. iii) The peaks A1 to A5 are only present if Na[TFSI] was added to the IL and the peaks which were

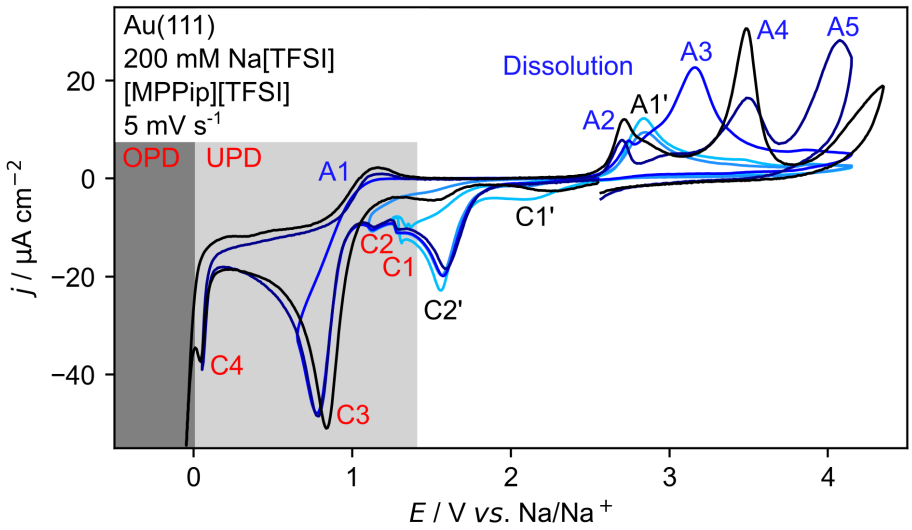

Figure 7.1: CVs for Au(111) recorded in a 200 mM solution of Na[TFSI] in the IL [MPPip][TFSI]. The LPL was gradually decreased from 1.25 V, to 1.05 V, 0.65 V, 0.05 V and −0.05 V while the UPL was kept at 4.15 V and the scan rate was 5 mV s^{-1}. The peaks marked in red and blue are assigned to the Na deposition and dissolution with the UPD above and the OPD below 0 V. The black peaks with prime labels are assigned to processes which are independent of the Na salt (see section 5).

Table 7.1: Approximate values of the peak potentials in Figure 7.1. All given values refer to the first curve (highest LPL) where the peak appeared. For C5, no peak potential can be assigned since it is not reached before the LPL.

Peak	***E*** **/ V**	**Peak**	***E*** **/ V**
C1	1.3	A1	1.15
C2	1.15	A2	2.75
C3	0.75	A3	3.15
C4	0.7	A4	3.45
C5	-	A5	4.05

assigned to the Na deposition were passed in the previous negative-going scan. Therefore, these peaks can be associated with the Na dissolution. All approximate peak potentials are given in Table 7.1. Peak potentials are not always the best measure since they depend on the concentration and scan rate. Still, due to the overlaps of different peaks, it is hard to determine onset potentials in the shown measurements.

The consecutive lowering of the LPL reveals some relations between the deposition and the dissolution peaks. The first occurring deposition peaks C1 and C2 are correlated with small humps between 1.2 V and 1.4 V in the following positive-going scan, which are not assigned as peaks and only occur as long as there are no other deposition peaks. Despite these humps, no influence of the peaks C1 and C2 on the peaks in the following positive- or negative-going scan can be seen. Significant changes in the positive-going scan happened after the peak C3 was passed. The current density remained negative in the previous cycles until a potential of ca. 1.8 V was reached. This behaviour is often observed in ILs and attributed to residual impurities, such as H_2O and O_2.[115] After passing the peak C3, the current density returns to zero at ca. 1.0 V. At higher potentials, the changes in the CV are even more pronounced. The peak A1', known from the pure IL, is now only a small shoulder, whereas the peak A2 appears at a potential slightly negative and the peak A3 positive of the peak A1'. A further decrease of the LPL beyond peaks C4 and C5 enhances these changes. In the positive-going scan, the peak A3 decreases while the new peaks A4 and A5 appear at even more positive potentials. Note that changes in the relative intensity of the dissolution peaks are not only induced by changes in the LPL but also by potential cycling. Despite that, the peak C3 is increased by each cycle with an LPL positive of the onset of the peak C4. If the peak C4 is reached, the

peak C4 is enhanced by cycling. The peak A5 seems to shift to more positive potentials with every cycle. Thus, it is often only visible in the first cycle after passing the peak C4.

From these CVs much information about what happens during the Na deposition can be gained. The UPD peaks C1 and C2 are only small humps and do not cover much charge. In contrast, the UPD peak C3 covers approximately 5.6 mC cm^{-2} which has a monolayer equivalent of 25 monolayers. This number is much higher than expected for the UPD.[134,136] Usually, the beneficial interaction between the deposit and substrate only influences the first layers.[134,136,138,139] Suppose that the peak C3 is related to Na deposition; it is expected that deposited Na does not block the electrode for further UPD. Possible consecutive reactions are a reaction with the electrolyte by decomposing the IL or an alloy formation with the Au(111) bulk, which exceeds surface alloying. Another indication of a reaction of the deposited Na are the dissolution peaks, which are several volts more positive than the deposition peaks. Still, it seems that the system is not irreversibly altered, *e.g.* by reactions of Na with the IL, since the observed peak potentials in the negative-going scan remain constant even after several cycles. This leads to the assumption that alloy formation took place.

It is known that there are at least three stable alloys between Na and Au: $NaAu_2$, NaAu, and Na_2Au.[140] During the measurements, the potential is constantly varied. Therefore, even more metastable compositions might be possible. Another important aspect is whether the alloy formation is limited to the surface or propagates to the underlying layers. In UHV experiments, where Na was evaporated on a Au(111) surface, it was observed that Na atoms diffuse into deeper layers if many layers are deposited.[159,160] Similar results were obtained for the Na deposition from an organic electrolyte.[221,222] Here, x-ray diffractrograms of a Au film were recorded after bulk Na deposition. These diffractograms showed no evidence of pure Au anymore, but only of the Na_2Au alloy and the underlying Cu substrate.[221,222] At potentials positive of the first two stripping peaks, still, no polycrystalline Au, but a $NaAu_2$ alloy was detected. To provide a detailed comparison of the results, further cycling experiments to lower potentials are needed. This will be shown in 7.1.4.

An alloy formation could not only explain the considerable amount of deposited Na and the dissolution peaks, which appear at much more positive potentials than the deposition peaks. The different dissolution peaks could be explained by the dealloying of Na from differently coordinated sites or alloy compositions.

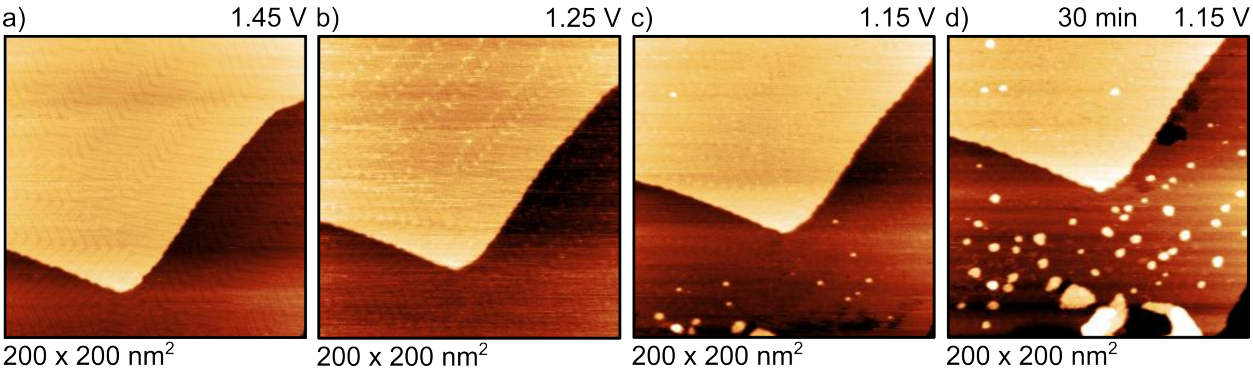

Figure 7.2: *In situ* STM images of the Au(111) surface in 0.2 M Na[TFSI] in [MPPip][TFSI] at a) 1.45 V, b) 1.25 V, c) 1.15 V, and d) after 30 min at 1.15 V. Adapted from Heubach et al. [205]. CC BY-NC-ND 4.0, `https://creativecommons.org/licenses/by-nc-nd/4.0/` Modifications with permission from Wiley.

7.1.2 Initial Stages of Sodium Deposition on Au(111)

In the next step, the morphological changes of the Au(111) surface during the Na UPD were investigated by *in situ* STM. The measurement was started on the electrochemically reconstructed Au(111) surface at 2.55 V. Then, the potential was gradually lowered to 1.45 V, which is slightly positive of the first UPD peak. An STM image of the Au(111) surface at this potential is shown in Figure 7.2 a. The herringbone pattern of the reconstructed Au(111) surface is visible on both imaged terraces. After a decrease of the potential to 1.25 V, which is slightly negative of the UPD peak C1 (see Figure 7.1), a significant change on the surface can be seen which is shown in Figure 7.2 b. Small islands cover the surface at the elbow sites of the herringbone reconstruction. These islands cover every imaged elbow site and at least 2 % of the surface. In the top left quarter of the image, where the elbows and islands are best resolved, a coverage of 6.5 % was determined. The measured height of these islands varies between 50 pm and 100 pm. A more detailed value cannot be extracted from the image. Nevertheless, this value is smaller than the geometric height of a Na deposit on a Au(111) substrate in the case of an epitaxial deposition (269 pm). Therefore, the islands will subsequently be called 'nano-islands'. This observation could originate from different effects. i) The STM image does not necessarily resemble the surface topography but a plane of constant electron density. When Na is deposited on Au, which has a higher electronegativity than Na, Au is expected to withdraw electron density from Na. This would result in a lower measured height of Na deposits due to the chemical contrast. ii) Na is not deposited on top of the topmost

Au layer but, in fact, inserted in this layer. Hereby, even more atoms are in this layer than in the reconstructed Au(111) layer, which already has an atom excess of 4 % compared with the geometric Au(111) plane. This atom excess could increase the layer's height around the inserted Na atom. iii) Simultaneously, Au is dissolved from the surface by cathodic corrosion, as discussed in the last section, and Na is deposited at these pits. Due to the larger size of Na, the first layer and the surface bulge around these sites. However, this mechanism is based on the premise that every elbow site suffers cathodic corrosion. This contradicts the previous findings (see chapter 6).

An STM image after a further decrease of the potential to 1.15 V is shown in Figure 7.2 c, which is in the region of peak C2 (see Figure 7.1). On some of the previously formed nano-islands, islands that exhibit monoatomic height are formed. Compared to the formation of nano-islands, which instantaneously took place at every elbow site, the formation of the islands of monoatomic height is slower. Thus, they only cover some elbows sites and nano-island. Figure 7.2 d shows the Au(111) surface after 30 min at 1.15 V. Even after this time, not every elbow is occupied with an island of monatomic height. Instead, the already deposited islands have grown along the surface and cover now 7.5 % of the surface. The now observed monoatomic height of the islands can be explained differently, depending on the origin of the nano-islands. i) If the nano-islands are, in fact, of monoatomic height but imaged smaller than they are, now, a place exchange between the Na and Au atoms must have taken place. This would increase the electron density in the islands and be the first step in forming a surface alloy between Na and Au. ii)+iii) If the Na was previously inserted into the Au layer or replaced Au atoms, the observed deposition happens on top of the Au layer. Hereby, islands of monoatomic height are formed.

Preferential deposition of metals at the elbow sites of the herringbone reconstruction was already observed for many other metals, e.g. Co,[143,147,148,152] Ni,[142,145,146] Pd,[91,144] Rh,[153] and Mo.[154,155] Hereby, most studies were performed under UHV conditions and only the observations of *Kleinert et al.*[143] and *Möller et al.*[142] were based on *in situ* STM measurements. For UHV conditions, it was supposed that the deposition at the elbow sites could be described as a two-step mechanism.[146] First, an atom of the deposited metal exchanges the place with a Au surface atom. Then, new atoms are deposited, preferably on top of this foreign atom.[146] It is supposed that the atom exchange is the decisive step. Thus, comparing the surface free energy and the sublimation heat of the metal with Au can help predict if another metal, preferably, adsorbs at the elbow sites under UHV conditions.[146] For the electrodeposition, a similar

mechanism is proposed.[142] Preferential deposition on the elbow sites was not observed for the Na deposition under UHV conditions.[159,160] Therefore, the interplay between the Au(111) electrode, the adsorbed Na, and the electrolyte supposedly plays an important role. It is known that the nature of the electrolyte has a strong influence on the potential of the deposition and the preferred nucleation sites.[161] Our results indicate that a different mechanism must be formulated for Na deposition on Au than for the Na deposition under UHV conditions.[159,160] It remains unclear if our observations for the Na deposition agree with the mechanism for the nucleation of foreign metals on the elbow sites proposed in the literature.[142,146] For the Ni electrodeposition, a pit formation on the surface was observed during the first deposition step due to the place exchange between the smaller Ni atoms and Au.[142,146] This might be in agreement with the here observed formation of nano-islands since Na atoms have a radius of 1.8 Å in crystals, which is larger than the respective Au atom radius of 1.35 Å.[223] Also, the preferred deposition of further atoms on top of the foreign atoms at the elbow sites[142,146] agrees with the here observed islands. This mechanism agrees with the third possible explanation for the aforementioned nano-islands, that Na first replaces Au atoms at the elbow sites. This was previously excluded since cathodic corrosion was not observed at all elbows in the pure IL. Nevertheless, in the studies of preferred Ni electrodeposition at the elbow sites, it was reported that no changes at the elbows occured if no Ni salt was added to the electrolyte.[142] Thus, the place exchange might be independent of cathodic corrosion. It also might be possible that further place exchanges between Na and Au occur concomitantly with Na deposition. Alloy formation occurs at room temperature if Na is deposited on Au under UHV conditions and in an electrolyte.[159,160,221,222]

7.1.3 UPD of Na on Au(111)

Figure 7.3 shows a series of STM images recorded during the UPD of Na on Au(111) after the first islands formed at the elbow sites of the herringbone reconstruction. One island is marked in all images with an arrow, which allows for comparison of the structures on the surface at different potentials and deposition times. In Figure 7.3 a, the potential was set to 0.85 V. This image was recorded ca. 90 min after the first islands grew at 1.25 V. The island coverage of the surface, number of islands and average island size in this and the following images are given in Table 7.2. The island nucleation and growth occur quite inhomogeneous. It seems that the deposition is limited to the right part of the images. Most likely, this is related to tip

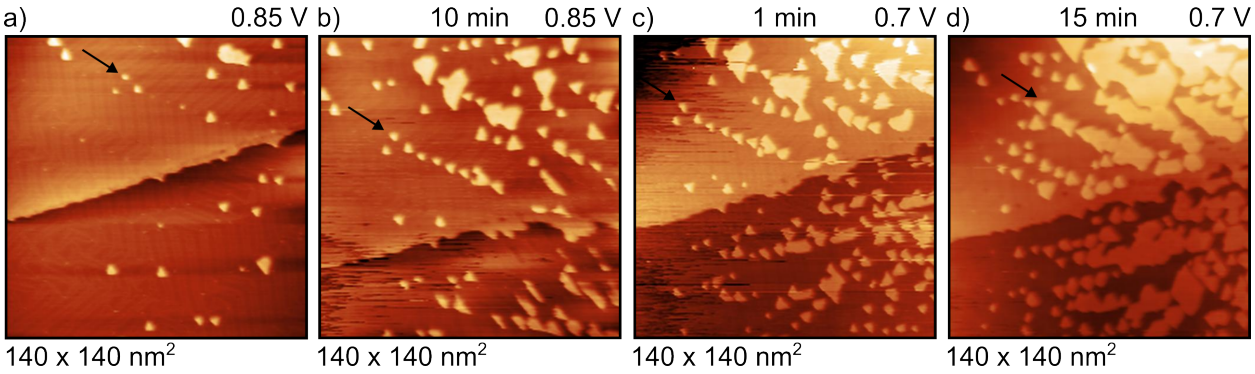

Figure 7.3: *In situ* STM images of the Na UPD on Au(111) in 0.2 M Na[TFSI] in [MPPip][TFSI] a) consecutive to a potential step to 0.85 V, b) after 10 min at 0.85 V, c) 1 min after a potential step to 0.7 V, and d) after 15 min at 0.7 V.

effects that might limit the diffusion in parts of the surface. Due to an irregularly shaped tip or coating, this effect might not influence the entire surface but only parts of the imaged area.

In Figure 7.3 a, most islands have a triangular shape. This means they grow epitaxially to the underlying Au(111) substrate. With this epitaxial growth, two different orientations of step edges would be possible, {111} and {100}. Islands with both types of step edges are typically hexagonal. The triangular shape of the islands suggests that one type of step edge is preferred. Unfortunately, it is impossible to extract from the images which type is preferred. The image in Figure 7.3 b was recorded after 10 min at 0.85 V. Compared to the previous image, it is apparent that the island density increased and the existing islands have grown. The area covered by islands on the surface increased from 3 % to 13 % (see Table 7.2). Figure 7.3 c shows the same region 10 min later just after a potential decrease to –0.7 V. At this time, the island coverage did little increase, while the number of islands increased greatly by the deposition of small islands (see Table 7.2). This is reflected by the average island size, which decreased compared with the previous image even if the deposited islands grew in the respective time. After keeping the potential at 0.7 V for 15 min, the image in Figure 7.3 d was recorded. Many previously deposited islands have coalesced and second layer island growth is observed. The island coverage and average island size increased, while the island number decreased due to coalescence. Whereas the triangular shape of the islands is still present for small islands, the coalesced deposits show a hexagonal shape with both step edge types.

In the STM images in Figure 7.3, most of the deposited triangles have a preferred orientation, with their edges pointing parallel to the reconstruction lines. This means that most of the

Table 7.2: Islands coverage, number and average size for the Na UPD before the multilayer island formation. The time is related to the last change in potential / the change to 0.85 V at which the first image of this series was recorded.

Figure	*E* / V	*t* / min	Island Coverage / %	Island No	Average Island size / nm^2
7.3a	0.85	1	3	28	21
7.3b	0.85	10	13	79	32
7.3c	0.7	1 / 20	15	127	23
7.3d	0.7	15 / 35	38	82	92
7.4a	0.65	3 / 45	51	68	149

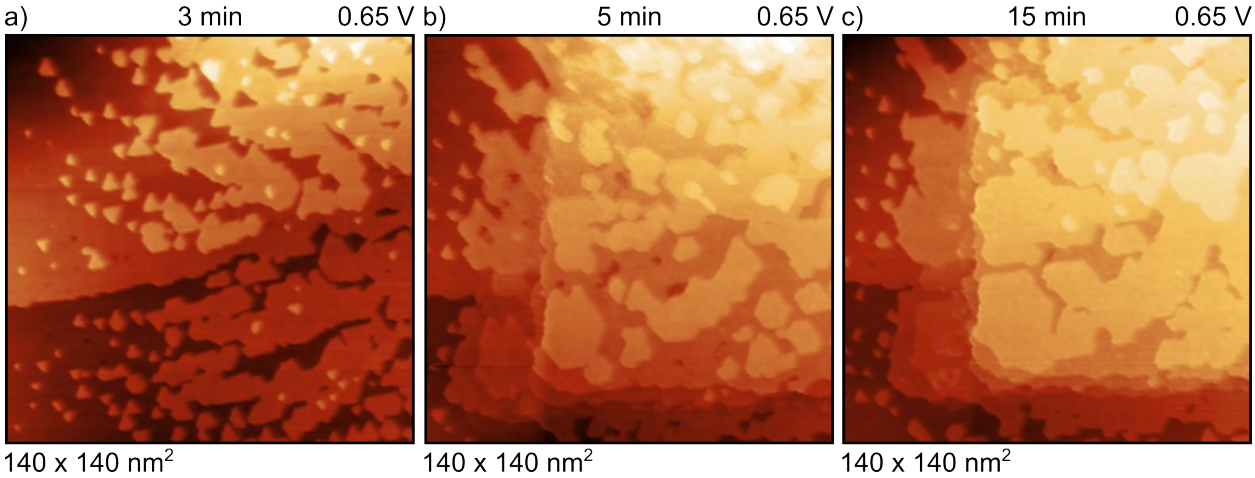

Figure 7.4: *In situ* STM images of the Na UPD on Au(111) in 0.2 M Na[TFSI] in [MPPip][TFSI] at 0.65 V after a) 3 min, b) 5 min, and c) 15 min.

triangular islands pointing with one of their edges to the top of the image have grown on bulged edges, while those with a triangular shape pointing to the bottom of the image have been mostly deposited on the pinched elbows. Ca. 55 % of the islands shown in Figure 7.3 d are deposited on pinched elbows. Therefore, there is no clear trend for a preferential deposition at one type of elbow. Preferential nucleation at one kind of elbow site was *e.g.* reported for Pd electrodeposition.[91] At both elbow types, the islands seem to grow preferably in the hcp region between the reconstruction lines. This is in contrast to the electrodeposition of Co and Pd, where the deposited islands at the bulged elbows grew in the fcc region of the surface.[91,145]

Figure 7.4 gives an overview of the effect of continuous deposition at 0.65 V. The first images recorded at this potential showed ongoing island nucleation and coalescence. Figure 7.4 a was recorded 3 min after the potential decrease to 0.65 V. In the top-right corner of the image, most islands coalesced into a first layer with some holes. Note that the island nucleation and coalescence into layers are still mostly limited to the right-hand side of the imaged area. Nevertheless, half of the imaged area is already covered by the Na islands, and, especially on the right-hand side of the image, second layer deposition occurred. Even in the second layer, islands have a triangular shape, so the growth continues epitaxially. The next image in Figure 7.4 at 0.65 V, recorded only 2 min after the previous image, shows huge changes on the surface compared to the image in Figure 7.4 a. Suddenly, ca. 75 % of the imaged surface is covered by an inhomogeneous multilayer island. This multilayer island exhibits a height of 3-4 monolayers. The islands that form on the topmost layer have either a hexagonal or a triangular structure and are, thus, still epitaxial to the underlying Au(111) substrate. Interestingly, the underlying island shows a rectangular structure, which is not in line with the hexagonal symmetry of the Au(111) substrate. The image in Figure 7.4 c shows the surface 15 min after the potential decrease to −0.65 V. The topmost layer of the multilayer island coalesced to a huge extent, while the underlying layers did not change much. It seems that the borders of the multilayer island remained unchanged as if the lateral growth of the lowest layers of the island was hindered. Interestingly, the underlying Au(111) substrate, which is uncovered, still shows the herringbone pattern of the ($\sqrt{3} \times 22$) reconstruction.

Figure 7.5 shows the surface structure starting 90 min after the multilayer island has formed on the surface. The image in Figure 7.5 a is recorded at 0.65 V which is the same potential than for the images in Figure 7.4. The multilayer island has the same shape as before, but the holes in the topmost layers have filled, and the fourth layer is nearly closed. On the first layer of deposition next to the formed multilayer island, the surface structure is different than on the other parts of the deposit. There are some islands visible, but they are not as distinct as before and seem to be of less than monoatomic height. This might be an indication of deposition, which is not epitaxial. Tip effects are rather improbable since they would also occur on the underlying Au layer. After decreasing the potential to 0.55 V and 135 min after the multilayer island formation started, the image shown in Figure 7.4 b was recorded. The imaged area has shifted to the bottom-left due to thermal drift. On top of the deposited layers next to the multilayer island, irregular three-dimensional structures have formed. This three-dimensional growth continues in Figure 7.5 c, which was recorded at 0.45 V 180 min after the multilayer

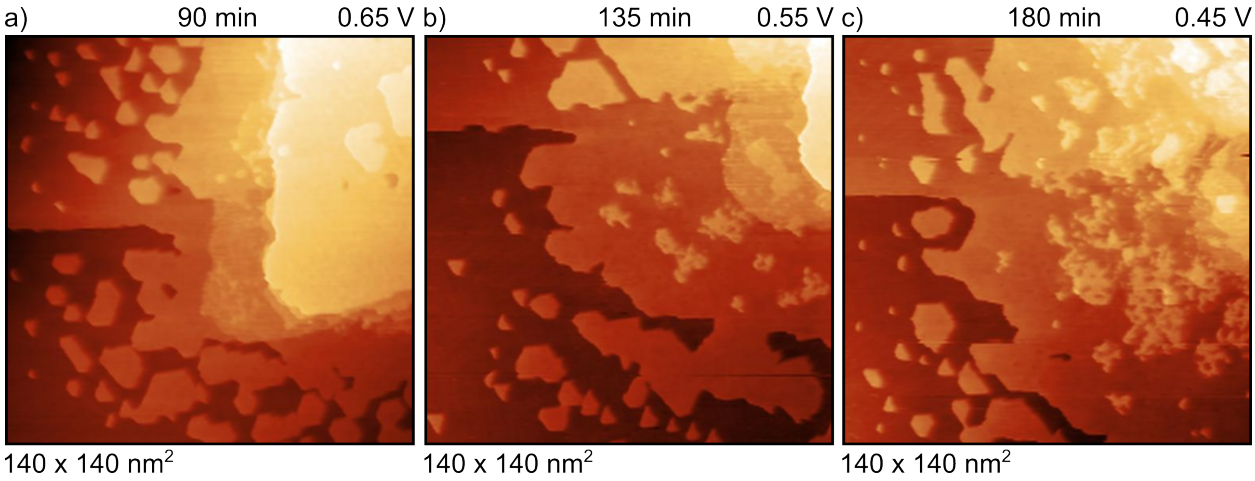

Figure 7.5: *In situ* STM images of the Na UPD on Au(111) in 0.2 M Na[TFSI] in [MPPip][TFSI] a) after 90 min at 0.65 V, b) at 0.55 V 135 min after the start of the multilayer-island formation, and c) at 0.45 V 180 min after the start of the multilayer island formation.

island formation started. The irregular structure now covers the layer next to the multilayer island.

At the end of the measurement, there are still parts of the surface on which no Na nucleation occurred. Still, the amount of Na deposited at potentials positive of the Na/Na^+ equilibrium potential is higher than expected for UPD.[134,136] UPD of four and more monolayers can only be reasoned by a favourable interaction between Na and Au if the Au atoms change positions so that the upper layers are not deposited on pure Na. If Na and Au already form a surface alloy while the first islands are deposited and coalesce into layers, the next deposited layer is not deposited on Na but on a Na-Au alloy. As long as the alloy formation is not limited by the diffusion of Na or Au atoms from/to the bulk crystal, further deposition positive of the Na/Na^+ potential can occur. As discussed above, such diffusion can be expected for Na which is deposited on Au.[221,222]

It is known from Na deposition under UHV conditions that a Na_2Au surface alloy arranges epitaxially with a hexagonal structure on the Au(111) substrate.[160] Under these conditions, a Moiré pattern was observed due to the misfit of the $(1.08\sqrt{3}\times 1.08\sqrt{3})$R30 ° superstructure with the underlying Au surface.[160] Figure 7.6 shows a magnification of the structures of a) the underlying Au(111) substrate in the bottom left region in Figure 7.5 a and b) the deposited multilayer island in the top right region in Figure 7.5 a. The herringbone reconstruction is clearly visible on the admetal-free Au(111) surface. Furthermore, a regular pattern can be

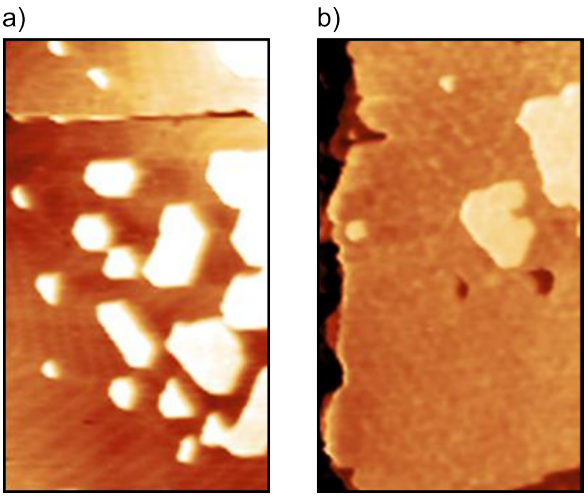

Figure 7.6: Zooms on the STM image in Figure 7.5 a (90 min at 0.65 V) for a detailde view on the structures on top of the surface: a) Herringbone reconstruction on the Au(111) surface underneath the deposited islands in the area of the image where no further deposition took place, b) Structure on top of the deposited multilayer island.

observed on the multilayer island, which could indeed be a Moiré pattern induced by the misfit of a possible Na/Au alloy and the underlying substrate.

The *in situ* STM images have shown that the UPD, which happens in the potential region of the peak C3 in the CVs in Figure 7.1, proceeds in several steps. First, islands form on top of the surface and coalesce. Then, multilayer islands are deposited, which still have clear monoatomic heights between the layers. In the last step, cauliflower-like deposits form on top of the deposited layer. Due to the change from epitaxial growth to an unordered three-dimensional deposition, the growth mode in huge parts of the surface resembles a Stranski-Krastanov-like growth mode. This means that the Na-Au interactions are favourable compared to the Na-Na interactions, which is already clear since UPD happens. A misfit between Na and Au hinders layer-by-layer growth due to sterical strain, leading to cauliflower-like structures during the ongoing deposition. However, Na does not cover the complete surface, which resembles rather a Volmer-Weber-like growth. Otherwise, this growth mode happens if no favourable interactions between the deposited metal and the substrate occur which is in great contrast to the deposition at underpotentials. It is more likely that the uncovered surface is an artefact of the STM measurement.

Interestingly, three different processes (island growth, multilayer growth and spherical growth on top of the deposits) are observed in the potential region of only one peak in the CV (C3).

Nevertheless, this sequence is in accordance with another STM experiment that has been published previously in the frame of this thesis.[205] The origin might be the different conditions of the electrochemical measurements in the glovebox and the *in situ* STM measurements. First, in the CVs, the electrode potential was decreased by a constant scan rate. In contrast, the potential was always kept constant for many minutes in the *in situ* STM measurements. Second, the inert conditions in the glovebox were controlled, while no control was possible in the inert container of the STM. Therefore, higher O_2 and H_2O concentrations in the IL are expected during these measurements, which can affect the deposition.

There are two significant differences in the STM measurement shown here and previously published, which should be briefly discussed.[205] First, in the measurement shown here, some parts of the Au(111) surface were still exposed after the deposition experiment, even at potentials which were lower than those used in the previous work, where the complete imaged area was covered by a multilayer film. Second, the formation of the cauliflower-like structure in the published measurement was different: It already formed at 0.65 V, covering the entire surface with huge spherical particles. Additionally, the process was much faster and already after 45 min at 0.65 V, the deposits did not grow epitaxial anymore. These discrepancies can originate in slight differences in the measurement conditions. One crucial parameter is the stability of the reference electrode. An $AlPO_4$ coated Al wire was used in both measurements. Even if the potentials of the multilayer island, respectively, film deposition, were the same in both measurements, there might be changes in the order of a few millivolts during the measurements, which can influence the deposition process. Another parameter is the tip's and coating's shape. It might be that in the here shown measurement, the tip and coating shield some parts of the surface from Na deposition. Nevertheless, in both measurements, the tips were in good condition since the images were sharp and free of indications of a double tip or images of the tip itself.

7.1.4 Bulk Alloy Formation of Na and Au

In the last step, the focus was moved from the initial stages and the UPD, which could be resolved by STM, to the processes happening at overpotentials and with repetitive cycling. Therefore, a similar window opening experiment as described in Figure 7.1 was repeated for five times. In between these CV series, nine additional cycles with the highest LPL were performed to enable further Na dissolution after the deposition cycles. Figure 7.7 shows the five

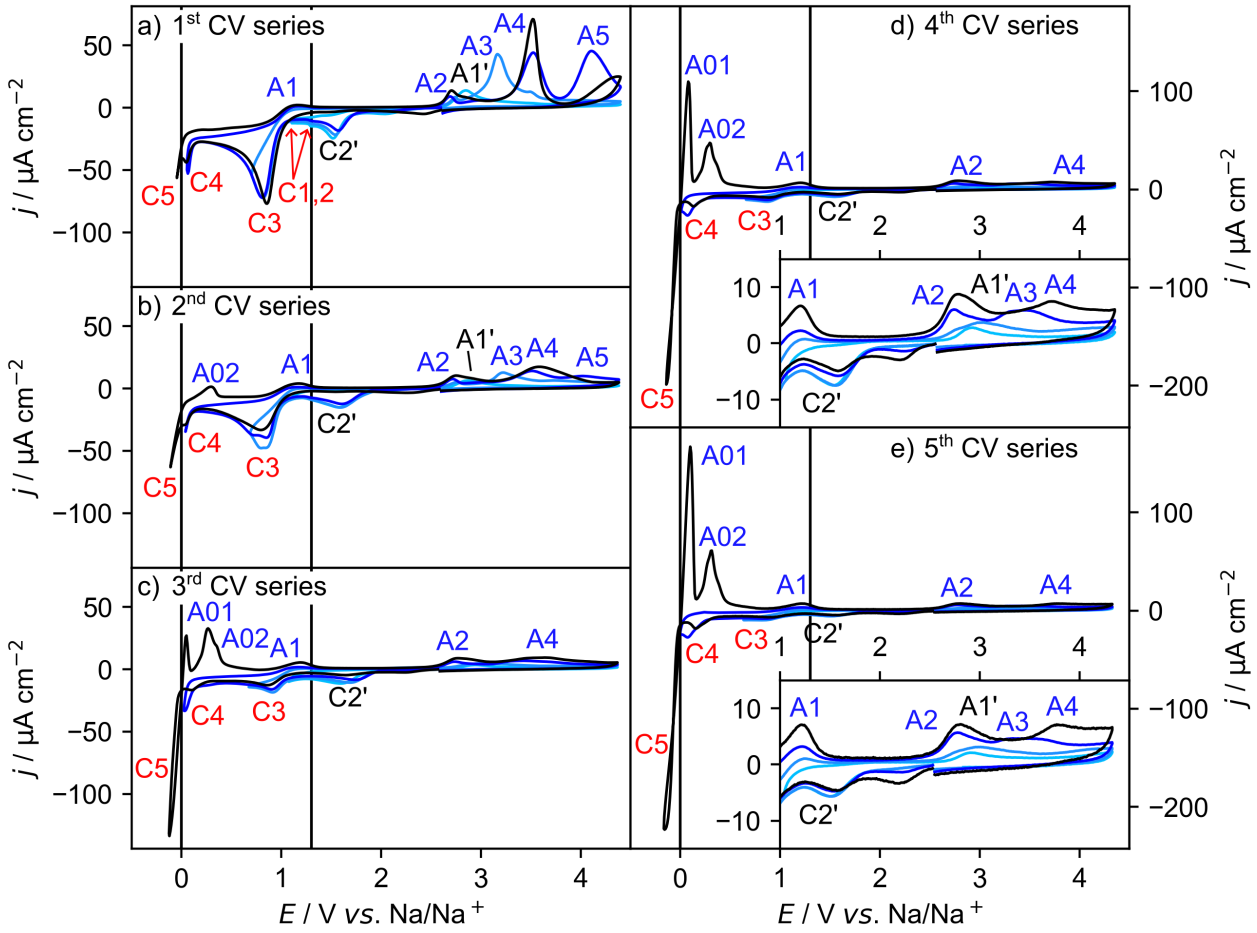

Figure 7.7: Several CV series for Au(111) recorded in a 200 mM solution of Na[TFSI] in the IL [MPPip][TFSI]. The experimental sequence of each series follows the procedure described in 7.1. In between the series, nine additional CVs with the highest LPL were recorded to remove leftovers of Na. The insets in d) and e) show an increased view on the dealloying peaks between 1 V and 4.5 V.

consecutive series of CVs in which the LPL was gradually lowered from ca. 1.25 V, to 1.05 V, 0.65 V, 0.0 V, and –0.1 V in the first series of CVs, respectively –0.15 V in the other. The UPL was always set to 4.35 V and the scan rate was 5 mV s^{-1}. It was observed that the potential of the Na rod, which was used as RE, was not stable throughout the measurement. Thus, all CV series were calibrated on the onset of the OPD peak C5 and its corresponding dissolution peak A01. Due to this, every CV series was conducted with slightly more positive potentials than the previous one. Nevertheless, this shift did not exceed 70 mV from the first to the last series of CVs. The first series of CVs in Figure 7.7 mostly resembles the measurement shown in Figure 7.1. The only difference is the intensity ratio between the anodic peaks A3 to A5. Slight deviations of the potential might be the reason for this. Another possible explanation is that the different peaks could be related to the dealloying processes of Na from sites with different coordination. Here, the crystal roughness before the measurement might play a role. Even if the crystal was always prepared using the same procedure, previous measurements of alloying and dealloying could lead to an increased roughness at the start of the experiment. This might influence the coordination of Na in the alloy and thus lead to differences in the intensities of the different dissolution peaks.

After the first series of CVs, 10 cycles with the highest LPL were performed. In the last cycle, all anodic peaks except the peak A1' have vanished. Therefore, it was expected that the surface had recovered. Nevertheless, there are substantial differences in the second window opening in Figure 7.7 b compared with the first. First, the small peaks C1 and C2, which were only visible as small humps in Figure 7.7 a, are vanished in Figure 7.7 b. Furthermore, all peaks except the peaks C5 and A1 have decreased. Interestingly, the peak C3 now has the shape of a double peak. In the positive-going scan, a new peak A02 with a maximum at ca. 0.25 V appears, and the peak A1 is higher in current density as in the previous series of CVs. These changes in the positive-going scan correlate with the higher current density in the peak C5. This could be reasoned differently. First, there are slight deviations between the potential limits due to the shift of the reference electrode. Second, it might be that not all Na, which was deposited during the series of CVs, has been dissolved. Consequently, more Na is on the surface and forming an alloy with Au than after the OPD in the first series of CVs. This could lead to the formation of alloys with a higher Na content. From these alloys, Na could be oxidised at lower potentials than from alloys with a lower Na content.[221,222] Since the current density of the peaks A02 and A1 is lower than the current density of the other dissolution peaks and the peaks A2 to A5 decreased compared with the first window opening, it is likely

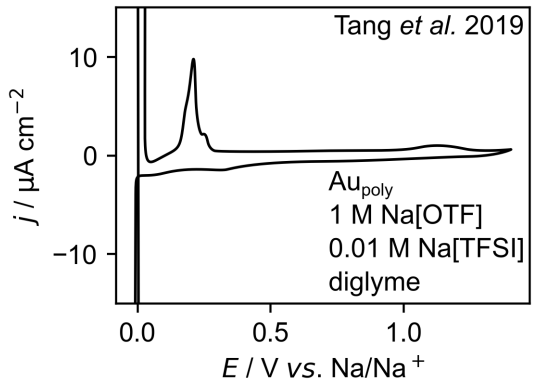

Figure 7.8: CV for polycrystalline Au recorded in diglyme with 1 M Na[OTF] and 0.01 M Na[TFSI] as reported by *Tang et al.*[222] in a two electrode set-up with a Na foil as the counter electrode. No information about the scan speed was given. Due to the small current density, a scan rate of 5 mV s^{-1} or below can be assumed.

that even more Na remains in the Au(111) substrate than before.

The next series of CVs shown in Figure 7.7 c follows the previous trend that the current density of most peaks decreased compared to the previous CV series. All UPD peaks and the peaks A2 to A5 are less intense. In contrast, the OPD peak C5 increased again. Consequently, a second anodic peak A01 at ca. 0.1 V appears, and the peak A02 also increased. Figure 7.7 d and e show the next two CV series. Also, in these series, the current density maximum of the peak C5 increases with each series of measurements, even if the LPLs shifted slightly positively due to the shift of the reference electrode. This leads to a further increase of the anodic peaks A01 and A02. The current density of all other peaks decreased. Nevertheless, they still are there and shown in the insets with an increased current density scale between 1.0 V and 4.5 V.

Tang et al. reported on the Na deposition and alloy formation using a polycrystalline Au substrate and a diglyme electrolyte with 1 M Na[OTF] and 0.01 M Na[TFSI].[221,222] For comparison, the recorded CV is shown in Figure 7.8.[222] All deposition peaks observed in our measurements should appear within the positive and negative potential limit applied by *Tang et al*. Nevertheless, only one huge deposition peak has been recorded, which might be related to the deposition peak C5 observed in Fig 7.7. The following positive-going scan is very similar to our measurements, showing peaks at similar potentials as the peaks A01, A02, and A1 in our measurements (see Figure 7.7). Based on *ex situ* XRD (x-ray diffraction) measurements, the authors suggested that the peak A01 corresponds to the dissolution of metallic Na de-

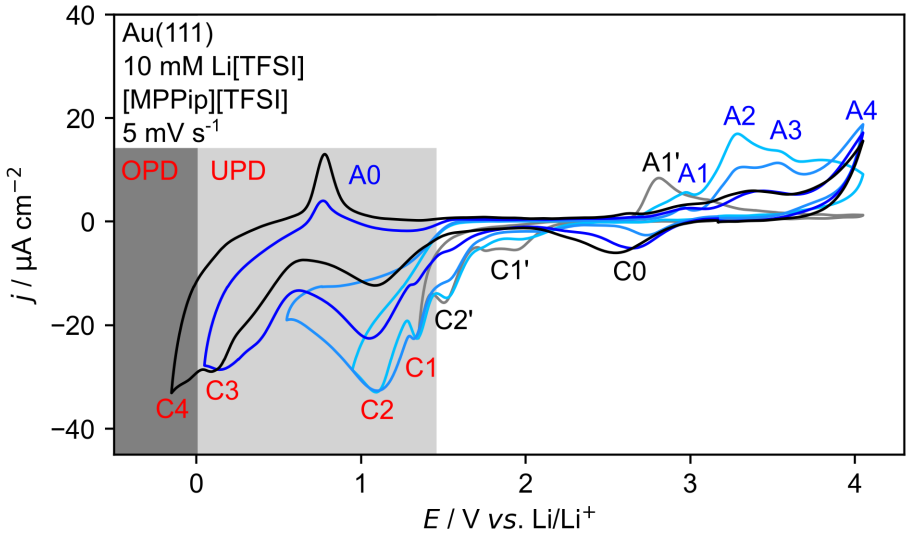

Figure 7.9: CVs for Au(111) recorded in a 10 mM solution of Li[TFSI] in the IL [MPPip][TFSI]. The LPL was gradually decreased while the UPL was kept constant, and the scan rate was 5 mV s^{-1}. All peaks marked in red and blue are assigned to the Li deposition and dissolution with the UPD above and the OPD below 0 V. The black peaks with prime labels are assigned to processes independent of the Na salt (see section 5), and the peak C0 is assigned to surface rearrangements.

posited on top of the Na_2Au alloy. The peak A02 is induced by the dissolution of Na from Na_2Au to form $NaAu_2$ and the peak A1 to the dissolution of the residual Na from the alloy. The measured XRD signals, however, correspond to the bulk of the thin Au sheet used. Thus, it might be that surface alloys are still present at potentials positive of peak A1. These could be dissolved at more positive potentials within the peaks A2-A5.

7.2 Li Deposition on Au(111) from [MPPip][TFSI]

7.2.1 Electrochemical Overview

First reports on Li deposition on Au(111) from [MPPip][TFSI] were performed by *Berger et al.*[31] In their work, the IL showed an electrochemical behaviour of type II in the described measurements. Thus, comparing the data for the Na deposition described above (with type I of IL) might not be trivial. Therefore, another set of measurements was performed to discover

possible differences. Figure 7.10 shows a series of CVs for Au(111) in 10 mM Li[TFSI] in [MPPip][TFSI]. From STM imaging one could, however, not observe Na deposition with such low concentrations. Nevertheless, in the literature, a similarly low concentration was used to image Li depostion from [MPPip][TFSI] by STM. Overall, the CVs shown in Figure 7.9 are rather similar to the measurements with Na. As for Na, the CV contains all peaks known for Au(111) in [MPPip][TFIS] of type I, such as peak C1', C2', and A1' when the potential was not decreased below the peak C1, which is the first peak which was not present in the pure IL. Most of the deposition and dissolution peaks of Li are very similar to the peaks observed for the Na deposition and dissolution. The peak C1 is similar to the peaks C1 and C2 for Na, which were attributed to the initial nucleation of Na at the elbow sites of the herringbone reconstruction. In Li, however, only a single peak is observed. Consequently, we suggest that the peak C2 for Li is related to the peak C3 for the Na-containing IL, which is the main UPD peak. For Li, the charge in the peak C2 is equivalent to ca. 14 monolayers. This is less than for Na but still much more than expected for a UPD peak. Hence, alloy formation is likely to accompany the Li deposition. At potentials below the peak potential of the peak C2, the peaks C3 and C4 follow, which seem similar to the peaks C4 and C5 for the Na deposition. Consequently, it can be assumed that the peak C3 is induced by further alloy formation, whereas the peak C4 is the OPD peak. In the following positive-going scan, the peaks C3 and C4 are followed by the peak A0. Comparing the course of the current density, this peak is similar to that of peak A02 of the Na dissolution attributed to the dealloying of Na_2Au, which is the alloy with the highest Na content. According to a phase diagram of the Au-Li system, the alloy with the highest amount of Li would be $Li_{15}Au_4$.[141] In electrochemical studies. However, the highest observed lithiation of Au was the Li_3Au alloy.[224,225] Therefore, it is likely that the peaks C3 and A0 are related to the formation and dealloying of Li_3Au. In the following positive going scan, several anodic peaks A1 to A4 occur, which only are present if the deposition features have been passed before. They are similar to the peaks A1 to A5 for the Na dissolution and could also correspond to the dealloying from differently coordinated sites. Finally, in the negative-going scan following the dissolution peaks, a huge peak C0 can be observed. This peak was also observed for Na but was not shown in the first cycle since it appeared at slightly different potentials. It likely corresponds to a reordering of the surface after the dealloying.[31]

A comparison to the study of *Berger et al*. about Li deposition on Au(111) from [MPPip][TFSI] shows that there are huge similarities even if the electrochemical behaviour of the pure IL is different. In the measurement of *Berger et al*, the deposition peaks C2, C3 and C4 are also

Table 7.3: Comparison of the standard reduction potentials of Na and Li according to the electrochemical series[14] and the estimated UPD and OPD potentials in [MPPip][TFSI]. Note that the potential value *vs.* Zn/Zn^{2+} is also influenced by the solvent.

Metal	**Na**	**Li**
Standard reduction potential / V *vs.* Zn/Zn^{2+}[14]	-1.95	-2.28
OPD in IL / V *vs.* Zn/Zn^{2+}	-2.4	-2.4
UPD in IL / V *vs.* Zn/Zn^{2+}	-1.1	-0.95
UPD in IL / V *vs.*Na/Na^{+} or Li/Li^{+}	1.3	1.45
UPD according the Kolb-Gerischer rule[14,226] / V *vs.* Na/Na^{+} or Li/Li^{+}	1.5	1.2

visible, even if the peak C4 was not described as an individual Li deposition peak.[31] In the positive-going scan, different dissolution features can also be seen. However, they appeared at various potentials and were differently assigned. One peak in the potential region of the peaks A2 to A4 was assigned to the UPD dissolution, and another at roughly 2 V was assigned to the OPD dissolution.

If the assumptions of the peak attribution between the Na and Li measurements are correct, the UPD of Li begins at less negative potentials than that for Na, whereas the OPD happens at the same potential. This contradicts the predictions of the Galvani series as shown in Table 7.3.[14]

Nevertheless, these predictions do not include the solvation energies of the alkali ions.[198] Since Na^{+} is larger than Li^{+}, it can be coordinated by three $[TFSI]^{-}$ anions, while Li^{+} is only coordinated by two anions.[135] Therefore, the interaction between the Na^{+} ions and the IL might be much stronger than for Li^{+} ions and the IL. Similar effects were already observed in an $AlCl_3$ based IL.[198,199] Interestingly, this was not observed in [BMpyr][TFSI], which contains the same anion than the here used [MPPip][TFSI].[15] This discrepancy cannot easily be explained since there is a lack of data for standard electrode potentials in non-aqueous electrolytes, such as ILs or DESs.[201]

For the *in situ* STM measurements, the Li concentration in the electrolyte was increased to 200 mM to reach comparable conditions as for the Na deposition. Figure 7.10 shows a comparison of the CVs for Au(111) in a solution of of 10 mM and 200 mM Li[TFSI] in [MPPip][TFSI]. Due to changes in the potential of the reference electrode in between the measurements, different potential limits were chosen. Nevertheless, more or less the same peaks can be seen

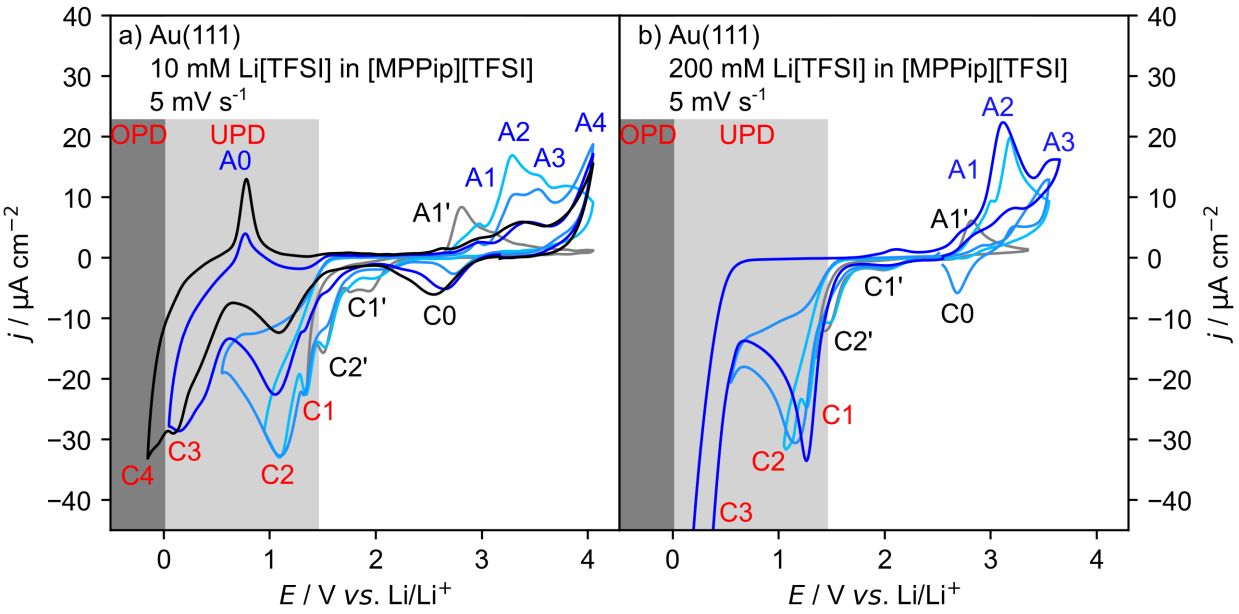

Figure 7.10: CVs for Au(111) recorded in a) a 10 mM and b) a 200 mM solution of Li[TFSI] in the IL [MPPip][TFSI]. The LPL was gradually decreased during both experiments. The peaks marked in red and blue are assigned to the Li deposition and dissolution. The black peaks with prime labels are assigned to processes independent of the Li salt (see chapter 5), and the peak C0 is assigned to surface rearrangements.

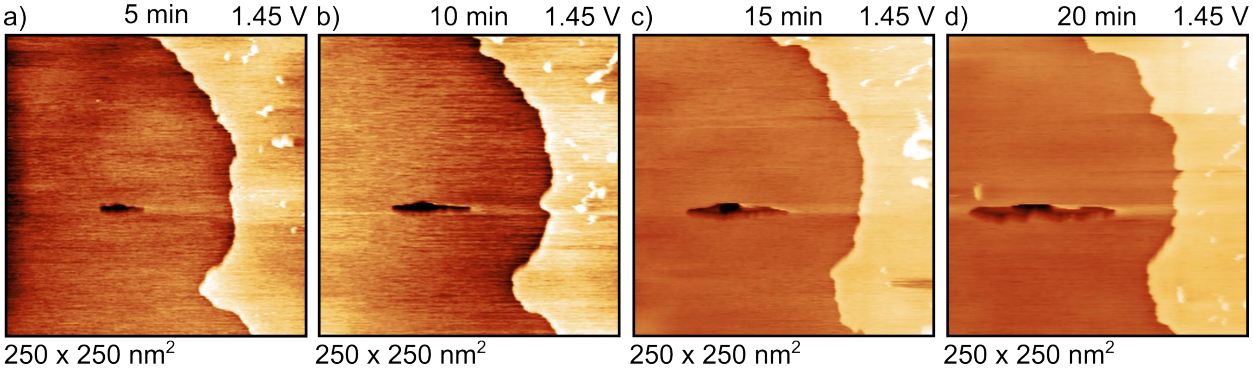

Figure 7.11: *In situ* STM images of the Au(111) surface recorded in 0.2 M Li[TFSI] in [MPPip][TFSI] at a) 5 min, b) 10 min, c) 15 min, and d) 20 min after a potential decrease to 1.45 V. All images were recorded from bottom to top.

for both concentrations. For the 200 mM solution of Li[TFSI], the peak C3 is larger, which can be reasoned by the increased concentration. Furthermore, the peak A0 was not there for the higher concentration. Instead, the current density dropped to 0 µA cm^{-2} in the positive-going scan between 0.5 V and 1.5 V after the peak C3 was passed in the previous negative-going scan. In the measurement with the lower concentration, the current density has a negative offset in this potential region. Overall, comparable processes can be observed for both concentrations, so changing the concentration to higher values for the *in situ* STM measurements is reasonable.

7.2.2 Underpotential Deposition of Li on Au(111)

Berger et al. described an island formation of Li during the UPD in the peak C2.[31] These islands coalesced with time.[31]

Figure 7.11 shows a series of *in situ* STM images of Au(111) recorded in the 200 mM solution of Li[TFSI] in [MPPip][TFSI] at 1.45 V. All images were recorded from bottom to top. Figure 7.11 a was recorded 5 min after the potential was decreased to 1.45 V. A monoatomic high step separates two terraces. On the upper terrace, the first irregularly-shaped monolayer high islands formed. The next images shown in Figure 7.11 b, c, and d were recorded 10 min, 15 min, and 20 min after the potential decrease. In all of these images, some islands are present, mostly on the upper terrace, but the islands are very mobile and change positions and shapes in between the images. Also, the Au(111) surface shows high mobility and

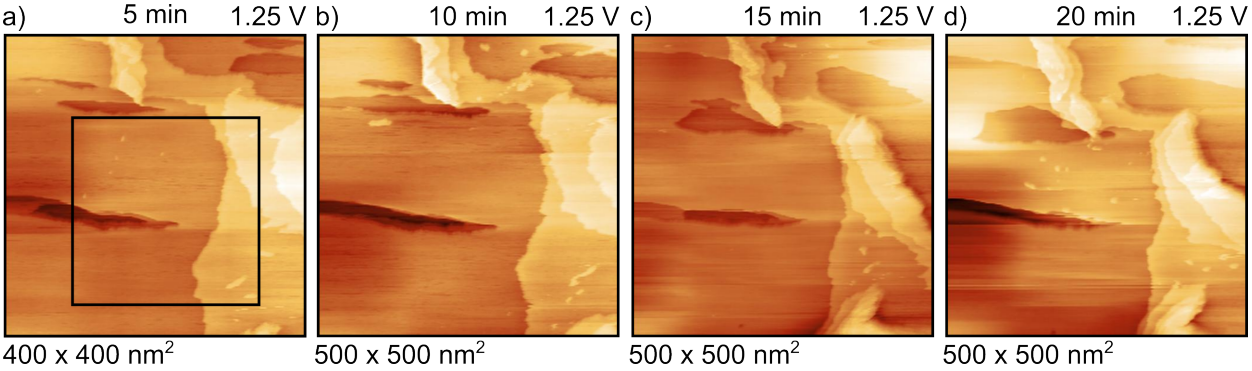

Figure 7.12: *In situ* STM images of the Au(111) surface recorded in 0.2 M Li[TFSI] in [MPPip][TFSI] at a) 5 min, b) 10 min, c) 15 min, and d) 20 min after a potential decrease to 1.25 V. All images were recorded from bottom to top.

restructures during the measurement. The shape of the step edge changes from image to image, as well as the monolayer deep hole on the lower terrace increases. Therefore, it is not easy to determine if the deposited islands are, in fact, Li islands or dissolved Au. Since no islands were observed at similar potentials in the pure IL, it is reasonable to assume that the observed islands are related to the deposition of Li. Therefore, it can be assumed that Li is deposited, but this deposition goes in hand with increased mobility of the Au atoms.

Figure 7.12 shows some images of the continued measurement after a potential decrease to 1.25 V. All images were recorded from bottom to top. A larger area was imaged than in Figure 7.11, which is shown with the black frame in Figure 7.12 a. This image was recorded 5 min after the potential decrease. Due to the larger area, more terraces become visible, and more holes in the lower terrace can be seen in the top part of the image. Additionally, there are some islands on the terraces. The hole, already observed during the previous images, now has a depth of two monolayers. The following images shown in Figure 7.12 b, c, and d were recorded 10 min, 15 min, and 20 min after the potential decrease. The surface atoms remain mobile during this time, and the step edges, holes and islands rearrange. Hereby, the holes and islands grow, the terrace widths become smaller, and ridges form.

Figure 7.13 a) shows the same region with a large scale image 15 min after the potential was decreased to 0.75 V. The surface is covered with huge holes and multilayer ridges. Still, it remains unclear which surface regions are covered by Li or bare Au. The enhanced surface mobility during the deposition and comparison to the Na deposition leads to the assumption that here, as well, an alloy is formed during the deposition. This assumption is strengthened by

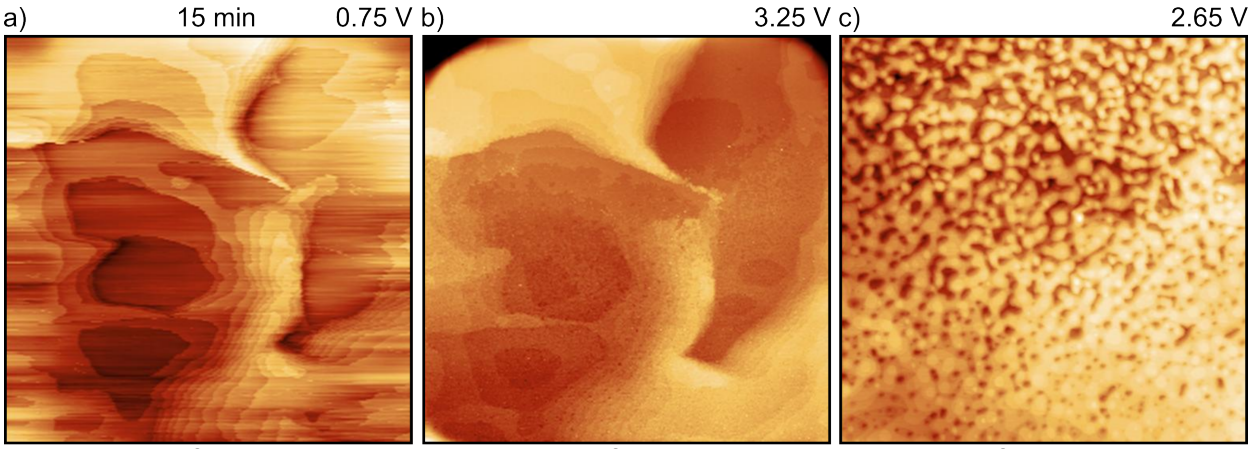

Figure 7.13: *In situ* STM images of the Au(111) surface recorded in 0.2 M Li[TFSI] in [MPPip][TFSI] a) 5 min after a potential decrease to 0.75 V, b) subsequently, after increasing the potential to 3.25 V, and c) at 2.65 V after one cycle of Li UPD and dissolution.

the observations made after increasing the potential again to potentials where the dissolution of Li is expected: Figure 7.13 b shows the surface after a potential increase to 3.25 V. The image was recorded from top to bottom and the potential was increased immediately before recording this image. Whereas the surface is relatively stable in the top part of the image, many tiny holes appear, scanning from top to bottom. It seems that some material is dissolved from the surface. This dissolution continues, and Figure 7.13 c shows the surface at 2.65 V after Li was first deposited at 0.75 V and then dissolved at 3.25 V. Now, the surface is very rough, with a porous structure. This is quite common after dealloying[227–229] and even observed after Li dissolution from Au,[32] so it can be assumed that Li had been deposited before.

7.2.3 Comparison of Na and Li Deposition

Some parts of this section have previously been published in the article "Initial Stages of Sodium Deposition onto Au(111) from [MPPip][TFSI]: An In-Situ STM Study for Sodium-Ion Battery Electrolytes".[205]

The electrochemical measurements have shown that Na and Li deposition show very similar peaks in the CVs if the same IL with the same type of electrochemical behaviour is used. In both cases, there are many different UPD peaks and dissolution peaks. The UPD peaks cover

over 10 monolayer charge equivalents of current density. The huge amount of deposited material during the UPD can be explained by alloy formation, which was also observed in other studies where Na and Li were deposited on Au from other electrolytes or in vacuum.[32,159,160,221,222] Furthermore, it is known that several alloys of the alkali metals with Au are stable.[140,141] This can also explain the many dissolution peaks observed. In contrast, the *in situ* STM measurements reveal the differences in the deposition of both alkali metals. For Na, the UPD started at the elbow sites of the reconstruction pattern, and the islands grew from these sites. The surface was morphologically very stable throughout the whole measurement. In contrast, Li islands seemed rather mobile. The Au(111) surface also greatly changed during the Li deposition by forming pits and the step edges were also rather mobile. These differences also resulted in different macroscopic structures after the UPD. For Na, huge multilayer islands covered the surface, which were, in the end, partially covered with a cauliflower-like structure, while during Li deposition, ridges were formed. Nevertheless, after the dissolution of both alkali metals, the surface was very rough with many pits and islands as expected after dealloying processes.[32,227–229]

8 Summary and Outlook

In this work, I presented fundamental insights into the electrochemical processes in the IL [MPPip][TFSI] in contact with a Au(111) electrode: The electrochemical behaviour was elucidated by cyclic voltammetry. Furthermore, morphological changes of the Au(111) electrode within the electrochemical stability window of the IL were resolved by *in situ* STM. Finally, the Na and Li electrodeposition and dissolution were investigated by cyclic voltammetry, and the initial stages of the UPD were resolved by *in situ* STM.

It could be shown that all batches of this IL that we purchased during this thesis could be categorised into two distinct electrochemical behaviours. Most of the peaks observed in the CVs could be related to reactions of either residual H_2O or O_2, even if all measurements were performed under an inert atmosphere. To study the influence of water, we changed the concentration either by adding water or by removing it. However, changes in the H_2O content did not result in considerable changes in the peaks in the CVs. This was attributed to the accumulation of H_2O at the IL-Au(111) interface at low concentrations, which does not increase significantly when the bulk H_2O content is increased. Therefore, neither vacuum-drying nor adding a molecular sieve significantly affected the water-related peaks. However, the treatment with the molecular sieve results in Na impurities, which most likely originate in a place exchange between Na ions from the zeolite and the cations of the IL. Consequently, the peaks known for the Na deposition from this IL could be observed in the CVs of the molecular sieve-dried IL. Additional XPS measurements could verify that Na is present in the molecular sieve-dried IL and can be deposited from it. Still, it could not be determined if type I or type II of the electrochemical behaviour of the IL is induced by impurities that are not present in the other type of batch. Therefore, it might be helpful to mix the batches to see which behaviour dominates over the other. Other insights could be gained by measuring in an O_2 or CO_2 atmosphere to get a better understanding of the influence of these gases, which can hardly be monitored in the electrolyte.

Even if Au is considered to be a mostly inert electrode,[56–58] it was shown that this considers

chemical and electrochemical reactions, while its morphology undergoes many restructuring processes within the electrochemical stability window of the IL. On Au(111), the Au oxidation starts at ca. 2.0 V *vs.* Zn/Zn[TFSI]$_2$. The reduction was observed at different potentials(–0.7 V or –1.2 V), where the potential depends on either the water content or surface preparation. Hence, the electrochemical stability window of a Au(111) electrode in [MPPip][TFSI] is ca. 2.5–3 V. The onset of the cathodic corrosion starts with a pit formation, preferably at the elbow sites of the herringbone reconstruction. Hereby, the water content plays an important role. The higher the water content is, the more elbow sites are affected by pit corrosion. Redeposition of the dissolved material was not observed in the measurement but cannot be excluded since it might have happened outside the imaged area of the surface.

Even within the electrochemical stability window of the Au(111) electrode, there are some morphological changes. At 0.4 V, the herringbone reconstruction of the Au(111) surface is lifted, probably due to OH^--adsorption. The islands formed during the lifting of the reconstruction were rather small and nucleated along the reconstruction lines. The formation of small islands indicates that the surface mobility was very low at the respective potential. In other electrolytes, large variations of the surface morphology depending on the potential at which the reconstruction was formed or lifted on the formed structures were seen.[89,93] Further insights into the potential-dependent surface mobility could be gained by additional studies varying the potential of the formation and lifting of the reconstruction. With increased O_2 contents the morphology of the Au(111) surface changed drastically between –0.7 V and –0.3 V. The step edges rearranged forming channels and fingers which resulted in an increased share of {111} step edges. Furthermore, large deviations in the measured step height due to electrochemical reactions on the tip were observed. Possibly, the ORR induces these effects. To avoid such effects, *in situ* AFM measurements could be conducted.

For the Na deposition on Au(111) from [MPPip][TFSI], several stages of UPD were found. The UPD starts at 1.3 V *vs.* Na/Na^+ (–1.1 V *vs.* Zn/Zn[TFSI]$_2$) with Na nucleation at the elbow sites of the herringbone reconstruction. After decreasing the potential, these islands grew and started coalescing. Once islands have been formed, they remain in the place where they were formed. Multilayer islands start covering the surface at 0.65 V. First, these multilayer islands or films show clear monoatomic steps. During the following UPD, the three-dimensional Na growth continues in a less-defined cauliflower-like structure. This mechanism resembles mostly a Stranski Krastanov-like growth mode. The deposition of three-dimensional multilayer islands during the UPD is only reasonable if alloy formation between Na and Au occurs con-

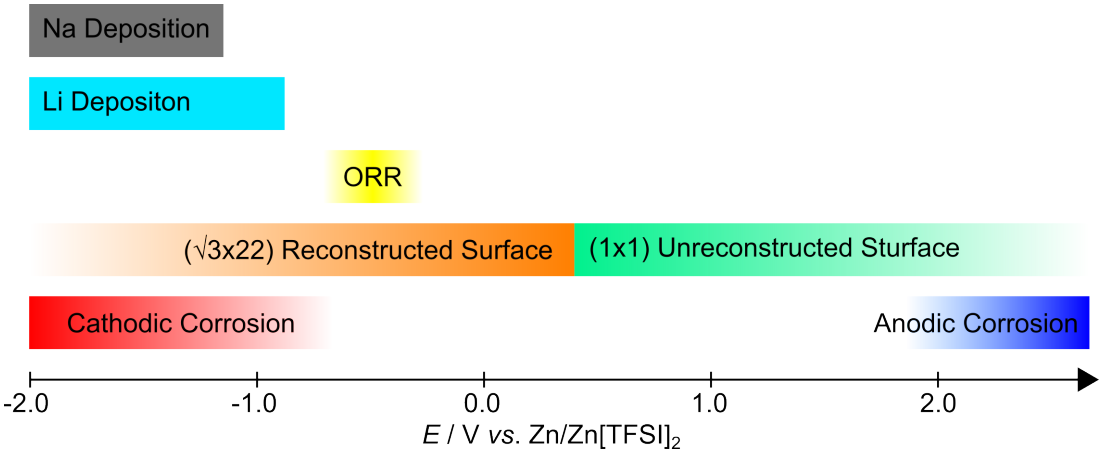

Figure 8.1: Overview on the potentials of Na and Li deposition on Au(111) and the surface restructuring processes of Au(111) in [MPPip][TFSI].

comitantly with the Na deposition.

The OPD of Na started at ca. –2.4 V *vs.* Zn/Zn[TFSI]$_2$. As observed for Na deposition on a polycrystalline Au sample,[221,222], reversible plating and stripping of Na is only possible after forming a NaAu-alloy. This can be reasoned by the deliberate alloy formation, which prevents the dissolution of Na at low overpotentials as long as the deposited Na can form an alloy with the Au substrate.

The CVs for Au(111) in the Li-containing electrolyte are very similar to the respective CVs in the Na-containing electrolyte. Hereby, the Li UPD started slightly positive of the Na UPD at 1.45 V *vs.* Li/Li$^+$ (–0.95 V *vs.* Zn/Zn[TFSI]$_2$). Interestingly, the Li OPD started at the same potential as the Na OPD (–2.4 V *vs.* Zn/Zn[TFSI]$_2$). This is not expected from the standard reduction potentials for both metals.[14] Nevertheless, similar findings were made in an $AlCl_3$-based IL.[198,199] Furthermore, Na is better coordinated by the [TFSI]$^-$-anions than Li.[135] Therefore, the solvation energy might be larger for Na and, thus, the deposition is shifted to lower potentials than expected. In contrast to the Na deposition, the surface mobility of Li on Au(111) in the Li-containing electrolyte was very high. This included the formed Li islands and the underlying Au(111) substrate. During the UPD, ridges formed, which most probably consist of Li/Au alloys since Li and Au also deliberately form alloys.[141]

In summary, Figure 8.1 shows all processes in the pure IL and the IL with a Na or Li salt with the respective potential ranges. Na and Li are deposited at potentials at which the cathodic corrosion started. Nevertheless, pit formation, such as in the pure IL, was not observed. The

surface seems to be more stabilised with Na such that no pit formation in the presence of the Na salt was observed. In contrast, the surface mobility is much higher in the presence of Li salt.

The shown measurements for the Na and Li deposition have revealed valuable insights into the Li and Na deposition on Au and the consecutive alloy formation. These insights could help to also gain a better understanding of other alloying electrodes, such as Si and Sn which can be used for LIBs.[230,231] However, it would still be interesting to see how the morphology of the Li and Na deposits evolves if a non-alloying material is used. Rh(111) would be a possible substrate since it has the same crystal structure as Au(111) but neither forms alloys with alkali metals nor reconstructs at negative potentials. Furthermore, *in situ* AFM measurements of the initial nucleation of Na on Au(111), which depict the height and not the electron density of the surface, would be interesting. They could reveal if the nano-islands have a smaller height than expected for an island of monoatomic height or are of monoatomic height.

In this thesis, many details about the electrochemistry of [MPPip][TFSI] with and without alkali salts on Au(111) and the proceedings at the [MPPip][TFSI]-Au(111) interface could be revealed. Despite that, several pitfalls in such investigations could be identified. It was shown that reproducibility in ILs is difficult due to unknown impurities in the purchased chemicals. This aspect is not only relevant for ionic liquids, but as well for other non-aqueous electrolytes which do not have clear benchmarks. Furthermore, the Au(111) surface showed massive morphologic changes throughout the measurements, even if it is often described as an inert electrode.[56–58] The measurements of the Na and Li deposition showed very similar CVs, which could lead to the assumption that the deposition and dissolution of both alkali metals occur very similar. Nevertheless, *in situ* STM revealed that the morphologies of the deposits and the surface mobility during the UPD were very different. This shows the value of *in situ* scanning probe methods which allow the observation of processes which would be overseen in pure electrochemical measurements.

A Appendix

Table A.1: Overview on all batches and preparations.

Figure	Company, batch	Preparation	Additives	Water content / ppm
5.1 a	Iolitec, batch 1	vacuum-dried	none	<25
5.1 b	Iolitec, batch 2	vacuum-dried	none	<5
5.1 c	Iolitec, batch 3	none	none	<75
5.1 d	Solvionic, batch 4	none	none	<10
5.1 e	Iolitec, batch 5	none	none	<100
5.2 black	Iolitec, batch 1	vacuum-dried	none	<25
5.2 blue	Iolitec, batch 2	vacuum-dried	none	<5
5.2 grey	Iolitec, batch 3	none	none	<75
5.2 green	Solvionic, batch 4	none	none	<10
5.2 red	Iolitec, batch 5	none	none	<100
5.3 a	Iolitec, batch 3	none	none	<75
5.3 b	Solvionic, batch 4	none	none	<10
5.4 a	Iolitec, batch 3	none	none	<75
5.4 b	Iolitec, batch 3	none	none	<75
5.4 c	Solvionic, batch 4	none	none	<10
5.4 d	Solvionic, batch 4	none	none	<10
5.5 a solid	Iolitec, batch 3	vacuum-dried	none	<50
5.5 a dashed	Iolitec, batch 3	none	none	<75
5.5 b solid	Iolitec, batch 3	molecular sieve-dried	none	<5
5.5 b dashed	Iolitec, batch 3	none	none	<75
5.6 solid	Iolitec, batch 3	molecular sieve-dried	none	<5
5.6 dashed	Iolitec, batch 3	none	none	<75
5.7 a solid	Solvionic, batch 4	molecular sieve-dried	none	<5
5.7 a dashed	Solvionic, batch 4	none	none	<10
5.7 b solid	Iolitec, batch 5	molecular sieve-dried	none	not determined
5.7 b dashed	Iolitec, batch 5	none	none	<100
5.8 blue	Iolitec, batch 5	molecular sieve-dried	none	not determined
5.8 black	Iolitec, batch 5	none	none	<100
5.9 a solid	Iolitec, batch 2	none	water	290
5.9 a dashed	Iolitec, batch 2	vacuum-dried	none	<5
5.9 b solid	Iolitec, batch 3	none	water	270
5.9 b dashed	Iolitec, batch 3	none	none	<75
5.9 c solid	Solvionic, batch 4	none	water	170
5.9 c dashed	Solvionic, batch 4	none	none	<10
5.10 solid	Iolitec, batch 3	none	water	450
5.10 dashed	Iolitec, batch 3	none	none	<75
5.11 solid	Iolitec, batch 3	none	H[TFSI]	not determined
5.11 dashed	Iolitec, batch 3	none	none	<75

Table A.2: Overview on all batches and preparations (continued).

Figure	Company, batch	Preparation	Additives	Water content / ppm
6.1 red	Iolitec, batch 1	vacuum-dried	none	not determined
6.1 blue	Iolitec, batch 1	vacuum-dried	none	not determined
6.2	Iolitec, batch 1	vacuum-dried	none	not determined
6.3	Iolitec, batch 1	vacuum-dried	none	not determined
6.4	Iolitec, batch 1	vacuum-dried	none	not determined
6.5	Iolitec, batch 3	none	none	<75
6.6	Iolitec, batch 3	none	none	<75
6.7	Iolitec, batch 1	none	water	200
6.10	Iolitec, batch 3	none	none	<75
6.11	Iolitec, batch 3	none	none	<75
6.12	Iolitec, batch 3	none	none	<75
6.13	Iolitec, batch 3	none	none	<75
7.1	Iolitec, batch 1	vacuum-dried	Na[TFSI]	not determined
7.2	Iolitec, batch 1	vacuum-dried	Na[TFSI]	not determined
7.3	Iolitec, batch 3	vacuum-dried	Na[TFSI]	not determined
7.4	Iolitec, batch 3	vacuum-dried	Na[TFSI]	not determined
7.5	Iolitec, batch 3	vacuum-dried	Na[TFSI]	not determined
7.6	Iolitec, batch 3	vacuum-dried	Na[TFSI]	not determined
7.7	Iolitec, batch 3	vacuum-dried	Na[TFSI]	not determined
7.9	Iolitec, batch 3	vacuum-dried	Li[TFSI]	not determined
7.10	Iolitec, batch 3	vacuum-dried	Li[TFSI]	not determined
7.11	Iolitec, batch 3	vacuum-dried	Li[TFSI]	not determined
7.12	Iolitec, batch 3	vacuum-dried	Li[TFSI]	not determined
7.13	Iolitec, batch 3	vacuum-dried	Li[TFSI]	not determined

Table A.3: Parameters of the STM images 1. All potentials are given *vs.* Zn/Zn[TFSI]$_2$.

Image	E_{WE} / V	E_T / V	I_T / nA	I-gain	P-gain	v / Hz	↓↑	feedback mode
2.3	1.75	1.95	1	5	2.5	1	↑	lin
6.7 a	0	0.1	1	2	1	1	↓	lin
6.7 b	-0.7	-0.6	1	2	1	1	↓	lin
6.7 c	-0.7	-0.6	1	2	1	1	↓	lin
6.7 d	-0.7	-0.6	0.7	2	1	2.08	↓	lin
6.2 a	-1.4	-0.2	1			3	↓	log
6.2 b	1.3 → 2.5 → 1.3	0.19	1			4	↓	log
6.5 a	-0.5 → -0.6	0.2	1	0.733	3.53	1	↑	log
6.5 b	-0.7	0.2 → 0.1	1	0.733	3.53	1	↑	log
6.5 c	-0.7	0.1	1	0.733	3.53	1	↑	log
6.6 a	-0.7	0.1	1	0.733	3.53	1	↑	log
6.10 a	-1	-0.2	1	0.733	3.53	1	↓	log
6.10 b	0 → 0.5	-0.2 → 0.3	1	0.733	3.53	1	↓	log
6.11 a	-0.7	-0.3	1	0.733	3.53	1	↓	log
6.11 b	-0.6	-0.3	1	0.733	3.53	1	↓	log
6.11 c	-0.6	-0.3	1	0.733	3.53	1	↓	log
6.11 d	-0.6	-0.3	1	0.733	3.53	1	↓	log
6.12 a	-0.5	-0.3	1	0.733	3.53	1	↓	log
6.12 b	-0.5	-0.3	1	0.733	3.53	1	↓	log
6.12 c	-0.5	-0.3	1	0.733	3.53	1	↓	log
6.13 a	-0.5 → -0.4	-0.3	1	0.733	3.53	1	↑	log
6.13 b	-0.4	-0.3	1	0.733	3.53	1	↓	log
6.13 c	-0.4	-0.3	1	0.733	3.53	1	↑	log
6.13 d	-0.4	-0.3	1	0.733	3.53	1	↓	log
6.3 a	-0.9	-0.8	1	2	1	1	↓	lin
6.3 b	-1.2	-0.8	1	2	1	1	↓	lin
6.3 c	-1.5	-0.8	1	2	1	1	↓	lin
6.4 a	-1.8	-0.8	1	2	1	1	↓	lin

Table A.4: Parameters of the STM images 2. All potentials are given *vs.* Na/Na^+ (7.2-7.5) or Li/Li^+ (7.11-7.13).

Image	E_{WE} / V	E_T / V	I_T / nA	I-gain	P-gain	v / Hz	↓↑	feedback mode
7.2 a	1.45	1.85	1	2	1	1	↓	lin
7.2 b	1.25	1.85	1	2	1	1	↓	lin
7.2 c	1.15	1.85	1	2	1	1	↓	lin
7.2 d	1.15	1.85	1	2	1	1	↓	lin
7.3 a	0.85	1.95	1.5	5	2.5	2	↑	lin
7.3 b	0.85	1.95	1.5	5	2.5	2	↓	lin
7.3 c	$0.75 \rightarrow 0.7$	1.95	1.5	5	2.5	2	↑	lin
7.3 d	0.7	1.95	1.5	5	2.5	2	↓	lin
7.4 a	0.65	1.95	1.5	5	2.5	2	↑	lin
7.4 b	0.65	1.95	1.5	5	2.5	2	↓	lin
7.4 c	0.65	1.95	1.5	5	2.5	2	↑	lin
7.5 a	0.65	1.95	1.5	5	2.5	2	↑	lin
7.5 b	0.55	1.95	1.5	5	2.5	2	↑	lin
7.5 c	0.45	1.95	1.5	5	2.5	2	↑	lin
7.11 a	1.45	2.35	1	1	100	2	↑	log
7.11 b	1.45	2.35	1	1	100	2	↑	log
7.11 c	1.45	2.35	1	1	100	2	↑	log
7.11 d	1.45	2.35	1	1	100	2	↑	log
7.12 a	1.25	2.35	1	1	100	2	↑	log
7.12 b	1.25	2.35	1	1	100	2	↑	log
7.12 c	1.25	2.35	1	1	100	2	↑	log
7.12 d	1.25	2.35	1	1	100	2	↑	log
7.13 a	0.75	2.35	1	1	100	2	↑	log
7.13 b	$2.65 \rightarrow 3.081$	2.35	1	1	100	2	↑	log
7.13 c	2.65	2.35	1	1	100	2	↓	log

Table A.5: Step heights in Figures 6.5, 6.6, 6.11,6.12, and 6.13 and the corresponding potential.

Figure	***E*** **/ V *vs.* Zn/Zn[$TFSI_2$]**	**Step height / pm**
6.5 a	-0.6	236±30
6.5 b	-0.7	233±30
6.5 c	-0.7	232±30
6.6 a	-0.7	243±30
6.11 a	-0.7	260±30
6.11 b	-0.6	550±60
6.11 c	-0.6	1280±130
6.11 d	-0.6	1270±130
6.12 a	-0.5	1150±120
6.12 b	-0.5	1120±120
6.12 c	-0.5	1140±120
6.13 a	-0.4	1270±130
6.13 b	-0.4	920±100
6.13 c	-0.4	1100±120
6.13 d	-0.4	984±100

Bibliography

[1] T. Yu, G. Li, Y. Duan, Y. Wu, T. Zhang, X. Zhao, M. Luo, Y. Liu, *Journal of Alloys and Compounds* **2023**, *958*, 170486.

[2] M. R. Palacín, *Chemical Society Reviews* **2009**, *38*, 2565–2575.

[3] J. F. Parker, C. N. Chervin, I. R. Pala, M. Machler, M. F. Burz, J. W. Long, D. R. Rolison, *Science* **2017**, *356*, 415–418.

[4] A. Sivakumaran, A. J. Samson, V. Thangadurai, *Energy Technology* **2023**, *11*, 2201323.

[5] A. K. Prajapati, A. Bhatnagar, *Journal of Energy Chemistry* **2023**, *83*, 509–540.

[6] N. Zhu, K. Zhang, F. Wu, Y. Bai, C. Wu, *Energy Material Advances* **2021**, *2021*, 1–29.

[7] S. Daboss, F. Rahmanian, H. S. Stein, C. Kranz, *Electrochemical Science Advances* **2022**, *2*, e2100122.

[8] S. A. M. Noor, P. C. Howlett, D. R. MacFarlane, M. Forsyth, *Electrochimica Acta* **2013**, *114*, 766–771.

[9] C. Ding, T. Nohira, A. Fukunaga, R. Hagiwara, *Electrochemistry* **2015**, *83*, 91–94.

[10] K. Sirengo, A. Babu, B. Brennan, S. C. Pillai, *Journal of Energy Chemistry* **2023**, *81*, 321–338.

[11] Y. Li, Y. Lu, P. Adelhelm, M.-M. Titirici, Y.-S. Hu, *Chemical Society Reviews* **2019**, *48*, 4655–4687.

[12] H. Pan, Y.-S. Hu, L. Chen, *Energy & Environmental Science* **2013**, *6*, 2338.

[13] N. Yabuuchi, K. Kubota, M. Dahbi, S. Komaba, *Chemical Reviews* **2014**, *114*, 11636–11682.

[14] D. Lide, *CRC Handbook of Chemistry and Physics, 82nd Edition*, Taylor & Francis, **2001**.

[15] R. Wibowo, L. Aldous, S. E. W. Jones, R. G. Compton, *Chemical Physics Letters* **2010**, *492*, 276–280.

[16] *Chemie*, (Eds.: C. E. Mortimer, U. Muller), Georg Thieme Verlag, **2007**.

[17] K. Pfeifer, S. Arnold, J. Becherer, C. Das, J. Maibach, H. Ehrenberg, S. Dsoke, *ChemSusChem* **2019**, *12*, 3312–3319.

[18] J.-l. Ma, Y.-b. Yin, T. Liu, X.-b. Zhang, J.-m. Yan, Q. Jiang, *Advanced Functional Materials* **2018**, *28*, 1703931.

[19] B. Lee, E. Paek, D. Mitlin, S. W. Lee, *Chemical Reviews* **2019**, *119*, 5416–5460.

[20] L. Geng, D. Xue, J. Yao, Q. Dai, H. Sun, D. Zhu, Z. Rong, R. Fang, X. Zhang, Y. Su, J. Yan, S. J. Harris, S. Ichikawa, L. Zhang, Y. Tang, S. Zhang, J. Huang, *Energy & Environmental Science* **2023**, *16*, 2658–2668.

[21] T. Tsuda, C. L. Hussey, *The Electrochemical Society Interface* **2007**, *16*, 42–49.

[22] A. Ray, B. Saruhan, *Materials* **2021**, *14*, 2942.

[23] X. Wang, M. Salari, D.-e. Jiang, J. C. Varela, B. Anasori, D. J. Wesolowski, S. Dai, M. W. Grinstaff, Y. Gogotsi, *Nature Reviews Materials* **2020**, *5*, 787–808.

[24] D. R. MacFarlane, N. Tachikawa, M. Forsyth, J. M. Pringle, P. C. Howlett, G. D. Elliott, J. H. Davis, M. Watanabe, P. Simon, C. A. Angell, *Energy Environ. Sci.* **2014**, *7*, 232–250.

[25] A. Khan, C. A. Gunawan, C. Zhao, *ACS Sustainable Chemistry & Engineering* **2017**, *5*, 3698–3715.

[26] S. Shahzad, A. Shah, E. Kowsari, F. J. Iftikhar, A. Nawab, B. Piro, M. S. Akhter, U. A. Rana, Y. Zou, *Global Challenges* **2019**, *3*, 1800023.

[27] G. A. Giffin, *Journal of Materials Chemistry A* **2016**, *4*, 13378–13389.

[28] F. Wang, C.-y. Ge, D. Duan, H. Lin, L. Li, P. Naumov, H. Hu, *Small Structures* **2022**, *3*, 2200048.

[29] S. Bi, R. Wang, S. Liu, J. Yan, B. Mao, A. A. Kornyshev, G. Feng, *Nature Communications* **2018**, *9*, 5222.

[30] R. Wibowo, L. Aldous, E. I. Rogers, S. E. W. Jones, R. G. Compton, *The Journal of Physical Chemistry C* **2010**, *114*, 3618–3626.

[31] C. A. Berger, M. U. Ceblin, T. Jacob, *ChemElectroChem* **2017**, *4*, 261–265.

[32] L. H. S. Gasparotto, N. Borisenko, N. Bocchi, S. Z. E. Abedin, F. Endres, *Physical Chemistry Chemical Physics* **2009**, *11*, 11140–11145.

[33] J. A. Vega, J. Zhou, P. A. Kohl, *Journal of The Electrochemical Society* **2009**, *156*, A253.

[34] T. Carstens, A. Lahiri, N. Borisenko, F. Endres, *The Journal of Physical Chemistry C* **2016**, *120*, 14736–14741.

[35] H. Sakaebe, H. Matsumoto, *Electrochemistry Communications* **2003**, *5*, 594–598.

[36] K. Matsumoto, T. Hosokawa, T. Nohira, R. Hagiwara, A. Fukunaga, K. Numata, E. Itani, S. Sakai, K. Nitta, S. Inazawa, *Journal of Power Sources* **2014**, *265*, 36–39.

[37] S. Doblinger, T. J. Donati, D. S. Silvester, *The Journal of Physical Chemistry C* **2020**, *124*, 20309–20319.

[38] T. Pajkossy, C. Müller, T. Jacob, *Physical Chemistry Chemical Physics* **2018**, *20*, 21241–21250.

[39] S. Baldelli, *Accounts of Chemical Research* **2008**, *41*, 421–431.

[40] S. Zhou, K. S. Panse, M. H. Motevaselian, N. R. Aluru, Y. Zhang, *ACS Nano* **2020**, *14*, 17515–17523.

[41] N. Nishi, K. Minami, K. Motobayashi, M. Osawa, T. Sakka, *The Journal of Physical Chemistry C* **2017**, *121*, 1658–1666.

[42] J. Friedl, I. I. E. Markovits, M. Herpich, G. Feng, A. A. Kornyshev, U. Stimming, *ChemElectroChem* **2017**, *4*, 216–220.

[43] N. Borisenko, S. Z. E. Abedin, F. Endres, *ChemPhysChem* **2012**, *13*, 1736–1742.

[44] A. V. Rudnev, M. R. Ehrenburg, E. B. Molodkina, A. Abdelrahman, M. Arenz, P. Broekmann, T. Jacob, *ChemElectroChem* **2020**, *7*, 501–508.

[45] F. Endres, S. Z. E. Abedin, N. Borissenko, *Zeitschrift für Physikalische Chemie* **2006**, *220*, 1377–1394.

[46] K. R. Seddon, A. Stark, M.-J. Torres, *Pure and Applied Chemistry* **2000**, *72*, 2275–2287.

[47] S. Rivera-Rubero, S. Baldelli, *Journal of the American Chemical Society* **2004**, *126*, 11788–11789.

[48] J. E. S. J. Reid, A. J. Walker, S. Shimizu, *Physical Chemistry Chemical Physics* **2015**, *17*, 14710–14718.

[49] B. Dilasari, Y. Jung, K. Kwon, *Journal of Industrial and Engineering Chemistry* **2017**, *45*, 375–379.

[50] R. Hayes, S. Imberti, G. G. Warr, R. Atkin, *Angewandte Chemie International Edition* **2012**, *51*, 7468–7471.

[51] U. Schröder, J. D. Wadhawan, R. G. Compton, F. Marken, P. A. Z. Suarez, C. S. Consorti, R. F. de Souza, J. Dupont, *New Journal of Chemistry* **2000**, *24*, 1009–1015.

[52] X. Liu, X. Chen, Y. Xu, T. Chen, X. Zeng, *Sensors and Actuators B: Chemical* **2019**, *285*, 350–357.

[53] D. S. Silvester, R. G. Compton, *Zeitschrift für Physikalische Chemie* **2006**, *220*, 1247–1274.

[54] C. Villagrán, C. E. Banks, C. Hardacre, R. G. Compton, *Analytical Chemistry* **2004**, *76*, 1998–2003.

[55] N. Elgrishi, K. J. Rountree, B. D. McCarthy, E. S. Rountree, T. T. Eisenhart, J. L. Dempsey, *Journal of Chemical Education* **2018**, *95*, 197–206.

[56] L. A. Kibler, J. M. Hermann, F. M. Matzik, M. Wittmann, S. Fackler, T. Jacob in (Ed.: K. Wandelt), Elsevier, **2024**, pp. 426–449.

[57] J. Gong, C. B. Mullins, *Accounts of Chemical Research* **2009**, *42*, 1063–1073.

[58] D. M. Kolb, *Angewandte Chemie International Edition* **2001**, *40*, 1162–1181.

[59] M. A. Schneeweiss, D. Kolb, *Chemie in unserer Zeit* **2000**, *34*, 72–83.

[60] M.-K. Heubach, F. M. Schuett, J. Mayer, O. W. Elkhafif, A. K. Engstfeld, T. Jacob, **2024**, DOI 10.26434/CHEMRXIV-2024-05D56.

[61] R. Wen, B. Rahn, O. M. Magnussen, *Angewandte Chemie International Edition* **2015**, *54*, 6062–6066.

[62] R. Atkin, N. Borisenko, M. Drüschler, S. Z. E. Abedin, F. Endres, R. Hayes, B. Huber, B. Roling, *Physical Chemistry Chemical Physics* **2011**, *13*, 6849.

[63] W. Schmickler, E. Santos, *Interfacial Electrochemistry*, Springer Berlin Heidelberg, **2010**.

[64] P. T. Kissinger, W. R. Heineman, *Journal of Chemical Education* **1983**, *60*, 702.

[65] G. A. Mabbott, *Journal of Chemical Education* **1983**, *60*, 697.

[66] R. G. Compton, C. E. Banks, *Understanding Voltammetry*, World Scientific (Europe), **2018**.

[67] T. J. Davies, R. R. Moore, C. E. Banks, R. G. Compton, *Journal of Electroanalytical Chemistry* **2004**, *574*, 123–152.

[68] A. Hamelin, *Journal of Electroanalytical Chemistry* **1996**, *407*, 1–11.

[69] Y. Song, J. Tang, J. Hu, H. Yang, W. Gu, Y. Fu, X. Ji, *Electrochimica Acta* **2017**, *240*, 90–97.

[70] H. Feng, X. Xu, Y. Du, S. X. Dou, *Electrochemical Energy Reviews* **2021**, *4*, 249–268.

[71] Y. Liang, J. H. K. Pfisterer, D. McLaughlin, C. Csoklich, L. Seidl, A. S. Bandarenka, O. Schneider, *Small Methods* **2019**, *3*, 1800387.

[72] M. Giesen, *Progress in Surface Science* **2001**, *68*, 1–154.

[73] C. Rodenbücher, K. Wippermann, C. Korte, *Applied Sciences* **2019**, *9*, 2207.

[74] F. M. Schuett, M.-K. Heubach, J. Mayer, M. U. Ceblin, L. A. Kibler, T. Jacob, *Angewandte Chemie - International Edition* **2021**, *60*, 20461–20468.

[75] C. Müller, S. Vesztergom, T. Pajkossy, T. Jacob, *Journal of Electroanalytical Chemistry* **2015**, *737*, 218–225.

[76] C. Müller, K. Németh, S. Vesztergom, T. Pajkossy, T. Jacob, *Physical Chemistry Chemical Physics* **2016**, *18*, 916–925.

[77] A. Lewandowski, M. Biegun, M. Galinski, *Electrochimica Acta* **2012**, *63*, 204–208.

[78] I. Stepniak, *Journal of Power Sources* **2014**, *247*, 112–116.

[79] I. Stepniak, E. Andrzejewska, A. Dembna, M. Galinski, *Electrochimica Acta* **2014**, *121*, 27–33.

[80] A. Yongxin, C. Xinqun, Z. Pengjian, L. Lixia, Y. Geping, *Journal of Solid State Electrochemistry* **2012**, *16*, 383–389.

[81] O. W. A. M. Elkhafif, H. K. Hassan, M. Ceblin, A. Farkas, T. Jacob, *ChemSusChem* **2023**, e202300421.

[82] F. M. Schuett, D. Esau, K. L. Varvaris, S. Gelman, J. Björk, J. Rosen, G. Jerkiewicz, T. Jacob, *Angewandte Chemie International Edition* **2020**, *59*, 13246–13252.

[83] S. Cherevko, A. A. Topalov, A. R. Zeradjanin, I. Katsounaros, K. J. J. Mayrhofer, *RSC Advances* **2013**, *3*, 16516.

[84] G. A. Somorjai, *Chemistry in Two Dimensions: Surfaces*, Cornell University Press, **1981**.

[85] G. A. Somorjai, *Introduction to Surface Chemistry and Catalysis*, Wiley-Interscience, **1994**.

[86] V. Repain, J. Berroir, S. Rousset, J. Lecoeur, *Applied Surface Science* **2000**, *162-163*, 30–36.

[87] V. Repain, J. M. Berroir, S. Rousset, J. Lecoeur, *Europhysics Letters (EPL)* **1999**, *47*, 435–441.

[88] D. Kolb, *Progress in Surface Science* **1996**, *51*, 109–173.

[89] A. S. Dakkouri, M. Dietterle, D. M. Kolb in (Ed.: R. Helbig), Springer Berlin Heidelberg, **1997**, pp. 151–173.

[90] J. V. Barth, H. Brune, G. Ertl, R. J. Behm, *Physical Review B* **1990**, *42*, 9307–9318.

[91] A. W. Stephenson, C. J. Baddeley, M. S. Tikhov, R. M. Lambert, *Surface Science* **1998**, *398*, 172–183.

[92] S. Narasimhan, D. Vanderbilt, *Physical Review Letters* **1992**, *69*, 1564–1567.

[93] L. A. Kibler, J. M. Hermann, A. Abdelrahman, A. A. El-Aziz, T. Jacob, *Current Opinion in Electrochemistry* **2018**, *9*, 265–270.

[94] Z. Tan, Y. Peng, J. Liu, Y. Yang, Z. Zhang, Z. Chen, B. Mao, J. Yan, *ChemElectroChem* **2020**, *7*, 4601–4605.

[95] R. Hayes, G. G. Warr, R. Atkin, *Chemical Reviews* **2015**, *115*, 6357–6426.

[96] M. Freemantle, T. Welton, R. D. Rogers, *An Introduction to Ionic Liquids*, The Royal Society of Chemistry, **2009**.

[97] S. K. Singh, A. W. Savoy, *Journal of Molecular Liquids* **2020**, *297*, 112038.

[98] L. E. Barrosse-Antle, A. M. Bond, R. G. Compton, A. M. O'Mahony, E. I. Rogers, D. S. Silvester, *Chemistry – An Asian Journal* **2010**, *5*, 202–230.

[99] G. A. O. Tiago, I. A. S. Matias, A. P. C. Ribeiro, L. M. D. R. S. Martins, *Molecules* **2020**, *25*, 5812.

[100] L. Cammarata, S. G. Kazarian, P. A. Salter, T. Welton, *Physical Chemistry Chemical Physics* **2001**, *3*, 5192–5200.

[101] L. L. Lazarus, C. T. Riche, B. C. Marin, M. Gupta, N. Malmstadt, R. L. Brutchey, *ACS Applied Materials & Interfaces* **2012**, *4*, 3077–3083.

[102] N. Sieffert, G. Wipff, *The Journal of Physical Chemistry B* **2006**, *110*, 13076–13085.

[103] J. G. Huddleston, A. E. Visser, W. M. Reichert, H. D. Willauer, G. A. Broker, R. D. Rogers, *Green Chemistry* **2001**, *3*, 156–164.

[104] E. L. Smith, A. P. Abbott, K. S. Ryder, *Chemical Reviews* **2014**, *114*, 11060–11082.

[105] T. Geng, S. J. Zeller, L. A. Kibler, M. U. Ceblin, T. Jacob, *ChemElectroChem* **2022**, *9*, e202101283.

[106] D. M. Correia, L. C. Fernandes, M. M. Fernandes, B. Hermenegildo, R. M. Meira, C. Ribeiro, S. Ribeiro, J. Reguera, S. Lanceros-Méndez, *Nanomaterials* **2021**, *11*, 2401.

[107] N. V. Veríssimo, F. A. Vicente, R. C. de Oliveira, B. Likozar, R. P. de Souza Oliveira, J. F. B. Pereira, *Biotechnology Advances* **2022**, *61*, 108055.

[108] F. M. Maia, O. Rodríguez, E. A. Macedo, *Industrial & Engineering Chemistry Research* **2012**, *51*, 8061–8068.

[109] R. Atkin, S. Z. E. Abedin, R. Hayes, L. H. S. Gasparotto, N. Borisenko, F. Endres, *The Journal of Physical Chemistry C* **2009**, *113*, 13266–13272.

[110] R. Atkin, N. Borisenko, M. Drüschler, F. Endres, R. Hayes, B. Huber, B. Roling, *Journal of Molecular Liquids* **2014**, *192*, 44–54.

[111] N. Borisenko, S. Z. E. Abedin, F. Endres, *The Journal of Physical Chemistry B* **2006**, *110*, 6250–6256.

[112] M. C. Kroon, W. Buijs, C. J. Peters, G.-J. Witkamp, *Green Chem.* **2006**, *8*, 241–245.

[113] S. Doblinger, J. Lee, D. S. Silvester, *The Journal of Physical Chemistry C* **2019**, *123*, 10727–10737.

[114] F. D. Giorgio, F. Soavi, M. Mastragostino, *Electrochemistry Communications* **2011**, *13*, 1090–1093.

[115] A. M. O'Mahony, D. S. Silvester, L. Aldous, C. Hardacre, R. G. Compton, *Journal of Chemical & Engineering Data* **2008**, *53*, 2884–2891.

[116] S. Randström, G. Appetecchi, C. Lagergren, A. Moreno, S. Passerini, *Electrochimica Acta* **2007**, *53*, 1837–1842.

[117] S. Randström, M. Montanino, G. B. Appetecchi, C. Lagergren, A. Moreno, S. Passerini, *Electrochimica Acta* **2008**, *53*, 6397–6401.

[118] M. Z. Bazant, B. D. Storey, A. A. Kornyshev, *Physical Review Letters* **2011**, *106*, 046102.

[119] A. Forse, **2015**, DOI 10.17863/CAM.26359.

[120] M. Belotti, X. Lyu, L. Xu, P. Halat, N. Darwish, D. S. Silvester, C. Goh, E. I. Izgorodina, M. L. Coote, S. Ciampi, *Journal of the American Chemical Society* **2021**, *143*, 17431–17440.

[121] S. Begić, F. Chen, E. Jónsson, M. Forsyth, *Physical Review Materials* **2019**, *3*, 095801.

[122] G. R. Elliott, K. P. Gregory, H. Robertson, V. S. Craig, G. B. Webber, E. J. Wanless, A. J. Page, *Chemical Physics Letters* **2024**, *843*, 141190.

[123] Z. A. Goodwin, G. Feng, A. A. Kornyshev, *Electrochimica Acta* **2017**, *225*, 190–197.

[124] M. A. Gebbie, A. M. Smith, H. A. Dobbs, A. A. Lee, G. G. Warr, X. Banquy, M. Valtiner, M. W. Rutland, J. N. Israelachvili, S. Perkin, R. Atkin, *Chemical Communications* **2017**, *53*, 1214–1224.

[125] T. J. Hersbach, M. T. Koper, *Current Opinion in Electrochemistry* **2021**, *26*, 100653.

[126] M. M. Elnagar, T. Jacob, L. A. Kibler, *Electrochemical Science Advances* **2022**, *2*, e2100175.

[127] A. I. Yanson, P. Rodriguez, N. Garcia-Araez, R. V. Mom, F. D. Tichelaar, M. T. M. Koper, *Angewandte Chemie International Edition* **2011**, *50*, 6346–6350.

[128] T. J. P. Hersbach, I. T. McCrum, D. Anastasiadou, R. Wever, F. Calle-Vallejo, M. T. M. Koper, *ACS Applied Materials & Interfaces* **2018**, *10*, 39363–39379.

[129] M. M. Elnagar, J. M. Hermann, T. Jacob, L. A. Kibler, *Electrochimica Acta* **2021**, *372*, 137867.

[130] M. M. Elnagar, J. M. Hermann, T. Jacob, L. A. Kibler, *Current Opinion in Electrochemistry* **2021**, *27*, 100696.

[131] F. Lu, X. Ji, Y. Yang, W. Deng, C. E. Banks, *RSC Advances* **2013**, *3*, 18791.

[132] Z. Liu, O. Höfft, A. S. Gödde, F. Endres, *The Journal of Physical Chemistry C* **2021**, *125*, 26793–26800.

[133] J. Medina-Ramos, W. Zhang, K. Yoon, P. Bai, A. Chemburkar, W. Tang, A. Atifi, S. S. Lee, T. T. Fister, B. J. Ingram, J. Rosenthal, M. Neurock, A. C. T. van Duin, P. Fenter, *Chemistry of Materials* **2018**, *30*, 2362–2373.

[134] M. Paunovic, M. Schlesinger, *Fundamentals of electrochemical deposition*, john wiley & sons, **2006**.

[135] D. Monti, E. Jónsson, M. R. Palacín, P. Johansson, *Journal of Power Sources* **2014**, *245*, 630–636.

[136] E. Budevski, G. Staikov, W. J. Lorenz, *Electrochemical Phase Formation and Growth*, Wiley, **1996**.

[137] S. Frittmann, R. Schuster, *The Journal of Physical Chemistry C* **2016**, *120*, 21522–21535.

[138] M. Hölzle, V. Zwing, D. Kolb, *Electrochimica Acta* **1995**, *40*, 1237–1247.

[139] V. Rooryck, F. Reniers, C. Buess-Herman, G. Attard, X. Yang, *Journal of Electroanalytical Chemistry* **2000**, *482*, 93–101.

[140] A. D. Pelton, *Bulletin of Alloy Phase Diagrams* **1986**, *7*, 136–139.

[141] A. D. Pelton, *Bulletin of Alloy Phase Diagrams* **1986**, *7*, 228–231.

[142] F. A. Möller, O. M. Magnussen, R. J. Behm, *Physical Review Letters* **1996**, *77*, 5249–5252.

[143] M. Kleinert, H. F. Waibel, G. E. Engelmann, H. Martin, D. M. Kolb, *Electrochimica Acta* **2001**, *46*, 3129–3136.

[144] C. S. Casari, S. Foglio, F. Siviero, A. L. Bassi, M. Passoni, C. E. Bottani, *Physical Review B* **2009**, *79*, 195402.

[145] D. D. Chambliss, R. J. Wilson, S. Chiang, *Physical Review Letters* **1991**, *66*, 1721–1724.

[146] J. A. Meyer, I. D. Baikie, E. Kopatzki, R. J. Behm, *Surface Science* **1996**, *365*, 647–651.

[147] I. Chado, S. Padovani, F. Scheurer, J. P. Bucher, *Applied Surface Science* **2000**, *164*, 42–47.

[148] T. H. Gentner, F. Scheurer, T. Detzel, J. P. Bucher, *Thin Solid Films* **1996**, *275*, 58–60.

[149] S. Padovani, F. Scheurer, J. P. Bucher, *Europhysics Letters (EPL)* **1999**, *45*, 327–333.

[150] K. Schouteden, E. Lijnen, E. Janssens, A. Ceulemans, L. F. Chibotaru, P. Lievens, C. V. Haesendonck, *New Journal of Physics* **2008**, *10*, 043016.

[151] H. Takeshita, Y. Suzuki, H. Akinaga, W. Mizutani, K. Ando, T. Katayama, A. Itoh, K. Tanaka, *Journal of Magnetism and Magnetic Materials* **1997**, *169*, 38–41.

[152] B. Voigtländer, G. Meyer, N. M. Amer, *Physical Review B* **1991**, *44*, 10354–10357.

[153] E. I. Altman, R. J. Colton, *Surface Science* **1994**, *304*, L400–L406.

[154] M. M. Biener, J. Biener, R. Schalek, C. M. Friend, *Surface Science* **2005**, *594*, 221–230.

[155] S. Helveg, J. V. Lauritsen, E. Lægsgaard, I. Stensgaard, J. K. Nørskov, B. S. Clausen, H. Topsøe, F. Besenbacher, *Physical Review Letters* **2000**, *84*, 951–954.

[156] M. M. Dovek, C. A. Lang, J. Nogami, C. F. Quate, *Physical Review B* **1989**, *40*, 11973–11975.

[157] B. Fischer, H. Brune, J. V. Barth, A. Fricke, K. Kern, *Physical Review Letters* **1999**, *82*, 1732–1735.

[158] B. Fischer, J. Barth, A. Fricke, L. Nedelmann, K. Kern, *Surface Science* **1997**, *389*, 366–374.

[159] J. V. Barth, H. Brune, R. Schuster, G. Ertl, R. J. Behm, *Surface Science* **1993**, *292*, L769–L774.

[160] J. Barth, R. Behm, G. Ertl, *Surface Science* **1995**, *341*, 62–91.

[161] L. Cagnon, A. Gundel, T. Devolder, A. Morrone, C. Chappert, J. E. Schmidt, P. Allongue, *Applied Surface Science* **2000**, *164*, 22–28.

[162] S. E. Abedin, F. Endres, *Electrodeposition from Ionic Liquids*, (Eds.: F. Endres, A. Abbott, D. MacFarlane), Wiley, **2017**.

[163] Y. He, Y. Cui, W. Shang, Z. Zhao, P. Tan, *Chemical Engineering Journal* **2022**, *438*, 135541.

[164] J. Wang, *Analytical Electrochemistry*, 3rd ed., John Wiley & Sons, Inc., **2006**.

[165] G. Wedler, H.-J. Freund, *Lehrbuch der Physikalischen Chemie*, 6th ed., Wiley-VCH Verlag & Co. KGaA, **2015**.

[166] G. Binnig, H. Rohrer, C. Gerber, E. Weibel, *Physical Review Letters* **1982**, *49*, 57–61.

[167] P. K. Hansma, J. Tersoff, *Journal of Applied Physics* **1987**, *61*, R1–R24.

[168] E. Meyer, H. J. Hug, R. Bennewitz, *Scanning Probe Microscopy*, Springer Berlin Heidelberg, **2004**.

[169] D. M. Kolb, F. C. Simeone in (Eds.: M. Bowker, P. R. Davies), Wiley, **2009**, pp. 119–146.

[170] A. Abdelrahman, J. M. Hermann, T. Jacob, L. A. Kibler, *ChemPhysChem* **2019**, *20*, 2989–2996.

[171] M. A. Schneeweiss, D. M. Kolb, *Solid State Ionics* **1997**, *94*, 171–179.

[172] C. Stumm, S. Grau, F. D. Speck, F. Hilpert, V. Briega-Martos, K. Mayrhofer, S. Cherevko, O. Brummel, J. Libuda, *The Journal of Physical Chemistry C* **2021**, *125*, 22698–22704.

[173] C. M. Vitus, A. J. Davenport, *Journal of The Electrochemical Society* **1994**, *141*, 1291–1298.

[174] P. Eaton, P. West, *Atomic Force Microscopy*, Oxford University Press, **2010**.

[175] I. T. Lucas, E. Pollak, R. Kostecki, *Electrochemistry Communications* **2009**, *11*, 2157–2160.

[176] H. Zhang, D. Wang, C. Shen, *Applied Surface Science* **2020**, *507*, 145059.

[177] M. Steinhauer, M. Stich, M. Kurniawan, B.-K. Seidlhofer, M. Trapp, A. Bund, N. Wagner, K. A. Friedrich, *ACS Applied Materials & Interfaces* **2017**, *9*, 35794–35801.

[178] V. Weinstein, M. Slutzky, A. Arenshtam, E. Ben-Jacob, *Review of Scientific Instruments* **1995**, *66*, 3075–3076.

[179] B. Voigtländer, *Scanning Probe Microscopy*, Springer Berlin Heidelberg, **2015**.

[180] U. D. Schwarz, H. Haefke, P. Reimann, H.-J. Güntherodt, *Journal of Microscopy* **1994**, *173*, 183–197.

[181] J. P. Pelz, R. H. Koch, *Physical Review B* **1990**, *41*, 1212–1215.

[182] S.-W. Hla, K.-F. Braun, V. Iancu, A. Deshpande, *Nano Letters* **2004**, *4*, 1997–2001.

[183] S.-W. Hla, *Journal of Vacuum Science & Technology B: Microelectronics and Nanometer Structures Processing Measurement and Phenomena* **2005**, *23*, 1351–1360.

[184] M. Gnahm, D. M. Kolb, *Journal of Electroanalytical Chemistry* **2011**, *651*, 250–252.

[185] L. Mayrand-Provencher, D. Rochefort, *Electrochimica Acta* **2009**, *54*, 7422–7428.

[186] D. Aurbach, H. Gottlieb, *Electrochimica Acta* **1989**, *34*, 141–156.

[187] H.-W. Cheng, J.-N. Dienemann, P. Stock, C. Merola, Y.-J. Chen, M. Valtiner, *Scientific Reports* **2016**, *6*, 30058.

[188] G. Feng, X. Jiang, R. Qiao, A. A. Kornyshev, *ACS Nano* **2014**, *8*, 11685–11694.

[189] M. Moreno, F. Castiglione, A. Mele, C. Pasqui, G. Raos, *The Journal of Physical Chemistry B* **2008**, *112*, 7826–7836.

[190] L. Aldous, D. S. Silvester, C. Villagrán, W. R. Pitner, R. G. Compton, M. C. Lagunas, C. Hardacre, *New J. Chem.* **2006**, *30*, 1576–1583.

[191] M. Gnahm, T. Pajkossy, D. Kolb, *Electrochimica Acta* **2010**, *55*, 6212–6217.

[192] K. Motobayashi, K. Minami, N. Nishi, T. Sakka, M. Osawa, *The Journal of Physical Chemistry Letters* **2013**, *4*, 3110–3114.

[193] A. Stark, P. Behrend, O. Braun, A. Müller, J. Ranke, B. Ondruschka, B. Jastorff, *Green Chemistry* **2008**, *10*, 1152–1161.

[194] T. Pajkossy, D. M. Kolb, *Electrochemistry Communications* **2011**, *13*, 284–286.

[195] D. W. Breck, *Journal of Chemical Education* **1964**, *41*, 678.

[196] X. Hu, C. Chen, S. Tang, W. Wang, J. Yan, B. Mao, *Science Bulletin* **2015**, *60*, 877–883.

[197] F. M. Schuett, S. J. Zeller, M. J. Eckl, F. M. Matzik, M.-K. Heubach, T. Geng, J. M. Hermann, M. Uhl, L. A. Kibler, A. K. Engstfeld, T. Jacob, *Angewandte Chemie International Edition* **2021**, *60*, 22783–22790.

[198] C. Scordilis-Kelley, J. Fuller, R. T. Carlin, J. S. Wilkes, *Journal of The Electrochemical Society* **1992**, *139*, 694–699.

[199] C. Scordilis-Kelley, R. T. Carlin, *Journal of The Electrochemical Society* **1993**, *140*, 1606–1611.

[200] M. Forsyth, G. Girard, A. Basile, M. Hilder, D. MacFarlane, F. Chen, P. Howlett, *Electrochimica Acta* **2016**, *220*, 609–617.

[201] A. Abbott, L. Aldous, N. Borisenko, S. Coles, O. Fontaine, J. Daniel, G. Garcia, R. Gardas, O. Hammond, L. J. Hardwick, P.-H. Haumesser, F. Hausen, C. Horwood, J. Jacquemin, R. Jones, J. ´. Onsson, A. Lahiri, D. Macfarlane, G. Marlair, B. May, H. Medhi, V. H. Paschoal, J. E. S. J. Reid, T. Schoetz, K. Tamura, M. L. Thomas, S. Tiwari, B. Uralcan, A. V. D. Bruinhorst, M. Watanabe, J. Wishart, A. P. Abbott, G. Frisch, S. J. Gurman, A. R. Hillman, J. Hartley, F. Holyoak, K. S. Ryder, *Chem. Commun* **2011**, *47*, 20.

[202] M.-K. Heubach, J. Bansmann, A. K. Engstfeld, T. Jacob, **2024**, DOI 10 . 26434 / CHEMRXIV-2024-ZKKNM.

[203] F. Buchner, K. Forster-Tonigold, M. Bozorgchenani, A. Gross, R. J. Behm, *Journal of Physical Chemistry Letters* **2016**, *7*, 226–233.

[204] B. K. Sweeny, D. G. Peters, *Electrochemistry Communications* **2001**, *3*, 712–715.

[205] M.-K. Heubach, F. M. Schuett, L. A. Kibler, A. Abdelrahman, T. Jacob, *ChemElectroChem* **2022**, *9*, e202200722.

[206] S. Ntais, A. Moschovi, F. Paloukis, S. Neophytides, V. Burganos, V. Dracopoulos, V. Nikolakis, *Journal of Power Sources* **2011**, *196*, 2202–2210.

[207] E. E. Switzer, R. Zeller, Q. Chen, K. Sieradzki, D. A. Buttry, C. Friesen, *Journal of Physical Chemistry C* **2013**, *117*, 8683–8690.

[208] Y. Katayama, H. Onodera, M. Yamagata, T. Miura, *Journal of The Electrochemical Society* **2004**, *151*, A59.

[209] X.-Z. Yuan, V. Alzate, Z. Xie, D. G. Ivey, W. Qu, *Journal of The Electrochemical Society* **2014**, *161*, A451–A457.

[210] L. Aldous, D. S. Silvester, W. R. Pitner, R. G. Compton, M. C. Lagunas, C. Hardacre, *Journal of Physical Chemistry C* **2007**, *111*, 8496–8503.

[211] R.-S. Kühnel, D. Reber, A. Remhof, R. Figi, D. Bleiner, C. Battaglia, *Chemical Communications* **2016**, *52*, 10435–10438.

[212] M. Hayyan, F. S. Mjalli, M. A. Hashim, I. M. AlNashef, T. X. Mei, *Journal of Industrial and Engineering Chemistry* **2013**, *19*, 106–112.

[213] J. Zhang, A. M. Bond, *The Analyst* **2005**, *130*, 1132.

[214] U. Zhumaev, A. V. Rudnev, J.-F. Li, A. Kuzume, T.-H. Vu, T. Wandlowski, *Electrochimica Acta* **2013**, *112*, 853–863.

[215] J. K. Nørskov, T. Bligaard, A. Logadottir, J. R. Kitchin, J. G. Chen, S. Pandelov, U. Stimming, *Journal of The Electrochemical Society* **2005**, *152*, J23.

[216] J. M. Hermann, A. Abdelrahman, T. Jacob, L. A. Kibler, *Electrochimica Acta* **2020**, *347*, 136287.

[217] E. Torres, G. A. DiLabio, *The Journal of Physical Chemistry C* **2014**, *118*, 15624–15629.

[218] C. Vaz-Domínguez, M. Escudero-Escribano, A. Cuesta, F. Prieto-Dapena, C. Cerrillos, M. Rueda, *Electrochemistry Communications* **2013**, *35*, 61–64.

[219] R. W. Haid, R. M. Kluge, Y. Liang, A. S. Bandarenka, *Small Methods* **2021**, *5*, 2000710.

[220] R. M. Kluge, R. W. Haid, I. E. L. Stephens, F. Calle-Vallejo, A. S. Bandarenka, *Physical Chemistry Chemical Physics* **2021**, *23*, 10051–10058.

[221] *Nano Energy* **2018**, *48*, 101–106.

[222] S. Tang, Y.-Y. Y. Zhang, X.-G. G. Zhang, J.-T. T. Li, X.-Y. Y. Wang, J.-W. W. Yan, D.-Y. Y. Wu, M.-S. S. Zheng, Q.-F. F. Dong, B.-W. W. Mao, *Advanced Materials* **2019**, *31*, 1807495.

[223] J. C. Slater, *The Journal of Chemical Physics* **1964**, *41*, 3199–3204.

[224] P. Bach, M. Stratmann, I. Valencia-Jaime, A. Romero, F. Renner, *Electrochimica Acta* **2015**, *164*, 81–89.

[225] P. Bach, I. Valencia-Jaime, U. Rütt, O. Gutowski, A. H. Romero, F. U. Renner, *Chemistry of Materials* **2016**, *28*, 2941–2948.

[226] H. Gerischer, D. Kolb, M. Przasnyski, *Surface Science* **1974**, *43*, 662–666.

[227] S. Chen, F. Sanz, D. Ogletree, V. Hallmark, T. Devine, M. Salmeron, *Surface Science* **1993**, *292*, 289–297.

[228] M. del Barrio, S. García, D. Salinas, *Electrochemistry Communications* **2004**, *6*, 762–766.

[229] J. Erlebacher, K. Sieradzki, *Scripta Materialia* **2003**, *49*, 991–996.

[230] R. A. Huggins, *Journal of Power Sources* **1999**, *81-82*, 13–19.

[231] S. Iwamura, H. Nishihara, Y. Ono, H. Morito, H. Yamane, H. Nara, T. Osaka, T. Kyotani, *Scientific Reports* **2015**, *5*, 8085.

List of Figures

2.1 fcc unit cell and its (111) plane. 6
2.2 Possible surface defects on the Au(111) plane. 7
2.3 The reconstructed Au(111) surface. 8
2.4 Structural formula of [MPPip][TFSI]. 10
2.5 IL-electrolde interface models. 10
2.6 Schematic metal electrodepostion. 13
2.7 Recording a cyclic voltammogram. 15
2.8 Scheme of the tunnelling effect. 16
2.9 Schematic image of the *in situ* STM set-up. 17
2.10 Imaging with assymmetric tips. 18
2.11 Typical artefacts during *in situ* STM measurements. 19

3.1 CVs for Au(111) in [BMPyr][TFSI] as reported in literature. 23

4.1 Electrochemical cells. 31
4.2 STM tip preparation. 33
4.3 STM setup. 34

5.1 CVs for Au(111) in the five different batches of the IL [MPPip][TFSI]. 40
5.2 XP spectra of the five different batches of the IL [MPPip][TFSI]. 41
5.3 CVs for Au(111) in [MPPip][TFSI] with different lower potential limits I · 42
5.4 CVs for Au(111) in [MPPip][TFSI] with different lower potential limits II. 44
5.5 Effect of different drying procedures of the CVs for Au(111) in [MPPip][TFSI]. . . 47
5.6 CVs with a LPL of –2.0 V for the IL with and without molecular sieve. 48
5.7 Influence of the molecular sieve on the CVs for batches of behaviour II. 49
5.8 XP spectra showing the influence of the molecular sieve. 51
5.9 Water influence of the CVs for Au(111) in [MPPip][TFSI]. 52
5.10 Time effect after water addition to [MPPip][TFSI]. 53
5.11 CVs for Au(111) in [MPPip][TFSI] after H[TFSI] addition. 55

6.1 Linear potential sweeps for Au(111) in [MPPip][TFSI]. 58

6.2 *In situ* STM images of the cathodic and anodic corrosion of Au(111) in [MPPip][TFSI]. 59
6.3 *In situ* STM images of the initial stages of the cathodic corrosion of Au(111) in [MPPip][TFSI] with 20 ppm H_2O. 60
6.4 *In situ* STM image of the ongoing cathodic corrosion of Au(111) in [MPPip][TFSI] with 20 ppm H_2O with the corresponding height profile. 61
6.5 *In situ* STM images of the initial stages of the cathodic corrosion of Au(111) in [MPPip][TFSI] with 100 ppm H_2O. 63
6.6 *In situ* STM image of the ongoing cathodic corrosion of Au(111) in [MPPip][TFSI] with 100 ppm H_2O with the corresponding height profile. 64
6.7 *In situ* STM images of the initial stages of the cathodic corrosion of Au(111) in [MPPip][TFSI] with 200 ppm H_2O. 65
6.8 Comparison of the pit fromation at different H_2O contents. 67
6.9 Scheme of the cathodic corrosion in ILs. 70
6.10 *In situ* STM images of the lifting of the reconstruction of Au(111) in [MPPip][TFSI]. 71
6.11 *In situ* STM images of surface restructuring of Au(111) in [MPPip][TFSI] with 100 ppm H_2O during the ORR I. 73
6.12 *In situ* STM images of surface restructuring of Au(111) in [MPPip][TFSI] with 100 ppm H_2O during the ORR II. 74
6.13 *In situ* STM images of surface restructuring of Au(111) in [MPPip][TFSI] with 100 ppm H_2O during the ORR III. 75
6.14 Step heights of all images of the measurement of Figures 6.5, 6.6, 6.11,6.12, and 6.13. 76
6.15 Potentials of surface restructuring processes of Au(111) in [MPPip][TFSI]. . . . 78

7.1 CVs for Au(111) recorded in a 200 mM solution of Na[TFSI] in the IL [MPPip][TFSI]. 80
7.2 *In situ* STM images of the initial stages of the Na deposition. 83
7.3 *In situ* STM images of the Na UPD I. 86
7.4 *In situ* STM images of the Na UPD II. 87
7.5 *In situ* STM images of the Na UPD III. 89
7.6 *In situ* STM images of the surface structures during Na UPD. 90
7.7 CVs for Na bulk deposition on Au(111). 92
7.8 CV for alloy formation of polycrystalline Au with Na in an organic electrolyte. . . 94
7.9 CVs for Au(111) in 10 mM Li[TFSI] in [MPPip][TFSI]. 95
7.10 CVs for Au(111) in 10 mM, respectively 200 mM Li[TFSI] in [MPPip][TFSI]. . . . 98

7.11 *In situ* STM images of the Li UPD on Au(111) at 1.45 V. 99
7.12 *In situ* STM images of the Li UPD on Au(111) at 1.25 V. 100
7.13 *In situ* STM images of the Li UPD on Au(111) at 0.75 V and following dissolution. 101

8.1 Overview on the potentials of Na and Li UPD on Au(111) and the surface restructuring processes of Au(111) in [MPPip][TFSI]. 105

List of Tables

4.1 Tip etching. . . . 33
4.2 Au(111) crystal. . . . 35
4.3 Batches of the IL [MPPip][TFSI]. . . . 36
4.4 Additives for the IL-based electrolytes. . . . 36
4.5 Gases. . . . 36
4.6 Metal wires and sheets. . . . 37
4.7 Other chemicals. . . . 37

7.1 Peak potentials for the Na deposition and dissolution. . . . 81
7.2 Islands coverage, number and average size for the Na UPD. . . . 87
7.3 Comparison of the Potentials for Na and Li Deposition. . . . 97

A.1 Overview on all batches and preparations. . . . 108
A.2 Overview on all batches and preparations (continued). . . . 109
A.3 Parameters of the STM images 1. . . . 110
A.4 Parameters of the STM images 2. . . . 111
A.5 Step heights in Figures 6.5, 6.6, 6.11,6.12, and 6.13. . . . 112

Curriculum Vitae

This section has been removed due to data protection.

Declaration

Hereby, I declare that I wrote the thesis independently and used no other aids than those cited. In each individual case, I have clearly identified the sources of the passages that are taken word for word or paraphrased from other works.

Ulm, date .....

Maren-Kathrin Heubach

Danksagung

Dieser Abschnitt wurde aufgrund von Datenschutz entfernt.